Stellingen

behorende bij het proefschrift

Multimode interference couplers design and applications

van

Lucas Beda Soldano

Delft, 14 oktober 1994

-I-

The term Multimode Interference (MMI) reflects more the chosen model than the operating principle of the devices treated in this thesis.

-II-

MMI couplers based on paired interference are actually longer, and therefore less tolerant, than those based on general interference. They can nonetheless provide lower losses than those based on general interference, when implemented in weakly guiding structures. (This thesis, chapter 2).

-III-

Field plots obtained by Beam Propagation Methods (BPMs) give little information over the way an optical device works, yet they are pretty convincing, which happens to be more important than comprehension when it comes to communicate scientific work.

-IV-

Due to its long time between submission and publication of a paper, the *Journal of Lightwave Technology* provides quite vivid and accurate historical overviews in the field of optical communication research.

-V-

Virtual Reality is a very powerful concept which enables people to roughly visualize how distorted this universe can be in some engineers' minds.

-VI-

The distinction between "political" refugees and "economic" refugees is made in order to a) appease some consciences by assisting ones, and b) keep the expenses low (and the status quo unchanged) by turning down the others.

-VII-

The two-year "certified designer" course (TWAIO) simply completes the necessary training (which is not provided by the four-year graduate curriculum) of a full-fledged engineer, and is therefore not recognized abroad as a post-graduate course.

-VIII-

The most remarkable discoveries of particle physics in the last half century are parity nonconservation and the breakdown of time-reversal symmetry. In other words, our scientists have managed to learn that right can be distinguished from left and that time future is different from time past.

-IX-

Max Havelaar, the powerful indictment of Dutch colonialism written by Eduard Douwes Dekker under the pseudonym Multatuli during 1859, was more effective in driving a nail into the coffin of the thirty-year old Culture System (the so-called Kultuurstelsel) than in achieving official rehabilitation to its author.

-X-

"Sollicitatieplichtig" is a eufemism used by the Dutch Ministry of Internal Affairs to denote "aanvaardingsplichtig". This fact can have negative financial consequences to those job-seekers who are candid enough to ask for advice to the Ministry.

-XI-

The very low number of female students at the Delft University of Technology has a profoundly disquieting effect on the local male students, and inclines visitors to doubt about sexual equality in the Netherlands.

-XII

The tendency of Dutch translations towards the use of *specification* and *explanation* —in contrast to the globally more prevalent tendency towards *generalization*— hinders the readers from savouring the most characteristic literary elements of contemporary Spanish and Spanish-American fictional prose.

Multimode Interference Couplers

Design and Applications

The picture on the cover shows the field evolution in a 1×2 multimode power splitter, calculated with the Beam Propagation Method. *See also* Section 3.5.

Multimode Interference Couplers

Design and Applications

PROEFSCHRIFT

ter verkrijging van de graad van doctor
aan de Technische Universiteit Delft,
op gezag van de Rector Magnificus Prof. ir. K.F. Wakker,
in het openbaar te verdedigen ten overstaan van een commissie,
door het College van Dekanen aangewezen,
op vrijdag 14 oktober 1994 te 16:00 uur
door

Lucas Beda SOLDANO

Electronics Engineer,
Universidad de Buenos Aires,
geboren te Buenos Aires,
Argentina

Dit proefschrift is goedgekeurd door de promotor:
Prof. dr. B.H. Verbeek

Toegevoegd promotor:
Dr. ir. M.K. Smit

This work was supported by the Technical Sciences Foundation (STW) within the programme of the Dutch Foundation for Fundamental Research on Matter (FOM).

Published and distributed by:
Delft University Press
Stevinweg 1
2628 CN Delft
The Netherlands
Telephone +31-15-783254
Fax +31-15-781661

CIP-DATA KONINKLIJKE BIBLIOTHEEK, DEN HAAG

Soldano, Lucas Beda

Multimode interference couplers : design and applications / Lucas Beda Soldano. -
Delft : Delft University Press. - Ill.
Ph.D. Thesis Delft University of Technology. - With ref. - With summary in Dutch.
ISBN 90-407-1044-9
NUGI 841
Keywords: Integrated optics / optoelectronics.

Printed in The Netherlands

a mis viejos

Summary

This thesis describes integrated optical devices based on multimode interference (MMI), their analysis, fabrication, measurements, and a few applications.

The operation of MMI devices is based on the principle of self-imaging, by which single or multiple replicas of an input field are produced at regular intervals along the propagation direction of a multimode waveguide. The self-imaging principle was studied by means of a guided-mode propagation analysis. Different interference mechanisms were found according to the modal excitation, which give rise to a wide range of N×N and N×M optical couplers. A simple expression was derived, which allows the calculation of the imaging resolution of a multimode waveguide in terms of its lateral numerical aperture. Tolerances to fabrication and operation parameters were calculated. The multimode section width was predicted to be the most critical parameter to control during the fabrication process.

A number of 3-dB and cross couplers have been designed, fabricated, and tested for operation at 1.55-μm wavelength window. Excess losses below 0.5 dB, crosstalk figures of -18 dB, and balancing within 0.2 dB have been measured in silica-based and in InP-based couplers. An experimental assessment of fabrication and operation tolerances was carried out for InGaAsP/InP 3-dB couplers. It was found that, in order to ensure a loss penalty below 1.0 dB and an imbalance below 0.2 dB, the multimode section width has to be within ± 0.25 μm of its design value. With the same limiting conditions, 1-dB optical bandwidths as large as 100 nm were measured. By optimizing the design for one polarization, loss penalty due to polarization changes were predicted and measured to be around 0.3 dB. Polarization-independent operation is possible by designing at half-way in between the different polarization optima, thus sharing (half) the penalty.

A very short ($\sim$25 μm for silica-based and $\sim$60 μm for InP-based waveguides) 1×2 power splitter/combiner was fabricated. Average excess losses of 1.0 dB, together with imbalances as low as 0.1 dB in were measured in 30-40% of all devices.

An all-passive 4×4 phase diversity network was demonstrated which comprises four MMI 3-dB couplers, a phase shifter and routing waveguide structures. A best performance of $\sim$3 dB excess-loss, with imbalances within 0.5 dB and phase deviations of 5°/12°/12°/9° was obtained.

Based on a Mach-Zehnder structure, a passive polarization splitter was implemented in InGaAsP/InP waveguides. A stack of a dielectric layer and a metal layer deposited on a strip-loaded waveguide can equalize the TE effective indices, while still having a difference in the TM effective indices, at acceptable losses. Over a 60-nm wavelength range, the measured TE (TM) extinction ratios were better than -16 dB (-13 dB), with insertion losses as low as 1.5 dB.

A short review of the characteristics of MMI devices, as compared with other coupling and routing devices, is given at the end of this thesis. It is concluded that MMI devices are very versatile, capable of providing a large set of coupling, splitting and combining functions, with performances and dimensions either comparable or better than conventional devices.

Contents

Chapter 1

Introduction

As we approach the end of the 20th century, the need to process and distribute large amounts of information appears to be ever increasing. In the last fifteen years, optical fibres have replaced copper cables in long-distance and trunk links. This chapter contains a brief history of optical communications and the evolution of practical lightwave systems. The role of fibre and integrated optics, their impact on system engineering and their potential to meet the demands for newer and more powerful information technologies are assessed.

1.1 Optical communications

The early steps of modern optical communication are very much related to the development of suitable optical sources and channels. The invention of the laser [1] in the early 1960s is usually considered to heve been the initial kick. Not only the laser provided a powerful coherent light source and it enhanced the few existing atmospheric propagation links, but it also prompted researchers to seek for a reliable optical channel. In 1966, almost simultaneously, Kao and Hockham [2], and Werts [3] proposed dielectric fibres for the transmission of coherent light, and worked out the basic design parameters of fibres of "glassy material constructed in a cladded structure [...] representing a possible practical optical waveguide with important potential as a new form of communication medium".

The development of techniques for making optical fibres with losses only slightly larger than the theoretical minimum represents an extraordinary engineering achievement. Early fibres used for localized illumination showed attenuation of the order of 5000 dB/km [4]. In 1970 this figure was reduced to 20 dB/km [5]. Today, fibre loss close to 0.2 dB/km in the 1550-nm window is commonplace.

Figure 1.1 shows the attenuation of today's high quality fused silica fibre. This curve is shaped by various loss mechanisms. In the short wavelength region, losses are mainly determined by intrinsic Rayleigh scattering [6], while (intrinsic) vibrational absorption determines

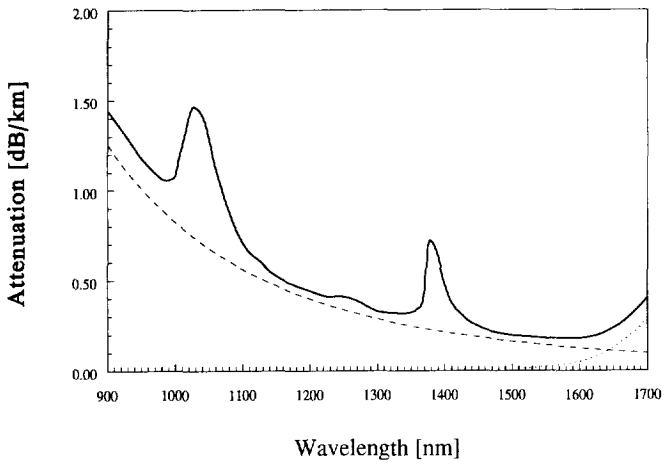

Figure 1.1 Typical measured attenuation constant as a function of wavelength for a high-quality fused-silica single mode optical fibre. Dashed line shows Rayleigh's scattering loss and dotted line shows infra-red vibrational absorption.

the loss in the long wavelength region [7]. In addition, the fundamental stretching vibrations of hydroxyl groups (OH^- ions present in the fibre) in the mid-infrared give rise to overtones, which appear as relatively strong absorption peaks within the communication wavelength range [8]. All the spectral losses combine to give low-loss regions (sometimes referred to as windows), the most notable around 1.30 μm (loss$\approx$0.34 dB/km) and 1.55 μm (loss$\approx$0.19 dB/km), providing a huge transmission bandwidth. A great part of the research strategies and the choice of materials in fibre and integrated optics for optical communications are determined by the wavelength characteristics of the silica fibre, and aim at the efficient utilization of its low-loss and/or low-dispersion regions.

1.2 Early lightwave systems

The first lightwave systems providing better performances than coaxial cables featured graded-index multimode fibres at $\lambda = 0.85$ μm, and made use of already available sources and detectors. Typical systems performed with a loss limit of 2.5 dB/km and a dispersion limit (bandwidth $\times$ distance) of about 2 Gbit/s km. The FT3C metropolitan lightwave system from AT&T [9] with a 10-km repeater spacing at 100 Mbit/s is a good example of such technology.

A big improvement in system performance came with the introduction of single-mode fibres (SMF) (lower loss and no modal dispersion) operating at 1.30-μm wavelength (zero material dispersion for fused silica fibres [10]). Suitable InGaAsP sources and Ge detectors had to be

developed for this wavelength. Two systems of this second generation were commercialized by AT&T [11] and NTT [12] in 1983, with 30–40 km repeater spacing at 200 Mbit/s.

By using the same material technology developed for 1.30-μm systems, the third generation pushes the wavelength to $\lambda = 1.55$ μm, where fibre loss reaches its minimum. Two strategies were proposed to overcome fibre dispersion (about 17 ps/nm.km) at this wavelength: zero-dispersion shifted fibres (DSF) and single-frequency lasers. The zero chromatic dispersion can be made to shift to 1.55-μm wavelength by suitably tailoring the waveguide dispersion [13]. Though practical DSFs have larger attenuation, they were used to demonstrate 140 Mbit/s transmission experiments over 140 km [14]. Distributed feedback (DFB) or distributed Bragg reflector (DBR) lasers —which oscillate in one longitudinal mode, rather than several— have been applied to achieve 420 Mbit/s transmission through 200 km of optical fibre [15].

Coherent optical communication started soon after the invention of the laser. Improved sensitivities over direct detection schemes had already been demonstrated in free space systems in the late 1960s [16]. The concept of coherent optical frequency multiplexing —which could permit an efficient access to the vast optical bandwidth of single-mode fibres— was first proposed in 1970 [17]. The high selectivity of coherent systems should allow frequency division multiplex (FDM) schemes with channel spacings of only a few hundred MHz [18] instead of more than 100 GHz (i.e. 0.6 nm @1.30-μm) achievable by conventional (filtering) wavelength division multiplexing (WDM)*.

Coherent systems achieved considerable successes in the late 1980s. AT&T demonstrated a 3-channel network by narrow-deviation frequency shift keying (FSK) separate DFB lasers at 45 Mbit/s in the 1.30-μm window. The sensitivity of -61 dBm (only 4.5 dB far from the shot-noise limit) and the spacing of 300 MHz indicate for the proposed system a potential throughput of about 4.5 Gbit/s [19]. In 1990, NEC reported on a 10-channel FDM broadcasting system by wide-deviation FSK of ten 1.54-μm DBR lasers at 400 Mbit/s, achieving a sensitivity of -45 dBm for all channels. The system has been estimated to be able to distribute about 80 high definition TV channels to 2000 subscribers by 500 GHz frequency tunable DBR laser diodes [20].

Although transmission of up to 10 Gbit/s over 360 km has been demonstrated through deployed standard (non-DSF) cables [21], installed commercial systems to date work at rates of 1.2, 1.7 Gbit/s [22], and 2.5 Gbit/s.

The main problems which have limited the feasibility and reliability of coherent optical networks are represented by the laser phase noise [23, 24], the random state of polarization at the output of a conventional single-mode fibre [25] and, to a lesser extent, the laser intensity noise. Moreover, laser phase noise is also a serious cause of crosstalk in multichannel systems [26, 27].

A practical way of circumventing the problems associated with phase and polarization fluctuations in coherent receivers is called phase and polarization diversity [28]. The techniques are further explained in Chapter 4 and Chapter 5 respectively, where the realization of a 4×4

*The distinction in the name is made (loosely) on the basis of channel spacing; FDM for spacings < 1 nm, WDM for spacings > 1 nm.

phase diversity network and a polarization splitter are described.

Subcarrier multiplexed (SCM) systems [29] can provide optical multichannel transmission of analogue and/or digital signals by direct detection (DD) of a single intensity-modulated (IM) optical carrier [30]. However, the IM/DD SCM system requires an optical modulator with excellent linearity [31], which ultimately limits the number of multiplexing channels. Accordingly, much research has been done on coherent SCM systems using optical phase and frequency modulation [32].

1.3 The new generations

By the early 1990s, the speed limit of fast silicon (de)multiplexer ICs (somewhere around 30 Gbit/s) seemed to have been reached [33], with hybrid OEICs reported up to 10 Gbit/s [34]. It was clear that future transmission systems would have to rely on a smart share of the resources offered by electronics (logic and memory), and the resources offered by optics (bandwidth, transparency and concurrency).

In order to overcome the electronic limitations, and thus increase the transmission capacity, it was suggested to exploit the fibre bandwidth by wavelength division multiplexing (WDM). Early WDM experiments at 10, 16, and 100 channels achieved aggregated capacities of 20, 32, and 62 Gbit/s respectively [35, 36, 37]. Recently, two major breakthroughs made WDM even more attractive. They are the optical fibre amplifiers and the multiple wavelength laser arrays.

Since the first announcement in 1987 of a high-gain fibre amplifier [38], a huge amount of basic and applied research was devoted to optical amplifiers for communications, especially erbium-doped fibre amplifiers (EDFAs) for 1.55-μm and (more recently) praseodymium-doped fibre amplifiers (PDFAs) for 1.30-μm. The emergence of optical amplification in doped fibres relaunched the debate on direct and coherent detection, the receiver sensitivity no longer being a critical issue. Fibre amplifiers have a relatively large bandwidth (around 30 nm), present low channel crosstalk, are polarization insensitive and bidirectional, and match very well to all existing fibre optics fabric. They are used as high-power low-gain amplifiers to boost signals from laser transmitters [39], as in-line moderate-power cascaded repeaters to periodically amplify the signal in long-distance systems [40], and as low-power low-noise preamplifiers to enhance receiver sensitivity [41]. When operated in a nonlinear mode, they find use as optical gates, pulse shapers and routing switches. Fibre amplifiers have evolved from laboratory prototypes to components making up part of commercial systems in just over five years. The future transpacific TPC-5 [42] and transatlantic TAT-12/13 [43] submarine cables, due to be operational in 1995, are remarkable examples of transmission systems involving hundreds of EDFAs.

Monolithic multi-wavelength laser sources are attractive for WDM systems because a single on-chip thermo-electric cooler can be used to keep the relative wavelength spacing constant. Conventional double heterostructure laser arrays and strained-layer multi-quantum well structures achieve channel spacings ranging from 1 to 10 nm [44, 45]. This allows a

trade-off between ease of demultiplexing versus dense use of the fibre amplifier bandwidth.

The advent of fibre amplifiers has made soliton[†] transmission a reality, the EDFA providing the gain for keeping the required pulse peak power throughout the link. In the first instance, soliton systems have established world records for DSF high speed transmission in long-haul (20 Gbit/s over 1850 km and 40 Gbit/s over 80 km [47]), transoceanic distances (single-channel 10 Gbit/s over 20000 km, and two-channel 10 Gbit/s WDM over 13000 km [48]), and virtually infinite distances (10 Gbit/s over 180×10^6 km [49]). Secondly, although standard (non-DSF) fibres are not the optimum choice for soliton transmission, the huge amount of regular SMF already deployed in the field spurred some research into the upgrading of conventional systems toward soliton operation, with 4 Gbit/s over 310 km and 7 in-line EDFAs [50, 51], and 10 Gbit/s over 204 km with a booster, a preamplifier and one in-line EDFA [52] being demonstrated in standard SMF at 1.55-μm wavelength. Thirdly, soliton-soliton interactions allow quantum-nondemolition (QND) measurements [53] of optical pulses within an optical fibre. Unlike the photodiode detection process, which completely destroys the optical signal, QND amounts to a loss-free tapping of information. Thus, it offers a noninvasive read-out technique that preserves a signal pulse train for further processing or transmission to, in principle, an unlimited number of receivers [54].

1.4 Integrated optics

A long-standing problem in the practical realization of lightwave communication systems has been that of coupling optical energy into and out of the transmission medium (single-mode fibre), accrued in transmitters or receivers containing a number of guided-wave optical and electro-optic devices. The problem arises from the different cross-section sizes of the single-mode fibre core (diameter $\approx$3–10 μm) and the integrated waveguide components (lateral: 2–5 μm, transverse: <1 μm), which produce very dissimilar light beams, and this makes coupling efficiency and stability serious issues.

Integrated optics (IO) aims at the fabrication of these devices and the simultaneous definition of their linking waveguides on a single substrate. The driving force for IO research is the potential for higher performance resulting from stable, low-loss optical coupling between components and the expected reduction in packaging costs. Optoelectronic integrated circuits (OEICs) combine optic, electro-optic and electronic functions on one single chip. Photonic integrated circuits (PICs) can be regarded as a subset of the OEICs, where only (passive) optical devices are integrated.

The integration of a number of guided-wave optical and electro-optic devices on to a single chip evolved hand in hand with the development of new transmission techniques, which required processing of the signal in the optical domain prior to its conversion to the electrical

[†]A soliton is a short (tens of ps), high-power (tens of mW) optical pulse with a hyperbolic secant squared (sech^2) envelope which can propagate in a lossless dispersive medium without changing its shape. This can be achieved because the non-linear refractive index change (Kerr effect) cancels out the dispersive optical pulse broadening [46].

domain [55].

The main application of OEICs has been as photoreceiver front-ends, where the reduction of the parasitics associated with the node connecting the photodiode and the preamplifier is of the utmost importance to ensure wide band operation. So far, and due to the complexities related to the simultaneous optimization of optical and electronic devices, hybrid receivers have offered better performances than OEICs, especially at <10 Gbit/s. This scenario may easily change for applications requiring 20 Gbit/s operation and beyond. Only monolithic integration can provide low-parasitics circuits, and the first 20-GHz bandwidth InP-based integrated photoreceivers are now being reported [56].

In terms of product maturity, the optoelectronics industry is many years behind the electronics industry. For electronic components, advances in performance tend to *follow* advances in manufacturability. In contrast, advances in performance tend to *lead* manufacturing science for optoelectronic components. The absence of a strong optoelectronics manufacturing infrastructure (there is even some discrepancy over the choice of the most suitable material) has created a logjam of prototype devices with very interesting functions, but which have to be, –and may never be– commercialized. Without commercial availability of these devices, systems that could utilize their advanced functions will be implemented instead with alternative technologies and architectures. Only recently, research efforts have turned from creating or improving laboratory components into addressing manufacturability issues.

While the concept of manufacturability may be difficult to define in an absolute sense, it is obvious that performance, cost and reliability are the most important decision elements. Thus, a manufacturable component is one that can meet cost and reliability requirements while maintaining adequate performance. Whereas optoelectronic device performances continue to improve, cost and reliability targets have so far only been met for a few components.

1.5 About this thesis

This thesis deals with integrated optical devices required for signal processing and routing in optical communications. Much of the work here reported has been devoted to the development of optical couplers based on multi-mode interference (MMI). The operation of optical MMI devices is based on the self-imaging principle, explained in Chapter 2. The design, fabrication and experimental results of MMI couplers are presented in Chapter 3. These chapters pay also attention to the theoretical and experimental assessment of fabrication and operation tolerances of the couplers.

Since our first experiments on MMI couplers [57, 58], the MMI concept has proved very versatile and has led to easy-to-design and fabricate, highly performing devices. In addition to their development as single components [59, 60], MMI couplers have been incorporated in more complex OEICs, thus enhancing their functions and improving their characteristics [61].

Chapter 4 demonstrates an early application of MMI couplers in a phase diversity network [62]. Phase diversity (Figure 1.2) is a technique which allows the avoidance of phase locking

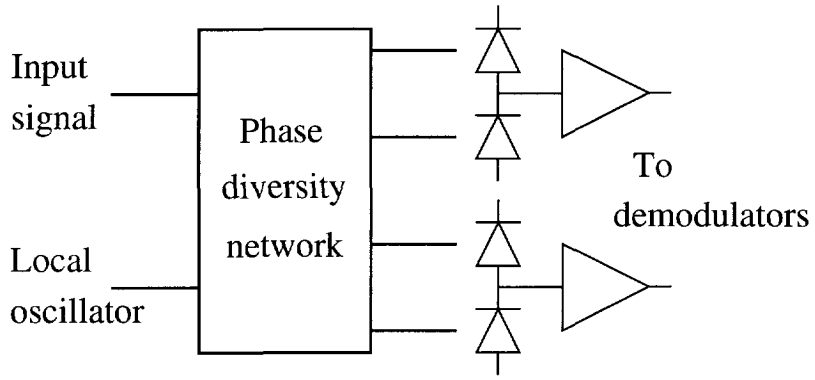

Figure 1.2 A phase diversity network provides quadrature combinations of the input signal and the local oscillator. Such technique allows stable coherent detection in spite of phase noise.

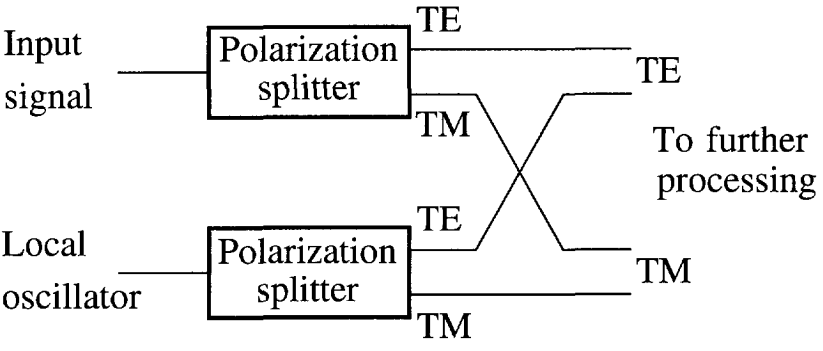

Figure 1.3 A pair of polarization splitters deliver equally-polarized optical fields. This enables the separate processing of the different field components of the input and local oscillator signals (according to their polarization).

in optical coherent receivers, and also relaxes laser linewidths requirements [63].

Chapter 5 describes the realization of a polarization splitter based on a Mach-Zehnder interferometer comprising MMI couplers [64]. Polarization splitters separate the two orthogonal states of polarization of an optical signal, allowing the further processing (combination, detection, etc.) of equally polarized fields (Figure 1.3).

The concepts demonstrated in this thesis are not restricted to a particular material or technology. Most of the devices were fabricated both in silica-based (dielectric) and III-V (semiconductor) waveguides, making use of the technologies developed at the Integrated Optics Group, Delft University of Technology [65, 66, 67]. The underlying principles of operation are fundamental enough to be realized with other materials.

The thesis concludes by comparing the properties of MMI devices with those of more conventional routing and coupling devices.

Chapter 2

The self-imaging principle

This chapter contains the theory of the self-imaging principle. A guided-mode propagation analysis is used to describe the periodic imaging in strongly multimoded step-index optical waveguides. Different imaging patterns are distinguished according to the modal excitation. A simple criterion is given to evaluate the imaging resolution of a multimode waveguide. Fabrication and operation tolerances are calculated.

2.1 Introduction

Self-imaging of periodic objects illuminated by coherent light was first described more than 150 years ago [68]. Self-focusing (graded index) waveguides can also produce periodic real images of an object [69]. However, the possibility of achieving self-imaging in uniform index slab waveguides was first suggested by Bryngdahl [70] and explained in more detail by Ulrich [71, 72].

The principle can be stated as follows: *Self-imaging is a property of multimode waveguides by which an input field profile is reproduced in single or multiple images at periodic intervals along the propagation direction of the guide.*

2.2 Multimode waveguides

A full-modal propagation analysis is probably the most comprehensive theoretical tool to describe self-imaging phenomena in multimode waveguides. It not only supplies the basis for numerical modelling and design, but it also provides insight into the mechanism of multimode interference. Other approaches make use of ray optics [73], hybrid methods [74], or BPM type simulations. We follow here the guided-mode propagation analysis (MPA), proposed first in [72] for the formulation of the periodic imaging. The method decomposes an input field

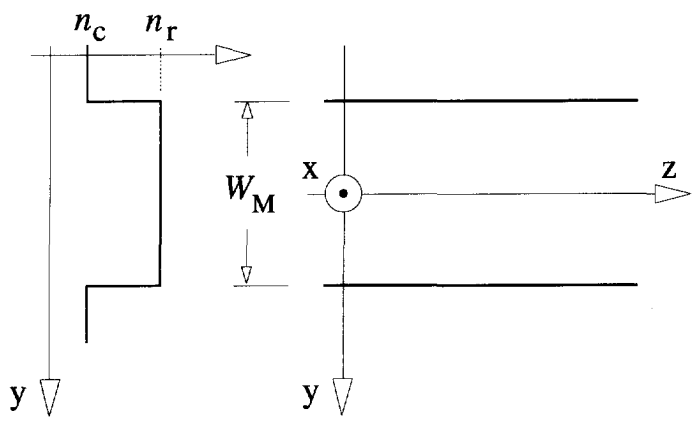

Figure 2.1 Two-dimensional representation of a step-index multimode waveguide; (effective) index lateral profile (left), and top view of ridge boundaries and coordinate system (right).

into all guided mode fields, propagates each of these modes independently, and calculates the output field by recombining the propagated mode fields. Reflecting this method of analysis, the mechanism is called *multimode interference* (MMI).

The central structure of an MMI device is a waveguide designed to support a large number of modes (typically ≥ 3). In order to launch light into and recover light from that multimode waveguide, a number of access (usually single-moded) waveguides are placed at its beginning and at its end. Such devices are generally referred to as *N×M MMI couplers*, where N and M are the number of input and output waveguides respectively.

Self-imaging may exist in three-dimensional multimode structures [75], for which MPA combined with two-dimensional (finite-element or finite-difference methods) cross-section calculations can provide a useful simulation tool [76]. However, the current trend of etch-patterning produces step-index waveguides, which are, in general, single-moded in the transverse direction. As the lateral dimensions are much larger than the transverse dimensions, it is justified to assume that the modes have the same transverse behaviour everywhere in the waveguide. The problem can thus be analyzed using a two-dimensional (lateral and longitudinal) structure, such as the one depicted in Fig. 2.1. The analysis hereafter is based on such a 2-D representation of the multimode waveguide, which can be obtained from the actual 3-D physical multimode waveguide by several techniques, such as the effective index method (EIM) [77] or the spectral index method (SIM) [78].

2.2.1 Propagation constants

Figure 2.1 shows a step-index multimode waveguide of width W_{M}, ridge (effective) refractive index n_r and cladding (effective) refractive index n_c. The waveguide supports m lateral modes (as shown in Fig. 2.2) with mode numbers $\nu = 0, 1, \ldots (m-1)$ at a free-space wavelength λ. The lateral wavenumber $k_{y\nu}$ and the propagation constant β_ν are related to the ridge index n_r by the dispersion equation

$$k_{y\nu}{}^2 + \beta_\nu{}^2 = k_0^2\, n_r^2 \tag{2.1}$$

with

$$k_0 = \frac{2\pi}{\lambda} \tag{2.2}$$

$$k_{y\nu} = \frac{(\nu+1)\,\pi}{W_{e\nu}} \tag{2.3}$$

where the "effective" width $W_{e\nu}$ takes into account the (polarization-dependent) lateral penetration depth of each mode field, associated with the Goos-Hähnchen shifts at the ridge boundaries. For high-contrast waveguides, the penetration depth is very small so that $W_{e\nu} \approx W_{\mathrm{M}}$. In general, the effective widths $W_{e\nu}$ can be approximated by the effective width W_{e0} corresponding to the fundamental mode [79]. It will be noted W_{e}, for simplicity, and is given by [73]:

$$W_{e\nu} \approx W_{\mathrm{e}} \approx W_{\mathrm{M}} + \left(\frac{\lambda}{\pi}\right)\left(\frac{n_c}{n_r}\right)^{2\sigma} \frac{1}{\mathrm{NA}} \tag{2.4}$$

where $\sigma = 0$ for TE, $\sigma = 1$ for TM, and NA is the lateral numerical aperture defined as

$$\mathrm{NA} \doteq \sqrt{n_r^2 - n_c^2} \tag{2.5}$$

By using the binomial expansion with $k_{y\nu}^2 \ll k_0^2 n_r^2$, the propagation constants β_ν can be deduced from Eq. (2.1), (2.2) and (2.3):

$$\beta_\nu \approx k_0\, n_r - \frac{(\nu+1)^2\,\pi\,\lambda}{4\, n_r\, W_e^2} \tag{2.6}$$

Therefore, the propagation constants in a step-index multimode waveguide show a nearly quadratic dependence with respect to the mode number ν.

By defining L_π as the beat length of the two lowest-order modes

$$L_\pi \doteq \frac{\pi}{\beta_0 - \beta_1} \approx \frac{4\, n_r\, W_{\mathrm{e}}^2}{3\,\lambda} \tag{2.7}$$

the propagation constants spacing can be written as

$$(\beta_0 - \beta_\nu) \approx \frac{\nu(\nu+2)\,\pi}{3\, L_\pi} \tag{2.8}$$

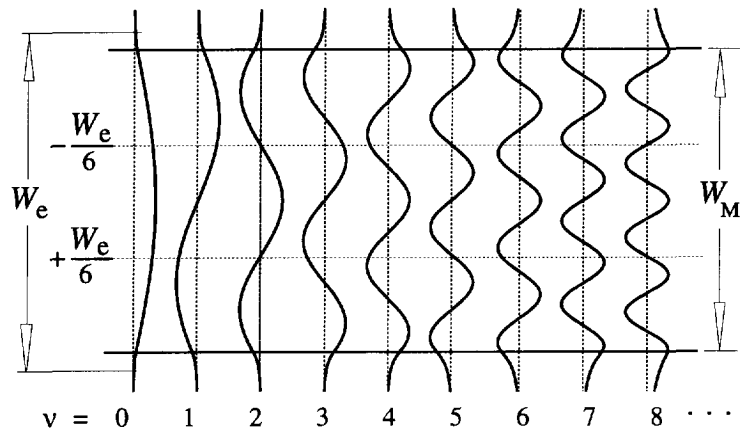

Figure 2.2 Example of amplitude-normalized lateral field profiles $\psi_\nu(y)$, corresponding to the first 9 guided modes in a step-index multimode waveguide.

2.2.2 Guided-mode propagation analysis

An input field profile $\Psi(y,0)$ imposed at $z = 0$ and totally contained within W_e (Fig. 2.3), will be decomposed into the modal field distributions $\psi_\nu(y)$ of all modes:

$$\Psi(y,0) = \sum_\nu c_\nu \, \psi_\nu(y) \tag{2.9}$$

where the field excitation coefficients c_ν can be estimated using overlap integrals

$$c_\nu = \frac{\int \Psi(y,0) \, \psi_\nu(y) \, dy}{\sqrt{\int \psi_\nu^2(y) \, dy}} \tag{2.10}$$

based on the field-orthogonality relations.

If the "spatial spectrum" of the input field $\Psi(y,0)$ is narrow enough not to excite unguided modes, (a condition satisfied for all practical applications), it may be decomposed into the *guided* modes alone:

$$\Psi(y,0) = \sum_{\nu=0}^{m-1} c_\nu \, \psi_\nu(y) \tag{2.11}$$

The field profile at a distance z can then be written as a superposition of all the guided mode field distributions

$$\Psi(y,z) = \sum_{\nu=0}^{m-1} c_\nu \, \psi_\nu(y) \, \exp\left[j(\omega t - \beta_\nu z)\right] \tag{2.12}$$

Taking the phase of the fundamental mode as a common factor out of the sum, dropping it and assuming the time dependence $\exp(j\omega t)$ implicit hereafter, the field profile $\Psi(y,z)$ becomes

$$\Psi(y,z) = \sum_{\nu=0}^{m-1} c_\nu \, \psi_\nu(y) \, \exp\left[j(\beta_0 - \beta_\nu)z\right] \tag{2.13}$$

A useful expression for the field at a distance $z = L$ is then found by substituting Eq. (2.8) into Eq. (2.13):

$$\Psi(y,L) = \sum_{\nu=0}^{m-1} c_\nu \, \psi_\nu(y) \, \exp\left[j \, \frac{\nu(\nu+2)\pi}{3\,L_\pi} L\right] \tag{2.14}$$

The shape of $\Psi(y,L)$, and consequently the types of images formed, will be determined by the modal excitation c_ν, and the properties of the mode phase factor

$$\exp\left[j \, \frac{\nu(\nu+2)\pi}{3\,L_\pi} L\right] \tag{2.15}$$

It will be seen that, under certain circumstances, the field $\Psi(y,L)$ will be a reproduction (self-imaging) of the input field $\Psi(y,0)$. We call *General Interference* to the self-imaging mechanisms which are independent of the modal excitation; and *Restricted Interference* to those which are obtained by exciting certain modes alone.

The following properties will prove useful in later derivations:

$$\nu\,(\nu+2) = \begin{cases} \text{even for } \nu \text{ even} \\ \text{odd for } \nu \text{ odd} \end{cases} \tag{2.16}$$

and,

$$\psi_\nu(-y) = \begin{cases} \psi_\nu(y) & \text{for } \nu \text{ even} \\ -\psi_\nu(y) & \text{for } \nu \text{ odd} \end{cases} \tag{2.17}$$

the latter being a consequence of the structural symmetry with respect to the plane $y = 0$.

2.3 General interference

This section investigates the interference mechanisms which are independent of the modal excitation, that is, we pose no restriction on the coefficients c_ν and explore the periodicity of Eq. (2.15).

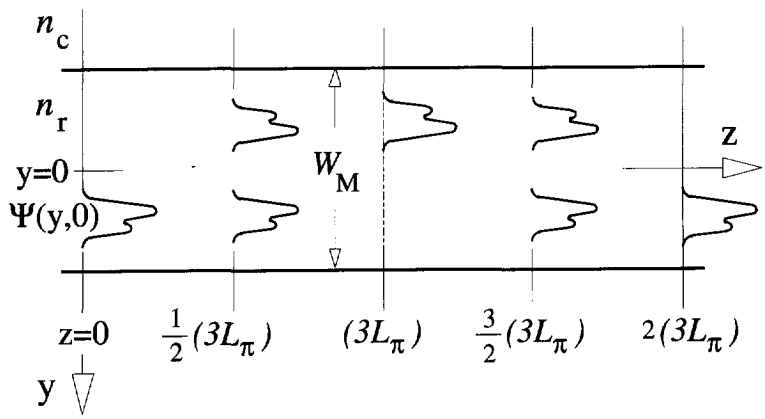

Figure 2.3 Multimode waveguide showing the input field $\Psi(y,0)$, a mirrored single image at $(3L_\pi)$, a direct single image at $2(3L_\pi)$, and two-fold images at $\frac{1}{2}(3L_\pi)$ and $\frac{3}{2}(3L_\pi)$.

2.3.1 Single images

By inspecting Eq. (2.14), it can be seen that $\Psi(y,L)$ will be an image of $\Psi(y,0)$ if

$$\exp\left[j\,\frac{\nu(\nu+2)\pi}{3\,L_\pi}L\right] = 1 \quad \text{or} \quad (-1)^\nu \tag{2.18}$$

The first condition means that the phase changes of all the modes along L must differ by integer multiples of 2π. In this case, all guided modes interfere with the same relative phases as in $z = 0$; the image is thus a *direct* replica of the input field. The second condition means that the phase changes must be alternatively even and odd multiples of π. In this case, the even modes will be in phase and the odd modes in antiphase. Because of the odd symmetry stated in Eq. (2.17), the interference produces an image *mirrored* with respect to the plane $y = 0$.

Taking into account Eq. (2.16), it is evident that the first and second condition of Eq. (2.18) will be fulfilled at

$$L = p\,(3L_\pi) \quad \text{with} \quad p = 0, 1, 2, \ldots \tag{2.19}$$

for p even and p odd, respectively. The factor p denotes the periodic nature of the imaging along the multimode waveguide. Direct and mirrored single images of the input field $\Psi(y,0)$ will therefore be formed by general interference at distances z that are, respectively, even and odd multiples of the length $(3L_\pi)$, as shown in Fig. 2.3. It should be clear at this point that the direct and mirrored single images can be exploited in bar- and cross-couplers, respectively.

Next, we investigate multiple imaging phenomena, which provide the basis for a broader range of MMI couplers.

2.3.2 Multiple images

In addition to the *single* images at distances given by Eq. (2.19), *multiple* images can be found as well. Let us first consider the images obtained half-way between the direct and mirrored image positions, i.e., at distances

$$L = \frac{p}{2}\,(3L_\pi) \quad \text{with} \quad p = 1, 3, 5, \ldots \tag{2.20}$$

The total field at these lengths is found by substituting Eq. (2.20) into Eq. (2.14):

$$\Psi(y, \frac{p}{2}3L_\pi) = \sum_{\nu=0}^{m-1} c_\nu\, \psi_\nu(y)\, \exp\left[j\,\nu(\nu+2)\,p\left(\frac{\pi}{2}\right)\right] \tag{2.21}$$

with p an odd integer. Taking into account the property of Eq. (2.16) and the mode field symmetry conditions of Eq. (2.17), Eq. (2.21) can be written as

$$\begin{aligned}\Psi(y, \frac{p}{2}3L_\pi) &= \sum_{\nu \text{ even}} c_\nu\, \psi_\nu(y) + \sum_{\nu \text{ odd}} (-j)^p\, c_\nu\, \psi_\nu(y) \\ &= \frac{1+(-j)^p}{2}\,\Psi(y,0) + \frac{1-(-j)^p}{2}\,\Psi(-y,0)\end{aligned} \tag{2.22}$$

The last equation represents a pair of images of $\Psi(y,0)$, in quadrature and with amplitudes $1/\sqrt{2}$, at distances $z = \frac{1}{2}(3L_\pi), \frac{3}{2}(3L_\pi), \ldots$ as shown in Fig. 2.3. This two-fold imaging can be used to realize 2×2 3-dB couplers.

Optical 2×2 MMI couplers based on the single and two-fold imaging by general interference have been realized in III-V semiconductor waveguides [58, 80], in silica-based dielectric waveguides [81], and in non-lattice matched III-V quantum wells [82, 83]. Figure 2.4 shows the schematic layout of a 2×2 general interference MMI coupler [58, 80]. Note that, because of the excitation independence, the access waveguides can be positioned close to the lateral boundaries of the multimode section, which maximizes the gap. This decreases coupling between access waveguides and obviates blunting due to poor photolithography resolution.

In general, multi-fold images are formed at intermediate z-positions [73, 75]. Analytical expressions for the positions and phases of the N-fold images have been obtained [84] by using Fourier analysis and properties of generalized Gaussian sums. The starting point is to introduce a field $\Psi_{\text{in}}(y)$ as the periodic extension of the input field $\Psi(y,0)$; antisymmetric with respect to the guide boundary, and with periodicity $2W_{\text{e}}$:

$$\Psi_{\text{in}}(y) \doteq \sum_{v=-\infty}^{\infty} \left[\Psi(y - v2W_{\text{e}}, 0) - \Psi(-W_{\text{e}} - y - v2W_{\text{e}}, 0)\right] \tag{2.23}$$

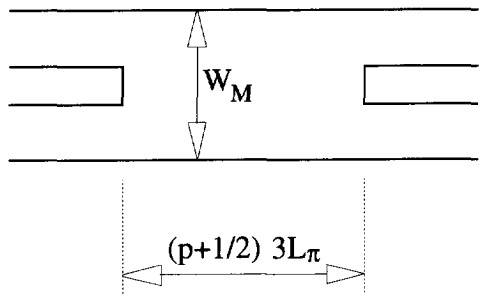

Figure 2.4 Basic layout of a 2×2 MMI coupler based on the general interference mechanism [80].

and to approximate the mode field amplitudes by (co)sine-like functions

$$\psi_\nu(y) \approx \begin{cases} \cos(k_{y\nu}y) & \text{for } \nu \text{ even} \\ \sin(k_{y\nu}y) & \text{for } \nu \text{ odd} \end{cases} \tag{2.24}$$

The spatially-periodic descriptions of the input field and guided modes made above is justified in so far as the lateral boundaries of the multimode waveguide act as parallel mirrors, providing repeated reflections of the fields within $y \leq |W_e/2|$, thereby creating a virtual periodic object of periodicity $2W_e$. It is interesting to note that, from this point of view, a multimode waveguide can be regarded as a kaleidoscope*.

Based on these periodic descriptions, Eq. (2.11) can be interpreted as a (spatial) Fourier expansion, and it is shown [84] that, at distances

$$L = \frac{p}{N}\ (3L_\pi) \tag{2.25}$$

where $p \geq 0$ and $N \geq 1$ are integers having no common divisor, the field will be of the form

$$\Psi(y, L) = \frac{1}{C} \sum_{q=0}^{N-1} \Psi_{\text{in}}(y - y_q)\ \exp(j\varphi_q) \tag{2.26}$$

with

$$y_q = \frac{p}{N}(2q - N)W_e \quad \text{with } q = 0, 1, \ldots N-1 \tag{2.27}$$

*A kaleidoscope is a tube with bright, loose objects at the bottom end and reflecting parallel inner walls, invented by David Brewster (British Patent No. 4136, 30 August 1817). The multiple images formed by the mirrors can be seen through an eye-piece at the top end.

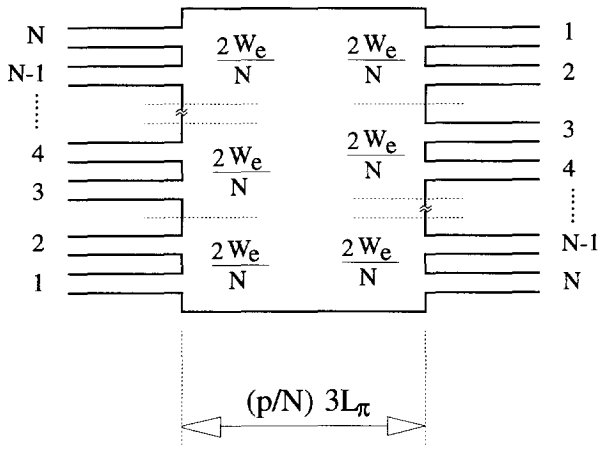

Figure 2.5 Layout of an N×N MMI coupler, for the case of N even [84].

$$\varphi_q = \frac{p}{N}(N-q)q\pi \tag{2.28}$$

where C is a complex normalization constant with $|C| = \sqrt{N}$, p indicates the imaging periodicity along z, and q refers to each of the N images along y.

The above equations show that, at distances given by Eq. (2.25), N images are formed of the *extended* field $\Psi_{\text{in}}(y)$, equally spaced across the interval $-3W_e/2 \leq y \leq W_e/2$, each with amplitude $1/\sqrt{N}$ and phase φ_q. This leads to N images of the *input* field $\Psi(y,0)$ (generally not equally spaced) within the physical guide (interval $|y| \leq W_e/2$). The multiple self-imaging mechanism allows for the realization of $N\times N$ or $N\times M$ optical couplers [85, 86, 87, 88]. Shortest devices are obtained for $p = 1$. Figure 2.5 shows the layout of an N×N MMI coupler for the case of N even.

2.4 Restricted interference

Thus far, no restrictions have been placed on the modal excitation. This section investigates the possibilities and realizations of MMI couplers in which only some of the guided modes in the multimode waveguide are excited by the input field(s). This selective excitation reveals interesting multiplicities of $\nu(\nu+2)$, which allow new interference mechanisms through shorter periodicities of the mode phase factor of Eq. (2.15).

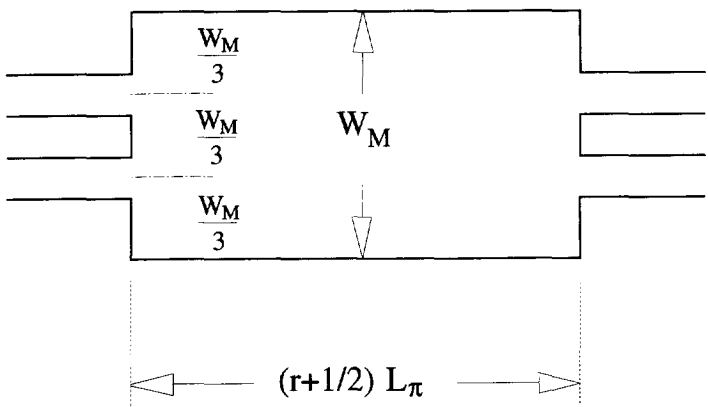

Figure 2.6 Layout of a 2×2 MMI coupler based on paired interference.

2.4.1 Paired interference

By noting that

$$\text{mod}_3[\nu(\nu+2)] = 0 \quad \text{for } \nu \neq 2, 5, 8, \ldots \tag{2.29}$$

it is clear that the length periodicity of the mode phase factor of Eq. (2.15) will be reduced three times if

$$c_\nu = 0 \quad \text{for } \nu = 2, 5, 8, \ldots \tag{2.30}$$

Therefore, as shown in [65, 59], single (direct and inverted) images of the input field $\Psi(y, 0)$ will now be obtained at (cf. Eq. (2.19))

$$L = p\,(L_\pi) \quad \text{with } p = 0, 1, 2, \ldots \tag{2.31}$$

provided that the modes $\nu = 2, 5, 8, \ldots$ are not excited in the multimode waveguide. By the same token, two-fold images will be found at $(p/2)L_\pi$ with p odd. Appendix 2A provides a mathematical verification of the direct, mirrored and two-fold restricted interferences. In general, N-fold images will be formed at distances (cf. Eq. (2.25))

$$L = \frac{p}{N}\,(L_\pi) \tag{2.32}$$

where $p \geq 0$ and $N \geq 1$ are integers with no common divisor.

One possible way of attaining the selective excitation of Eq. (2.30) is by launching an even symmetric input field $\Psi(y,0)$ (for example, a Gaussian beam) at $y = \pm W_e/6$. At these positions, the modes $\nu = 2,5,8,\ldots$ present a zero with odd symmetry, as shown in Fig. 2.2. The overlap integrals of Eq. (2.10) between the (symmetric) input field and the (antisymmetric) mode fields will vanish and therefore $c_\nu = 0$ for $\nu = 2,5,8,\ldots$ The number of input waveguides is in this case limited to two, and they should be positioned at 1/3 and 2/3 across the multimode waveguide width, as shown in Fig. 2.6.

When the selective excitation of Eq. (2.30) is fulfilled, the modes contributing to the imaging are paired, i.e. the mode pairs 0-1, 3-4, 6-7,...provide increasing orders of symmetric and antisymmetric functions for the (de)composition of the input field, thus the name of *paired* interference. Two-mode interference (TMI) can be regarded in this context as a particular case of paired interference.

We have demonstrated 2×2 MMI couplers based on the paired interference mechanism, in silica-based dielectric rib-type waveguides with multimode section lengths of 240 μm (cross state) and 150 μm (3-dB state) [57, 89]. Insertion loss lower than 0.4 dB, imbalance below 0.2 dB, extinction ratio of -18 dB, and polarization-sensitivity loss penalty of 0.2 dB were reported for structures supporting from 7 to 9 modes. Calculations predict that power excitation coefficients as low as -40 dB for the modes $\nu = 2,5,8$ can be achieved through a correct positioning of the access waveguides, remaining below -30 dB for a 0.1-μm misalignment [59]. Chapter 3 contains a description of these experiments.

2.4.2 Symmetric interference

Optical N-way splitters can in principle be realized on the basis of the general N-fold imaging at lengths given by Eq. (2.25). However, by exciting only the even symmetric modes, 1-to-N beam splitters can be realized with multimode waveguides four times shorter [90].

In effect, by noting that

$$\mathrm{mod}_4[\nu(\nu+2)] = 0 \quad \text{for } \nu \text{ even} \tag{2.33}$$

it is clear that the length periodicity of the mode phase of Eq. (2.15) will be reduced four times if

$$c_\nu = 0 \quad \text{for } \nu = 1,3,5,\ldots \tag{2.34}$$

Therefore, single images of the input field $\Psi(y,0)$ will now be obtained at (cf. Eq. (2.19))

$$L = p\left(\frac{3L_\pi}{4}\right) \quad \text{with } p = 0,1,2,\ldots \tag{2.35}$$

if the odd modes are not excited in the multimode waveguide. This condition can be achieved by centre-feeding the multimode waveguide with a symmetric field profile. The imaging is

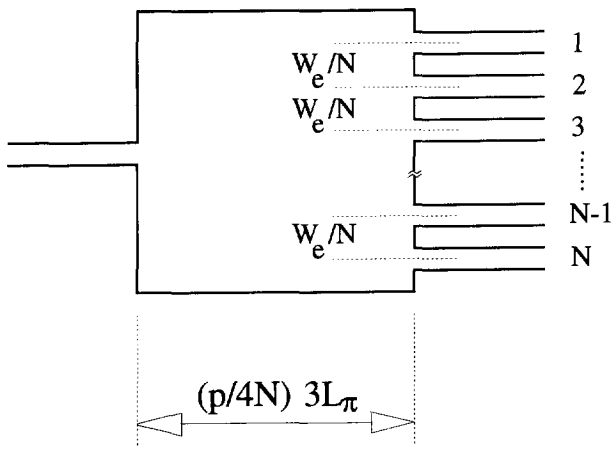

Figure 2.7 Layout of a 1×N MMI splitter/combiner.

obtained by linear combinations of the (even) symmetric modes, and the mechanism will be called *symmetric* interference.

In general, N-fold images will be obtained [91] at distances (cf. Eq. (2.25))

$$L = \frac{p}{N}\left(\frac{3L_\pi}{4}\right) \tag{2.36}$$

with N images of the input field $\Psi(y,0)$, symmetrically located along the y-axis with equal spacings W_e/N [90], and with (relative) phases [92]

$$\phi_s = \phi_0 + \frac{\pi}{N}(s-1)(N-s) \quad \text{with } s = 1,2,3,\ldots \tag{2.37}$$

The simplest way to comply with the selective excitation of Eq. (2.34) is to centre-feed the multimode waveguide with a symmetric input field. Figure 2.7 shows the layout of a 1×N MMI coupler.

A point worth noting is that it is not possible to obtain accurate images for N indefinitely large, as Eqs. (2.25), (2.32) and (2.36) might suggest. The reason is that functions with high spatial frequency (i.e. high-order modes) are needed to provide a resolvable reconstruction of the input field. As a rule of thumb, in order to obtain low-loss well-balanced 1-to-N splitting of a Gaussian field, the multimode waveguide is required to support at least $m = N+1$ modes. As an example, Fig. 2.8 shows the (BPM-calculated) field evolution in a centre-fed multimode waveguide. The field at the end of the multimode section is a five-fold image of the (Gaussian) input field. At shorter distances, 1×6 and 1×7 splitting can be observed. At even shorter

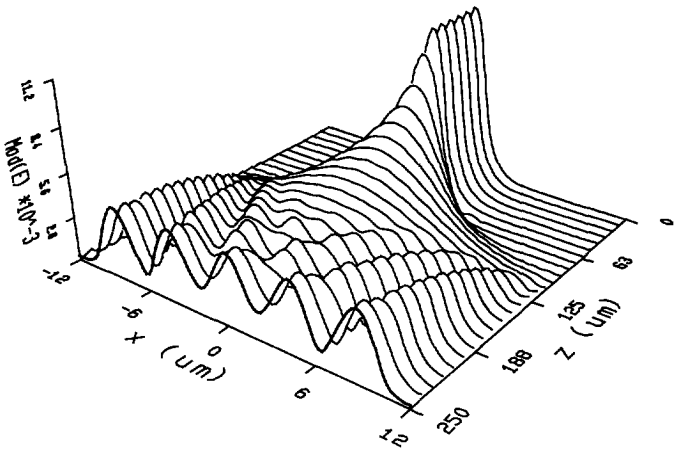

Figure 2.8 BPM simulation of a 20 μm-wide, 200 μm-long multimode waveguide, centre-fed by a Gaussian field through a 2 μm-wide, 50 μm-long single-mode waveguide. The input field at $z = 50$ μm is five-fold imaged at $z = 250$ μm.

distances, the field presents important droops at the sides (giving rise to imbalance) and the images are no longer resolvable (giving rise to excess loss).

A number of $1 \times N$ waveguide splitters/combiners covering a wide range of different multimode guide widths (12–48 μm) and lengths (250–3800 μm) have been demonstrated in GaAs- and InP-based rib waveguides which divide power with 0.36-dB imbalance between N output guides, for values of N between 2 and 20 [91, 93, 94].

We demonstrated extremely short splitters (20–30 μm for silica-based and 50–70 μm for InP-based waveguides), with excess losses of around 1 dB and imbalances below 0.15 dB [60], in agreement with numerical predictions [95, 96]. These experiments are presented in Chapter 3.

2.5 Discussion

Table 2.1 summarizes some characteristics of the general, paired and symmetric interference mechanisms.

It is important to note that general interference mechanisms are independent of the position and shape of the input fields. This fact not only makes design extremely easy but also allows the use of any form of input field profile as well as of the access waveguides, such as very sharp bends.

Restricted interference mechanisms, however, can provide shorter $2 \times N$ couplers and $1 \times N$

Interference mechanism	*General*	*Paired*	*Symmetric*
Inputs × Outputs	$N \times N$	$2 \times N$	$1 \times N$
First single image distance	$(3\ L_\pi)$	(L_π)	$(3\ L_\pi)/4$
First N-fold image distance	$(3\ L_\pi)/N$	$(L_\pi)/N$	$(3\ L_\pi)/4\ N$
Excitation requirements	none	$c_\nu = 0$ for $\nu = 2, 5, 8 \ldots$	$c_\nu = 0$ for $\nu = 1, 3, 5 \ldots$
Input(s) location(s)	any	$y = \pm W_e/6$	$y = 0$

Table 2.1 Summary of characteristics of the general, paired and symmetric interference mechanisms.

splitters at the cost of supplying well-located and reasonably symmetric input field(s) in order to comply with the selective modal excitation requirements of Eq. (2.30) and Eq. (2.34), respectively.

For the case of 2×2 couplers, paired interference actually leads to longer devices than those based on the general interference mechanism. The selective excitation requirement dictates an increase in the multimode waveguide width –and therefore in its length (*see* Eq. (2.7))– which cancels out the potential length reduction. This can be easily verified by considering a pair of input waveguides of width w with a gap assumed to be $w/2$. The multimode section widths are then $5w/2$ for the general interference, and $9w/2$ for the paired interference. Substituting these values in Eqs. (2.7), (2.19) and (2.31), the multimode section lengths are found to be $50 n_r w^2/4\lambda$ for the general interference, and $54 n_r w^2/4\lambda$ for the paired interference. Thus, for a gap equal to $w/2$, paired interference leads to an 8% *longer* multimode section than general interference.

However, general interference mechanisms in weakly guiding structures may suffer from higher losses than paired interference, due to decreased image resolution (Section 2.7.2). The access waveguides positioned at the corners of the multimode waveguide (Fig. 2.4) cause the image to be reconstructed mainly by the (wider) outer lobes of the high order modes (*see also* [76]).

2.6 Loss, balance and phases

For many applications, balancing is even more important than excess loss. In coherent detection techniques for example, the balancing of the output powers of the 3-dB coupler determines the suppression of the relative intensity noise (RIN) noise of the local oscillator laser. And when 3-dB couplers are used in Mach-Zehnder modulators or switches, the balancing directly translates into extinction ratio and cross-talk. With respect to balancing, MMI devices operate fundamentally different from directional couplers. The output powers of a directional coupler

are proportional to $\cos^2(\pi z/2L_\pi)$ and $\sin^2(\pi z/2L_\pi)$, causing the sensitivity of the transmission to length variations to be maximum at the 3-dB point, and of opposite sign for each output. The powers at the output ports of an MMI device, however, reach local maxima around the 3-dB point (or any other N-fold imaging condition). Therefore, the output powers *decrease similarly* for changes in any parameter around the optimum design condition. In other words, the losses increase, but the imbalance remains very low. Something similar happens with the output phases; as they are inherently linked to the imaging reconstruction (*see* Eq. (2.28)) their behaviour follows a local stable pattern around the optimum design conditions.

2.7 Imaging quality

Imaging quality refers to how accurately the input field is reproduced at the end of the multimode waveguide.

2.7.1 Aberration

The quadratic dependence of the propagation constants with the mode number, found in Eq. (2.6), is an approximation. This means that the guided modes will actually accumulate small deviations from the calculated phases at the imaging distances, which tend to blurr the reconstructed image field. The situation is somewhat similar to the focal shift from paraxial rays prediction due to aberration in optical systems of finite aperture. However, some balancing of the phase errors —and thus an improvement of the imaging quality— is possible by a slight correction of the imaging lengths predicted by Eqs. (2.25), (2.32) and (2.36) [97].

2.7.2 Image resolution and contrast

The imaging quality of a multimode waveguide can be formally evaluated with its line-spread function (LSF) [97]. The LSF represents the complex image field of an infinitely narrow input field. An imaging system of high resolution and good contrast is characterized by a narrow-peak and low-ripple LSF.

In device terms, a narrow-peak and low-ripple LSF means low insertion loss and low crosstalk, respectively. The characteristics of the LSF are given by the discrete modal amplitude spectrum c_ν from Eq. (2.10). A flat mode amplitude spectrum (i.e., all guided modes equally excited) with a sharp cut-off will produce a maximally narrow but heavily rippled LSF, as shown in Fig. 2.9. Conversely, a ripple-free but broader LSF can be obtained by a smooth roll-off in the mode spectrum (i.e., gradually decreasing excitation coefficients for the higher-order modes), as shown in Fig. 2.10.

A simpler way of estimating the imaging resolution of a multimode waveguide is as follows. As the image field is a linear combination of the guided mode fields, the narrowest obtainable image in a multimode waveguide, and thus its resolution ρ, will be roughly equal to the cosine-like lobe width of the highest supported mode (i.e., its spatial half-period, see Fig. 2.2):

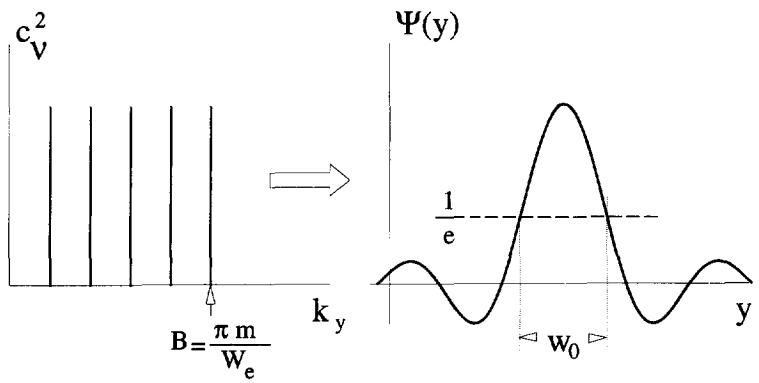

Figure 2.9 A flat (sharp cutoff) modal excitation spectrum and its associated line-spread (sinc) function. From a spatial Fourier analysis, the $1/e$ amplitude width is found to be $w_0 \approx 4.40/B = 1.40W_e/m$.

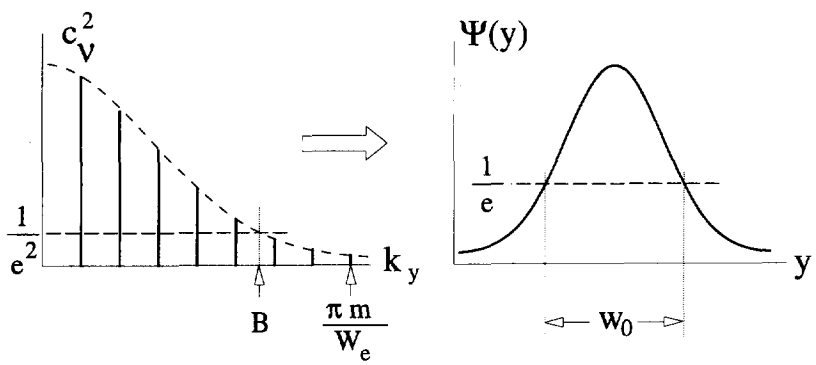

Figure 2.10 A Gaussian modal excitation spectrum and its associated line-spread (Gaussian) function. From a spatial Fourier analysis, the $1/e$ amplitude width is found to be $w_0 = 4/B$. Taking $B \approx (2/3)\pi m/W_e$, the line width becomes $w_0 \approx 1.91W_e/m$.

$$\rho \approx \frac{W_e}{m} \tag{2.38}$$

Despite the crudeness of its postulates, this analysis provides a rather accurate estimation of the imaging resolution. A more elaborate analysis, involving the calculation of the LSF [97], predicts a FWHM (full-width half-maximum) resolution ranging from $0.89W_e/m$ (for a flat mode spectrum) to approximately $1.50W_e/m$ (for a Gaussian mode spectrum). Practical MMI devices usually have smoothly decaying mode spectra, resembling Gaussian shapes.

For a given width of the multimode waveguide, the resolution ρ is determined by the number of guided modes m. The number of guided modes, in turn, is determined by the lateral refractive index contrast in ridge (rib) waveguides, whereas it is determined by the transverse contrast in deeply etched (raised-strip) waveguides.

For rib-type structures, as used for the demonstration of the devices in this thesis, the number of modes propagating in a strongly multimode waveguide (though an integer number) can be estimated as

$$m \approx \frac{V}{\pi} \tag{2.39}$$

where the lateral V parameter is defined as

$$V \doteq \frac{2\pi}{\lambda} W_M \sqrt{n_r^2 - n_c^2} \tag{2.40}$$

Making the approximation $W_e \approx W_M$ and substituting these equations into Eq. (2.38) yields

$$\rho \approx \frac{\lambda}{2\sqrt{n_r^2 - n_c^2}} \tag{2.41}$$

It is interesting to note that, with the definition of the lateral numerical aperture of a step-index waveguide given in Eq. (2.5), the imaging resolution of a multimode waveguide results

$$\rho \approx \frac{\lambda}{2\mathrm{NA}} \tag{2.42}$$

which coincides with the diffraction-limited resolution of a (bulk) optical system. Figure 2.11 plots Eq. (2.42) for $\lambda = 1.55$ μm.

2.8 Tolerances

Relaxed tolerances are important for fabrication as well as for operating conditions. Fabrication tolerances refer to the control of the geometrical dimensions during processing and their subsequent impact on device performance. Operation tolerances relate to the device behaviour

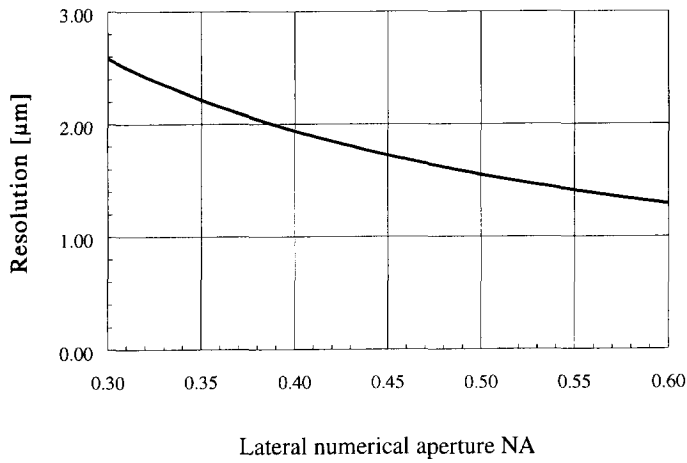

Figure 2.11 Imaging resolution of a multimode waveguide as a function of its lateral numerical aperture, calculated with Eq. (2.42) for $\lambda = 1.55$ μm.

for changes in the wavelength, polarization, temperature, input field distribution, and refractive index.

The relative effect of small finite changes of (some of) these parameters on device performance can be estimated by the change caused in the beat length L_π. Hence, from Eqs. (2.7) and Eq. (2.19)

$$\frac{\delta L_\pi}{L_\pi} = \frac{\delta L}{L} = 2\frac{\delta W_e}{W_e} \approx \frac{|\delta\lambda|}{\lambda} \tag{2.43}$$

This equation says, for example, that a 2% change in the length of the multimode waveguide L, a 1% change in its width W_e, or a 2% change in the operating wavelength λ will all produce the same 1% change in the beat length L_π (and therefore, the same performance degradation). Alternatively, it can be said that a 1% change in the width can be compensated by an (opposite) 2% change in the length, etc. The calculations of the wavelength and etch depth dependence are developed in Appendices 2B and 2C.

The loss penalty produced by a (small) finite shift δL in the z-position of the output waveguides has been evaluated [98] by considering each image as a Gaussian beam focused at a self-image distance $z = L$, and then overlapping the defocused beam with the output waveguide mode field. It was found that the length shift δL which produces a loss penalty $\mathcal{L}$ (expressed in dB) is

$$\delta L = 2Z(\mathcal{L}[\text{dB}]) \left[\frac{\pi\, n_r\, w_0^2}{4\,\lambda}\right] \tag{2.44}$$

where the bracketed factor is the Rayleigh range†, w_0 is the Gaussian beam waist, and equals the width of the input field $\Psi(y,0)$. Z is a rather complicated function [98] of the loss penalty $\mathcal{L}$ but, for $\mathcal{L} \geq 0.5$ dB, it can be well approximated by

$$Z(\mathcal{L}[\text{dB}]) \approx 0.49\mathcal{L}[\text{dB}] + 0.26 \tag{2.45}$$

Eq. (2.44) can be interpreted as an absolute length tolerance, which does not depend on the dimensions of the multimode waveguide. An important conclusion is that, for a given wavelength and technology, all tolerances can be relaxed by using wider access waveguides.

As an example, let us consider a 2×2 MMI coupler based on paired interference [64], comprising a multimode waveguide with $W_e \approx 16$ μm, $L = 425$ μm and $n_r \approx 3.30$, fed by access waveguides with $w_0 \approx 2.2$ μm, and operated at 1507-nm wavelength. Setting a loss penalty of $\mathcal{L} = 1.0$ dB, from Eqs. (2.44) and (2.45), we obtain $\delta L = 12.4$ μm; which substituted into Eq. (2.43) yields $\delta W_e = 0.23$ μm, and $\delta\lambda \approx 44$ nm. Thus, the multimode section width is by far the most critical parameter to control during fabrication. In a development stage, small variations in the width can be compensated for by varying lengths in steps of δL. In our example, five lengths L =415, 420, 425, 430, and 435 μm should be sufficient to obtain at least a pair of devices performing very close to design values. Experimental confirmation of these results will be presented in Chapter 3.

The dependence on polarization changes, which may be investigated through the factor $(n_r W_e^2)$ in Eq. (2.7), results in slightly different optimum imaging lengths for both polarizations. Polarization-independent operation is then possible by designing at an intermediate length, at the price of a small (shared) loss penalty. We calculated and measured polarization-change induced (full) penalty losses below 0.30 dB in 2×2 strip-loaded waveguide MMI couplers [99].

†The Rayleigh range is the distance from the beam waist at which the $1/e^2$ contour of a Gaussian beam has broadened $\sqrt{2}$ times.

Appendix 2A Paired interference

It will be verified here that, as suggested in [65], the single, two-fold, and multiple images found before also occur for MMI section lengths which are multiples of L_π instead of $3L_\pi$ provided that the modes 2, 5, 8,...are not excited. We start therefore by expressing the selective excitation using the *modulo* function

$$c_\nu = 0 \quad \text{for} \quad \text{mod}_3(\nu) = 2 \tag{2.46}$$

With this constraint, from Eq. (2.14), the field at a distance L can be explicitly written as

$$\begin{aligned} \Psi(y,L) \;=\; & \sum_{q=0}^{S} \Bigg\{ c_{3q}\, \psi_{3q}(y)\, \exp\left[j\,(3q+1)^2 \pi\, \frac{L}{3\,L_\pi} \right] \\ & + c_{3q+1}\, \psi_{3q+1}(y)\, \exp\left[j\,(3q+2)^2 \pi\, \frac{L}{3\,L_\pi} \right] \Bigg\} \end{aligned} \tag{2.47}$$

where the top summation limit is chosen as $S = \text{int}[(m-1)/3]$. The first term of the summation accounts for guided modes with $\nu = 3q$, and the second term accounts for guided modes with $\nu = 3q+1$, with $q = 0, 1, 2, \ldots$

This field will be calculated then for distances three times shorter than those given by Eq. (2.19) and Eq. (2.20). We shall distinguish the case of p even, and p odd.

Direct images

Starting with p even ($p = 2r$),

$$L = 2r\, L_\pi \quad \text{with } r = 0, 1, 2, \ldots \tag{2.48}$$

and substituting into Eq. (2.47) gives

$$\begin{aligned} \Psi(y,L) \;=\; & \sum_{q=0}^{S} \Bigg\{ c_{3q}\, \psi_{3q}(y) \exp\left[j\, \frac{(3q+1)^2}{3}\, 2r\, \pi \right] \\ & + c_{3q+1}\, \psi_{3q+1}(y) \exp\left[j\, \frac{(3q+2)^2}{3}\, 2r\, \pi \right] \Bigg\} \end{aligned} \tag{2.49}$$

Taking into account that, for all q

$$\begin{aligned} \text{mod}_3[(3q+1)^2] &= 1 \\ \text{mod}_3[(3q+2)^2] &= 1 \end{aligned} \tag{2.50}$$

and factorizing $\exp(j\ 2r\ \pi/3)$,

$$\Psi(y,L) = \exp\left(j\ 2r\ \frac{\pi}{3}\right) \sum_{q=0}^{S} \{c_{3q}\ \psi_{3q}(y) + c_{3q+1}\ \psi_{3q+1}(y)\} \tag{2.51}$$

Thus, apart from a phase factor, the field at $z = L_{2r}$ is a *direct* image of the field at $z = 0$.

Mirrored images

For p odd ($p = 2r + 1$)

$$L = (2r+1)\ L_\pi \quad \text{with } r = 0, 1, 2, \ldots \tag{2.52}$$

which substituted into Eq. (2.47) gives

$$\begin{aligned} \Psi(y,L) \;=\; & \sum_{q=0}^{S} \left\{ c_{3q}\ \psi_{3q}(y)\ \exp\left[j\ \frac{(3q+1)^2}{6}\ (2r+1)\ 2\pi \right] \right. \\ & \left. + c_{3q+1}\ \psi_{3q+1}(y)\ \exp\left[j\ \frac{(3q+2)^2}{6}\ (2r+1)\ 2\pi \right] \right\} \end{aligned} \tag{2.53}$$

Taking into account that,

$$\text{mod}_{\,6}[(3q+1)^2] = \begin{cases} 1 & \text{if } q \text{ even} \\ 4 & \text{if } q \text{ odd} \end{cases} \tag{2.54}$$

$$\text{mod}_{\,6}[(3q+2)^2] = \begin{cases} 4 & \text{if } q \text{ even} \\ 1 & \text{if } q \text{ odd} \end{cases} \tag{2.55}$$

the expression can be expanded in a sum of q even and q odd

$$\begin{aligned} \Psi(y,L) \;=\; & \sum_{q \text{ even}} \left\{ c_{3q}\ \psi_{3q}(y)\ \exp\left[j\ (2r+1)\ \frac{\pi}{3} \right] \right. \\ & \left. + c_{3q+1}\ \psi_{3q+1}(y)\ \exp\left[j\ (2r+1)\ \frac{4\pi}{3} \right] \right\} \\ & + \sum_{q \text{ odd}} \left\{ c_{3q}\ \psi_{3q}(y)\ \exp\left[j\ (2r+1)\ \frac{4\pi}{3} \right] \right. \\ & \left. + c_{3q+1}\ \psi_{3q+1}(y)\ \exp\left[j\ (2r+1)\ \frac{\pi}{3} \right] \right\} \end{aligned} \tag{2.56}$$

The subscript $3q$ corresponds to the even ν modes for q even and to the odd ν modes for q odd, whereas the subscript $3q + 1$ corresponds to the odd ν modes for q even and to the

even ν modes for q odd. Thus, the summation can be regrouped in symmetric (even) and antisymmetric (odd) guided modes

$$\begin{aligned}\Psi(y,L) &= \sum_{\nu \text{ even}} c_\nu \, \psi_\nu(y) \, \exp\left[j \, (2r+1) \, \frac{\pi}{3}\right] \\ &\quad + \sum_{\nu \text{ odd}} c_\nu \, \psi_\nu(y) \, \exp\left[j \, (2r+1) \, \frac{4\pi}{3}\right] \end{aligned} \tag{2.57}$$

and, after factorizing

$$\begin{aligned}\Psi(y,L) &= \exp\left[j \, (2r+1) \, \frac{\pi}{3}\right] \left\{ \sum_{\nu \text{ even}} c_\nu \, \psi_\nu(y) \right. \\ &\quad \left. + \sum_{\nu \text{ odd}} c_\nu \, \psi_\nu(y) \, \exp\left[j \, (2r+1) \, \pi\right] \right\} \end{aligned} \tag{2.58}$$

Dropping the common phase factor,

$$\Psi(y,L) = \sum_{\nu} (-1)^\nu \, c_\nu \, \psi_\nu(y) \tag{2.59}$$

The even modes are in phase and the odd modes in antiphase. Because of the symmetry property of the guided modes, the field at $z = L$ is a *mirror* image of the field at $z = 0$.

Two-fold images

For distances midway between the direct and mirrored images, i.e. at

$$L = \left(r + \frac{1}{2}\right) \, L_\pi \quad \text{with } r = 0, 1, 2, \ldots \tag{2.60}$$

Eq. (2.47) can be written as

$$\begin{aligned}\Psi(y,L) &= \sum_{q=0}^{S} \left\{ c_{3q} \, \psi_{3q}(y) \, \exp\left[j \, \frac{(3q+1)^2}{6} \, (2r+1) \, \pi\right] \right. \\ &\quad \left. + c_{3q+1} \, \psi_{3q+1}(y) \, \exp\left[j \, \frac{(3q+2)^2}{6} \, (2r+1) \, \pi\right] \right\} \end{aligned} \tag{2.61}$$

Again, taking into account Eq. (2.54) and Eq. (2.55), it can be developed into

$$\begin{aligned}\Psi(y,L) &= \sum_{q \text{ even}} \left\{ c_{3q}\, \psi_{3q}(y)\, \exp\left[j\,(2r+1)\,\frac{\pi}{6} \right] \right. \\ &\quad \left. + c_{3q+1}\, \psi_{3q+1}(y)\, \exp\left[j\,(2r+1)\,\frac{4\pi}{6} \right] \right\} \\ &\quad + \sum_{q \text{ odd}} \left\{ c_{3q}\, \psi_{3q}(y)\, \exp\left[j\,(2r+1)\,\frac{4\pi}{6} \right] \right. \\ &\quad \left. + c_{3q+1}\psi_{3q+1}(y)\, \exp\left[j\,(2r+1)\,\frac{\pi}{6} \right] \right\} \end{aligned} \tag{2.62}$$

With the same considerations as before, returning to the subscript ν

$$\begin{aligned}\Psi(y,L) &= \sum_{\nu \text{ even}} c_\nu\, \psi_\nu(y)\, \exp\left[j\,(2r+1)\,\frac{\pi}{6} \right] \\ &\quad + \sum_{\nu \text{ odd}} c_\nu\, \psi_\nu(y)\, \exp\left[j\,(2r+1)\,\frac{4\pi}{6} \right] \end{aligned} \tag{2.63}$$

and, after factorizing

$$\begin{aligned}\Psi(y,L) &= \exp\left[j\,(2r+1)\,\frac{\pi}{6} \right] \left\{ \sum_{\nu \text{ even}} c_\nu\, \psi_\nu(y) \right. \\ &\quad \left. + \sum_{\nu \text{ odd}} c_\nu\, \psi_\nu(y)\, \exp\left[j\,(2r+1)\,\frac{\pi}{2} \right] \right\} \end{aligned} \tag{2.64}$$

The common phase phactor just adds an overall phase, and can be dropped:

$$\Psi(y,L) = \sum_{\nu \text{ even}} c_\nu\, \psi_\nu(y) + \sum_{\nu \text{ odd}} j\,(-1)^{r+1}\, c_\nu\, \psi_\nu(y) \tag{2.65}$$

The field at $z = L$ is thus a linear combination of the even and odd modes with a relative phase of $\pm\pi/2$.

Appendix 2B Wavelength dependence

This Appendix details the calculation of the dependence of the beat length L_π on the wavelength. Derivating Eq. (2.7) with respect to λ

$$\frac{\partial L_\pi}{\partial \lambda} = \frac{4 n_r W_e^2}{3\lambda} \left[\frac{1}{n_r W_e^2} \frac{\partial (n_r W_e^2)}{\partial \lambda} - \frac{1}{\lambda} \right] \tag{2.66}$$

where

$$\frac{\partial (n_r W_e^2)}{\partial \lambda} = n_r \frac{\partial (W_e^2)}{\partial \lambda} + W_e^2 \frac{\partial n_r}{\partial \lambda} \tag{2.67}$$

In order to evaluate the derivative of W_e^2 with respect to λ, we can make the following assumption:

$$\frac{\partial (n_c / n_r)}{\partial \lambda} \approx 0 \tag{2.68}$$

which holds true for the waveguide structures used in this thesis.

Therefore, from Eq. (2.4)

$$\frac{\partial (W_e^2)}{\partial \lambda} = 2 W_e \frac{1}{\pi} \left(\frac{n_c}{n_r} \right)^{2\sigma} \frac{1}{\mathrm{NA}} \left(\mathrm{NA} - \lambda \frac{\partial \mathrm{NA}}{\partial \lambda} \right) \tag{2.69}$$

By writing

$$\mathrm{NA} = n_r \sqrt{1 - \left(\frac{n_c}{n_r} \right)^2} \tag{2.70}$$

and, taking into account Eq. (2.68), the derivative of NA results

$$\frac{\partial \mathrm{NA}}{\partial \lambda} = \frac{\mathrm{NA}}{n_r} \frac{\partial n_r}{\partial \lambda} \tag{2.71}$$

Defining n_g as the group refractive index:

$$n_g \doteq n_r - \lambda \frac{\partial n_r}{\partial \lambda} \tag{2.72}$$

and substituting Eq. (2.71) into Eq. (2.69), one obtains

$$\frac{\partial (W_e^2)}{\partial \lambda} = 2 W_e \frac{1}{\pi} \left(\frac{n_c}{n_r} \right)^{2\sigma} \frac{1}{\mathrm{NA}} \frac{n_g}{n_r} \tag{2.73}$$

which, by using Eq (2.4), can be written as

$$\frac{\partial (W_e^2)}{\partial \lambda} = \frac{2 W_e^2}{\lambda} \left(1 - \frac{W_M}{W_e} \right) \frac{n_g}{n_r} \tag{2.74}$$

With this result and the definition of group refractive index, Eq. (2.67) can be found to be

$$\frac{\partial(n_r W_e^2)}{\partial\lambda} = \frac{n_r W_e^2}{\lambda}\left[\frac{n_g}{n_r}\left(1 - \frac{W_M}{W_e}\right) + 1\right] \tag{2.75}$$

which, substituted into Eq. (2.66), allows us to calculate

$$\frac{\partial L_\pi}{\partial\lambda} = \frac{L_\pi}{\lambda}\left(2\frac{W_M}{W_e} - 1\right)\frac{n_g}{n_r} \tag{2.76}$$

Finally, expressing the differentials as small finite increments, the relative deviation of the beat length L_π due to a relative deviation in the wavelength becomes

$$\left.\frac{\delta L_\pi}{L_\pi}\right|_\lambda = \left(2\frac{W_M}{W_e} - 1\right)\frac{n_g}{n_r}\frac{\delta\lambda}{\lambda} \tag{2.77}$$

As an example, let us consider our InGaAsP/InP 16 μm-wide raised strip multimode waveguide [64] (described in Chapter 3). At 1.55-μm wavelength, the ridge TE (TM) effective index is $n_r = 3.30$ ($n_r = 3.29$) and the cladding effective index is $n_c = 3.27$ ($n_c = 3.25$). From Eq. (2.4), the TE (TM) effective width is 17.2 μm (16.9 μm). Using the Fiedler and Schlachetzki model [100] for the refractive index of quaternary ($\lambda_g = 1.30\,\mu$m) III-V compound lattice matched to InP, it is found $\partial n_r/\partial\lambda \approx -2.5 \times 10^{-4}\text{nm}^{-1}$. Thus, from Eq. (2.72), the group refractive index is $n_g \approx 3.69$. Substitution of these values into Eq. (2.77) yields

$$\left.\frac{\delta L_\pi}{L_\pi}\right|_\lambda = 0.96\,\frac{\delta\lambda}{\lambda} \approx \frac{\delta\lambda}{\lambda} \tag{2.78}$$

Appendix 2C Etch depth dependence

This Appendix details the calculations of the dependence of the beat length L_π on the etch depth. Derivating Eq. (2.7) with respect to the etch depth d yields

$$\frac{\partial L_\pi}{\partial d} = 2\frac{L_\pi}{W_e}\frac{\partial W_e}{\partial d} \tag{2.79}$$

The derivative of W_e with respect to the etch depth d is, from Eq. (2.4)

$$\frac{\partial W_e}{\partial d} = -\frac{\lambda}{\pi \mathrm{NA}^2}\frac{\partial \mathrm{NA}}{\partial d} \tag{2.80}$$

which was calculated for TE-polarization ($\sigma = 0$). A similar calculation can be performed for TM-polarization ($\sigma = 1$).

The dependence of the lateral numerical aperture NA on the etch depth d may be analytically calculated by derivating Eq. (2.70):

$$\frac{\partial \mathrm{NA}}{\partial d} = -\frac{2n_c}{\mathrm{NA}}\frac{\partial n_c}{\partial d} \tag{2.81}$$

and then investigating further the behaviour of n_c with respect to the etch depth d.

A numerical solution is also possible if the waveguide structure is known. Figure 2.12 shows the calculated lateral numerical apertures as a function of the etch depth for the waveguide structures used in this thesis: the silica-based (rib) waveguide and the InP-based strip-loaded

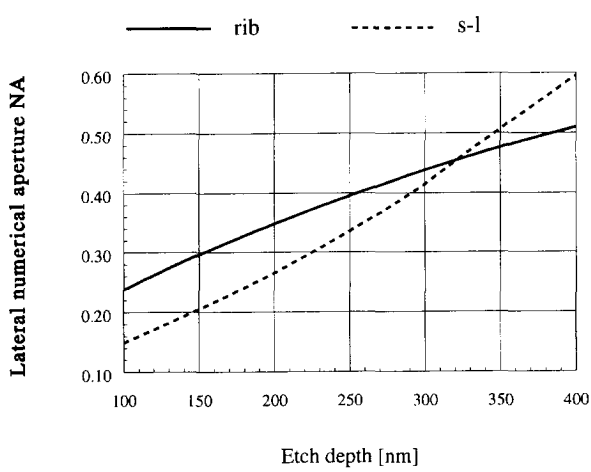

Figure 2.12 Lateral numerical aperture NA as a function of etch depth, calculated for the silica-based (rib) waveguide of Fig. 3.1 and for the InP-based strip-loaded (s-l) waveguide of Fig. 3.2, at 1.55-μm wavelength.

(s-l) waveguide, described in Chapter 3. From these curves, the derivative of NA with respect to the etch depth, at an etch depth of $d = 300$ nm for the silica-based waveguide is:

$$\frac{\partial \mathrm{NA}}{\partial d} \approx 0.8\ \mu\mathrm{m}^{-1} \tag{2.82}$$

and, for the InP-based waveguide is:

$$\frac{\partial \mathrm{NA}}{\partial d} \approx 1.8\ \mu\mathrm{m}^{-1} \tag{2.83}$$

Substituting Eq. (2.80) into Eq. (2.79), and expressing the differentials as small finite increments, gives

$$\frac{\delta L_\pi}{L_\pi} = \frac{-2\lambda}{\pi W_\mathrm{e} \mathrm{NA}^2} \left(\frac{\partial \mathrm{NA}}{\partial d} \right) \delta d \tag{2.84}$$

With the value given by Eqs. (2.82) and (2.83), and for $\lambda = 1.55\ \mu$m and $W_\mathrm{e} \approx 15\ \mu$m, it follows that a 10% change on a 300-nm etch depth produces a change of less than 2.5% in the beat length L_π. The dependence of the beat length on the etch depth is therefore very weak indeed.

Chapter 3

Multimode interference devices

This chapter presents the design considerations, numerical simulations and measurement results of basic passive multimode interference couplers and splitter/combiners. A short description is given of the silica-based aluminum oxide waveguides and indium phosphide-based waveguides structures. The restricted-interference imaging effect is applied in the realization of 2×2 3-dB and cross-couplers. A numerical and experimental assessment of fabrication and operation tolerances for the 3-dB MMI couplers is performed, confirming the theoretical predictions made in Chapter 2. The chapter closes with a simple symmetric interference concept used to produce ultra-short 1×2 power splitters. These experiments were reported at IPR '91, Monterey, 1991, [57]; J. Lightwave Tech., 1992, [59]; ECOC '92, Berlin, 1992 [60]; *and* ECIO '93, Neuchâtel, 1993 [99].

3.1 Waveguide structures

This section describes briefly the dielectric and semiconductor waveguide structures used for the fabrication of the integrated optical couplers presented in this thesis. The emphasis is laid upon the design specifications and fabrication constraints regarding the desired components and the available technology. The fabrication technology of silica-based aluminum oxide waveguides was developed at the Delft University of Technology for the realization of passive planar optical devices, described by M. K. Smit [66]. The expertise gained in this area was later transferred to indium phosphide-based waveguides, aiming at the fabrication of integrated circuits including passive optical devices as well as photodetectors [67] and, in future, field-effect transistors.

3.1.1 Silica-based waveguide

Figure 3.1 shows a cross-section of the silica-based aluminum oxide waveguide. It is composed of a rib-shaped Al_2O_3 guiding film sandwiched between two SiO_2 cladding layers.

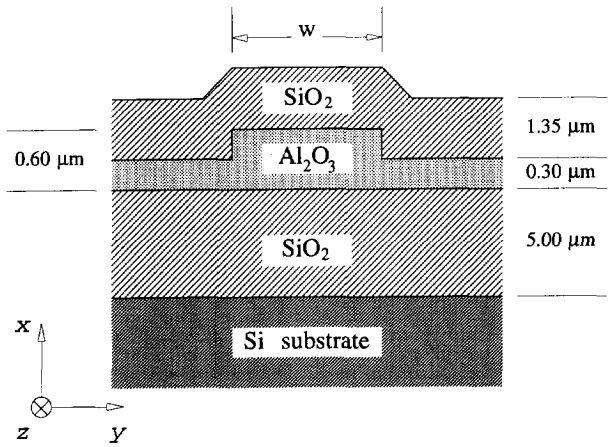

Figure 3.1 Cross-section view of the silica-based aluminum oxide waveguide structure. At 1.55-μm wavelength, the refractive indices are: n(Al_2O_3)=1.673 and n(SiO_2)=1.444.

Transverse (x-axis) optical confinement is provided by the Al_2O_3/SiO_2 refractive index difference, whereas lateral (y-axis) optical confinement is achieved through the effective refractive index contrast created by the ridge.

The waveguides are fabricated on a silicon substrate, which not only constitutes the mechanical support but also supplies the Si atoms for the growth of an SiO_2 buffer layer by thermal oxidation. This buffer layer provides downward optical confinement and, because of its thickness (~5 μm), it prevents the guided light from leaking into the high-index ($n \approx 3$) silicon substrate. The 0.6-μm Al_2O_3 guiding layer is sputtered by an RF (radio frequency) diode sputtering process [101]. The ridge is first masked by photoresist and then etched with a beam of (1 keV) accelerated Ar atoms. A 1.35 μm-thick SiO_2 cover layer is then RF magnetron sputtered onto the patterned guiding layer. Finally, a 60-minute 825°C thermal annealing step results in optical attenuations of 0.3 dB/cm at 1.55-μm wavelength [102].

The guiding film thicknesses were standardized [66] such that, for different wavelengths, the transverse V-parameter be $V \approx 2$. For example, for a wavelength of 1.55 μm, the guiding film thickness was chosen as 600 nm. This allows a lateral contrast up to 25% of the transverse contrast to be obtained by etching away half of the guiding film.

The fabrication of waveguides narrower than 2 μm presents poor width reproducibility. This is mainly due to contrast limitations in the pattern projection and developing during the photolithographic process, and (photoresist) mask degradation during the Ar-atom beam milling. Therefore, a standard access waveguide width of 2 μm was adopted.

The silica-based waveguide technology provides a simple and highly reproducible means to fabricate passive integrated optics. Moreover, this structure allows a prism-coupling technique

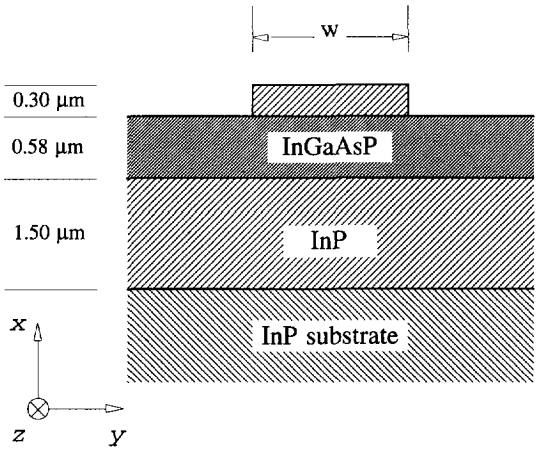

Figure 3.2 Cross-section view of the InP-based waveguide structure. The guiding film is a lattice-matched InGaAsP layer with a wavelength absorption edge $\lambda_g = 1.3$ μm. At 1.55 μm-wavelength, the refractive indices are n(InGaAsP)≈3.39 and n(InP)≈3.17.

which, because of its mode selectivity [103], proves very valuable during the characterization of the devices. Another advantage often mentioned is the fact that its wavelength in the material at 0.6328-μm is very nearly equal to the wavelength in InGaAsP at 1.30 or 1.55-μm, and its refractive index contrasts are similar, which would allow for passive compound semiconductor devices at near infrared to be 'prototyped' by silica-based aluminum oxide devices operating at visible light.

3.1.2 InP-based waveguide

Figure 3.2 shows the cross-section of the InP-based strip-loaded film waveguide [104]. It is composed of an $In_{0.72}Ga_{0.28}As_{0.61}P_{0.39}$ (band-edge absorption wavelength $\lambda_g = 1.3$ μm) guiding layer sandwiched between two InP layers. The 1.5-μm InP buffer layer prevents the beam tails from propagating in the wafer substrate, where dopants and/or impurities could attenuate the signal.

The layer stack is grown on a two-inch InP wafer by low-pressure metal-organic vapour phase epitaxy (MOVPE) [105], a technique which produces III-V semiconductor waveguides with lower attenuation than those produced by liquid-phase epitaxy (LPE), because of its smoother epilayer surfaces and the absence of absorbing defects at the interfaces [106].

After cleaning the surface, a 140 nm-thick SiO_2 layer is sputtered over the entire wafer. The wafer is diced in slices of about 1 cm^2. (In a large-scale production, the whole wafer would go ahead for further processing). A 430-nm thick AZ-5206 photo-resist (PR) is then

applied to the slice by 8000-rpm spinning, and dried in a 90–100°C post-spin bake to harden it by removing the remaining solvents.

The choice of SiO_2 layer thickness (one half-wave) aims at minimizing the reflectivity at the PR-SiO_2 interface, which determines the magnitude of the standing wave ratio within the PR during exposure. The development rate and edge profiles are most uniform with a minimum in the standing wave ratio [107, 108].

A quarter-wave (or odd multiple) thickness of resist on a half-wave of SiO_2 can reduce the reflectivity at the air-PR interface from a maximum of 40% to less than 10% [107], and therefore minimize the amount of scattered light and possible back-reflections from the projection system onto the sample.

The circuit layout is transfered from a dark-field chromium mask onto the photoresist-coated slice by a 4:1-reduction g- (436 nm) and h-line (405 nm) Canon pattern projection aligner (typically 70–150 mJ/cm^2). The resist is then image-reversal baked (1–4 min at $\sim$100°C), flood-exposed (30–40 mJ/cm^2) and developed. The image-reversal process offers good advantages compared with standard positive tone photolithography, because vertical walls can be easily achieved and standing wave effects are reduced to a minimum [109, 110].

The SiO_2 layer is patterned by reactive-ion etching in a CHF_3 plasma. After O_2 stripping the photoresist, the waveguides are etched by a sequence of CH_4/He RIE and O_2 descumming steps. The descumming steps remove the polymer deposited on the ridge during the preceding etch steps, thus minimizing the striations due to non-uniform polymer masking [111, 112].

The process is completed by removing the SiO_2 in an HF bath, and the oxides in acid baths. The slices are then scribed and cleaved; and the samples can be anti-reflection coated by depositing a quarter-wave layer of SiO_x ($n \approx 1.80$ @ 1.55-μm) on the cleaved facets.

Unlike the silica-based bottom-up technology described before, the fabricaton of the InP-based waveguide follows a top-down approach, where the complete layer stack is grown first and shaped afterwards by material removal. This strategy has the advantage of needing just one epitaxial growth step on a perfectly planar substrate, the avoidance of regrowth steps being of primary importance when monolithically integrating waveguides with other devices [113, 67].

Compound semiconductors of the groups III and V offer important advantages when compared with other materials* such as glass or $LiNbO_3$ for optical waveguide fabrication [115]:

1. The potential for monolithically integrate (passive) low-loss guided-wave devices [106] with (active) optoelectronic [113] and electronic components [116]. This stems from the fact that, when InP is used as a substrate, lattice-matched InGaAsP alloys with varying refractive indices can be prepared whose bandgaps span the range 0.92–1.65 μm, covering the fibre-optic communication wavelengths [117].

2. The possibility of high-speed refractive index modulation by field-induced effects (linear –Pockels– and quadratic –Kerr– electro-optic) [118], by carrier-induced effects (plasma

*Theoretical studies seem to indicate that InGaAsP/InP phase modulators can also outperform GaAs/AlGaAs structures in terms of modulation efficiency [114].

and band-filling) [119, 120], or by a combination of them (depletion edge translation, — called the Franz-Keldysh effect in bulk material or Stark shift in quantum-well structures) [121].

3. The availability of versatile (though still not cheap) fabrication processes (e.g., epitaxial growth, selective etching, anisotropic etching) for complex structural shaping and simple techniques for end-facet preparation (i.e., scribe-and-cleave versus cut-and-polish).

3.2 Waveguide analysis

For the analysis of the silica-based rib waveguides (Fig. 3.1) and the InP-based strip-loaded waveguide (Fig. 3.2), we used the effective index method (EIM), originally proposed by Knox and Toulios for dielectric sub-millimiter waveguides [77]. The EIM transforms a three-dimensional problem into a two-dimensional effective waveguide. The original waveguide cross-section is first divided into a number of laterally invariant regions, where the effective indices are calculated considering these regions to be infinitely extended in the lateral direction. Then each region is taken as a film with thickness equal to its original width and refractive index equal to its calculated effective index. The waveguide thus formed is sometimes referred to as "equivalent slab waveguide", a two-dimensional structure which can be solved analytically [122].

The EIM has proved satisfactory in providing accurate propagation constants with simple and fast calculations for the waveguide structures used in this thesis. Published numerical examples proved its reliability on a number of other structures as well [123].

The refractive indices of the silica-based waveguides were taken from [66], and those of the InGaAsP lattice-matched to InP were calculated using the Fiedler and Schlachetzki's model [100] based on an interpolation from InGaP and InGaAs ternary systems [124].

Figure 3.3 and 3.4 show examples of mode effective indices in 14-μm and 16 μm-wide multimode silica- and InP-based waveguides respectively, calculated with EIM and a scalar Finite Element Method (FEM). It can be seen that, for the lower order modes, EIM predictions are well within 10^{-3} with respect to those of the FEM.

3.3 silica-based 2×2 MMI couplers

This section presents the modelling and experimental work on silica-based 2×2 MMI couplers, as has appeared in several publications. The results of the first activities on 2×2 MMI couplers were presented at the Integrated Photonics Research Topical Meeting (IPR'91) on April 9-11, 1991, Monterey, USA [57, 58]; and prompted an increasing activity in multimode interference devices (see references in this chapter). The modelling and characterization of restricted interference MMI 3-dB and cross-couplers were reported in a regular paper at the *17th European*

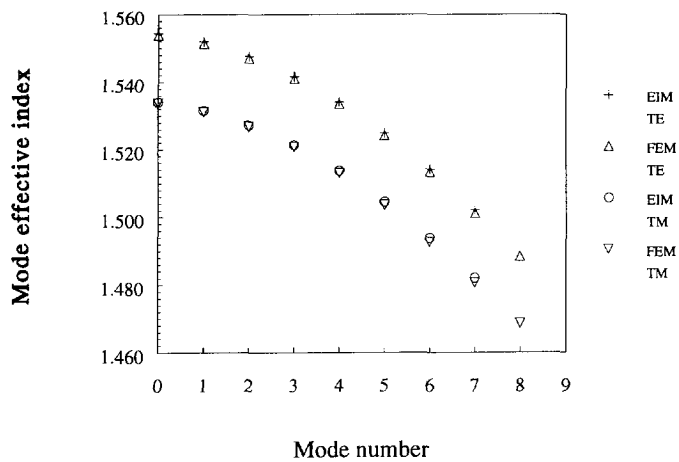

Figure 3.3 Comparison between the EIM and FEM predictions of the mode-effective indices for a 14 μm-wide silica-based aluminum oxide waveguide structure.

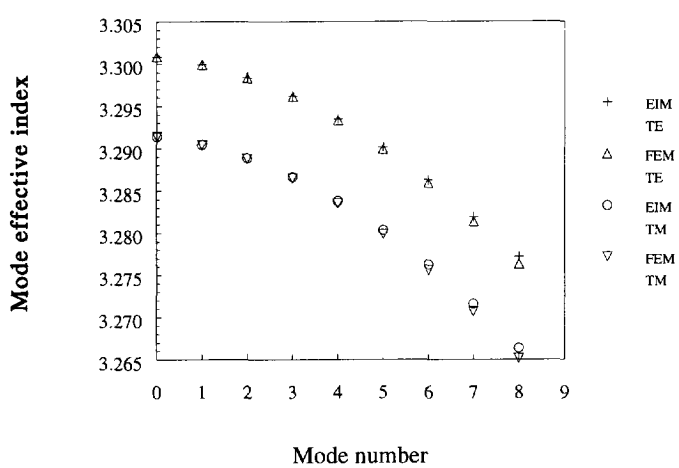

Figure 3.4 Comparison between the EIM and FEM predictions of the mode-effective indices for a 16 μm-wide InP-based waveguide structure.

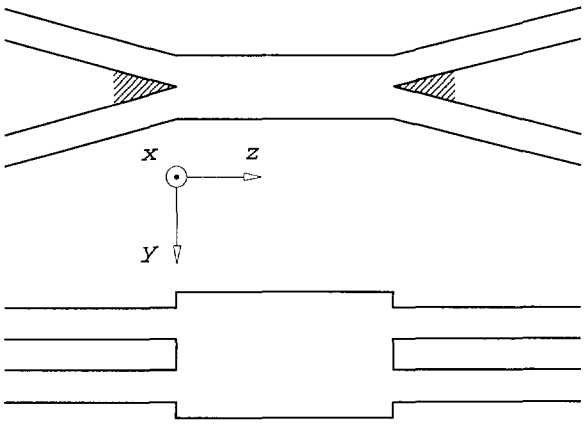

Figure 3.5 Top: Classical two-mode interference (TMI) coupler showing the blunted areas. Bottom: Multimode interference (MMI) coupler.

Conference on Optical Communication ECOC'91, on September 9-12, 1991, Paris, France [89], and published in more detail in the *Journal of Lightwave Technology* [59].

3.3.1 Introduction

Optical couplers are key components in photonic integrated circuits both for signal routing and signal processing. Two-Mode Interference (TMI) couplers had already been proposed in 1977 [125] as a more tolerant alternative to the weak synchronous couplers based on parallel waveguides, and reported in 1988 [126] to build integrated-optic dual-channel wavelength-division (de)multiplexers. TMI couplers consist of a two-moded central waveguide (TMI section) connected to two pairs of single-moded access waveguides, as shown at the top of Fig. 3.5.

Compared to weak synchronous couplers, TMI couplers are shorter, less sensitive to fabrication variations and less polarization dependent. However, requirements of high power coupling efficiency and proper mode excitation from the single-moded access waveguides to the TMI section limit the branching angle of the access waveguides to very small values (typically $< 2\,^{\circ}$ [127]). Due to the finite resolution of the lithographic process, part of the area between the access waveguides (shaded regions in Fig. 3.5) will become blunted in a non-reproducible way. This introduces considerable variation in the actual length of the TMI section, causing spread in coupler performance. Moreover, due to the proximity of the access waveguides, extra modal coupling occurs [128], adding to the performance spread.

Replacing the TMI section by a (wider) multimode interference (MMI) section while

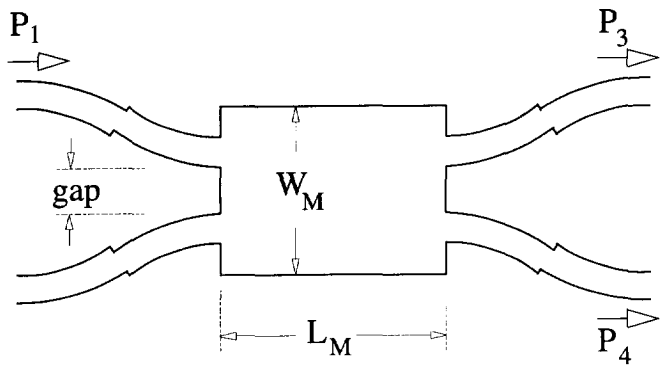

Figure 3.6 Schematic geometry of the multimode interference coupler, with dimensions and definitions.

keeping the access waveguides single-moded (as shown in Fig. 3.5, bottom) allows a good separation of the access waveguides at the junctions, eliminating the performance spread due to both the blunting and the extra coupling in the access waveguides. Further, because of the high number of modes supported by the multimode section, power coupling efficiencies are higher and consequently device excess losses are lower than those of TMI couplers (which are typically 1-3 dB [127]).

3.3.2 Design and modelling

Figure 3.6 shows the geometry of our MMI couplers, based on the paired interference structure shown in Fig. 2.6. Curved access waveguides ensure a fast separation and single-mode excitation field at the entrance of the multimode section.

The modal excitation coefficients at the entrance of the multimode section are calculated with the overlap integral Eq. (2.10). Fig. 3.7 shows the calculated field profiles corresponding to the modes 2, 5, and 8 of the silica-based 14 μm-wide multimode waveguide. Figure 3.8 shows the squares of the overlap integrals between a fundamental mode input profile and all the guided modes in the multimode section as a function of the offset, i.e., the lateral distance between the centre of the multimode section and the outer ridge of the curved access waveguide. Note that, although the fundamental mode profile in the curve is not perfectly symmetric, its asymmetry is low enough not to excite appreciably the undesired modes 2, 5, and 8.

Figure 3.8 allows the choice of the optimum gap (as defined in Fig. 3.6) to best satisfy the selective excitation of Eq. (2.46). In our case, a 1.65-μm offset (gap = 3.30 μm) was adopted,

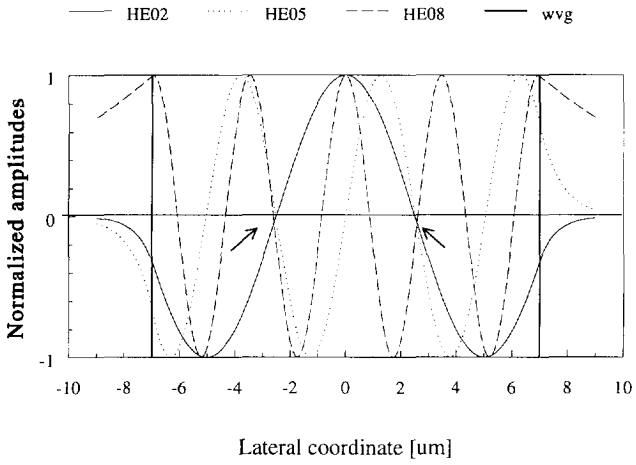

Figure 3.7 The amplitude-normalized lateral field profiles of the 2nd, 5th, and 8th order modes in the 14 μm-wide multimode section. All these modes present a zero and odd symmetry at the same lateral positions ($y \approx \pm 2.6$ μm, marked by arrows).

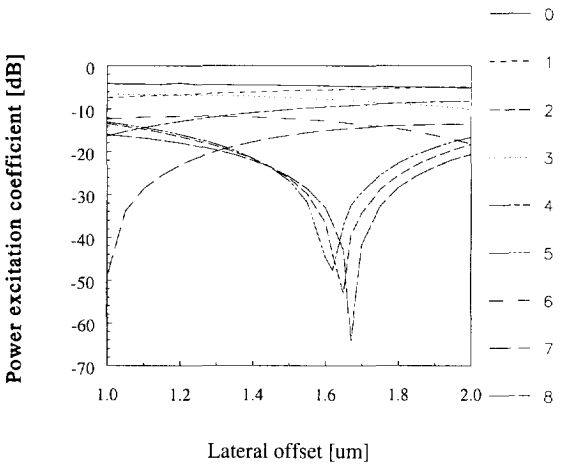

Figure 3.8 Squares of the overlap integral calculated between the fundamental mode of the access waveguides and all guided modes in the multimode section, as a function of the offset.

which results in $c_2^2 = -53$ dB, $c_5^2 = -37$ dB, $c_8^2 = -43$ dB.

With these data, a mode-propagation calculation as outlined in Section 2.3 is carried out to obtain the total field at any z-position in the multimode section. Finally, an overlap integral between the field at the end of the multimode section and the field in the single-moded output waveguides allows the prediction of the optical power in each output branch. Coupling between the access waveguides was calculated to be very low, because of the rather large gap and sharp bends, and it is therefore neglected.

In order to assess the performance of 2×2 MMI couplers we define the following figures of merit. For the 3-dB couplers:

$$\text{Excess Loss} = 10\log\left(\frac{P_3 + P_4}{P_1}\right) \tag{3.1}$$

$$\text{Imbalance} = 10\log\left(\frac{P_3}{P_4}\right) \tag{3.2}$$

And for the cross couplers:

$$\text{Insertion Loss} = 10\log\left(\frac{P_4}{P_1}\right) \tag{3.3}$$

$$\text{Crosstalk} = 10\log\left(\frac{P_3}{P_4}\right) \tag{3.4}$$

A perfect 3-dB coupler should have 0-dB Excess Loss and 0-dB Imbalance. A perfect cross-coupler should have 0-dB Insertion Loss and infinitely low Crosstalk.

With the procedure just described, sensitivity analysis can be performed of the behaviour of the couplers to some fabrication parameters (e.g., the MMI section width, the MMI section length, etc.) or operation parameters (e.g., the wavelength λ and the state of polarization). Figure 3.9 shows the calculated sensitivity of the 3-dB couplers to variations in the width of the multimode section. It can be seen that in order to ensure that excess losses are below 1 dB and imbalances are better than 0.1 dB, the width of the multimode section must be kept within ± 0.40 μm from its optimum design value. Figure 3.10 shows the calculated sensitivity of the 3-dB couplers to variations in the wavelength. For a wavelength range between 1520 and 1590 nm the excess loss is expected to be better than 0.5 dB and the imbalance to remain within ± 0.1dB.

3.3.3 Fabrication

Two sets of devices (3-dB and cross-couplers) were designed and fabricated for operation at 1520-nm wavelength. The set of 3-dB couplers have $W_M = 14.0$ μm (supporting a total of 9 modes). The simulated optimum length for the multimode section is $L_M = 155$ μm and the couplers were fabricated with L_M ranging from 120 to 190 μm in steps of 5 μm. The set of cross couplers have $W_M = 12.0$ μm (supporting a total of 7 modes). The predicted

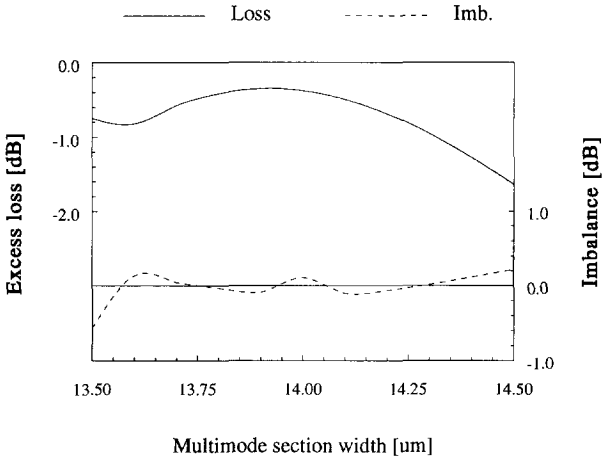

Figure 3.9 Calculated sensitivity of the excess loss (solid line) and imbalance (dashed line) to the multimode section width for the silica-based 3-dB couplers at 1520-nm wavelength.

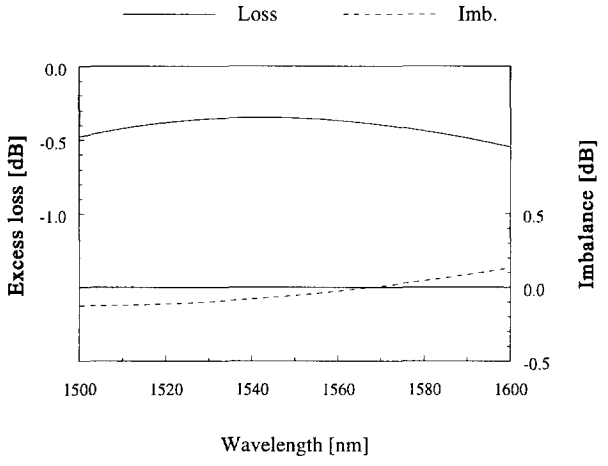

Figure 3.10 Calculated sensitivity of the excess loss (solid line) and imbalance (dashed line) to the free-space wavelength for the silica-based 3-dB couplers with W_M=14.0μm.

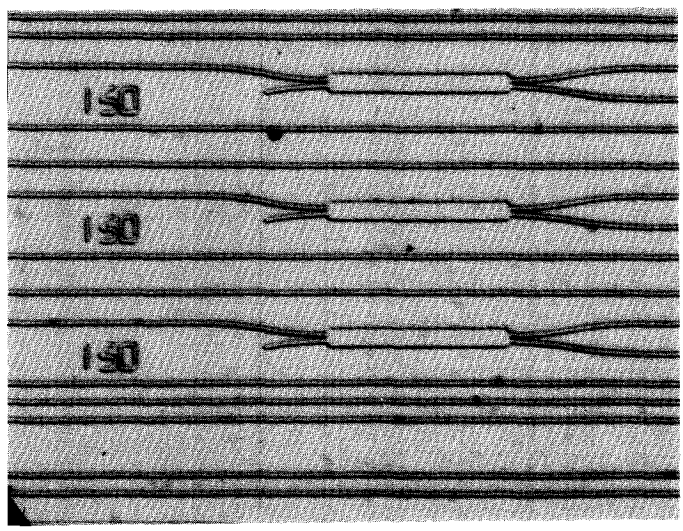

Figure 3.11 Nomarsky micrograph of the silica-based MMI 3-dB couplers. The identification numbers on the left indicate the multimode section length in micrometres. Straight reference waveguides can be seen running alongside the couplers.

optimum length for the multimode section is $L_M = 236$ μm and the couplers were fabricated with L_M ranging from 200 to 270 μm in steps of 5 μm. Figure 3.11 shows a microscope photograph of the realized couplers. Straight access waveguides are 2 μm-wide, and curved access waveguides have 300-μm radii, a width of 2 μm, are strictly single-moded and provide a lateral access waveguide separation of 30 μm. Straight reference waveguides are included running alongside each device, which allow monitoring of the input-launched optical intensity.

3.3.4 Experimental results

Measurements were carried out by coupling a 1.52-μm wavelength Fabry-Perot laser beam by means of a prism-coupling technique [103] to one of the input access waveguides (P_1 in Fig. 3.6) and recording the light intensities at both output access waveguides (P_3 and P_4) from the polished end-face. Each coupler was repeated three times in the layout and each layout was repeated three times in the silicon wafer in order to test on-chip and on-wafer repeatability.

Experimental data is shown in Figs. 3.12, 3.13 and 3.14, where the lines represent computer-simulated predictions and the markers are measured values, obtained as an average from 9 nominally identical devices.

Figure 3.12 presents the results for the 3-dB couplers. The measured imbalance for the

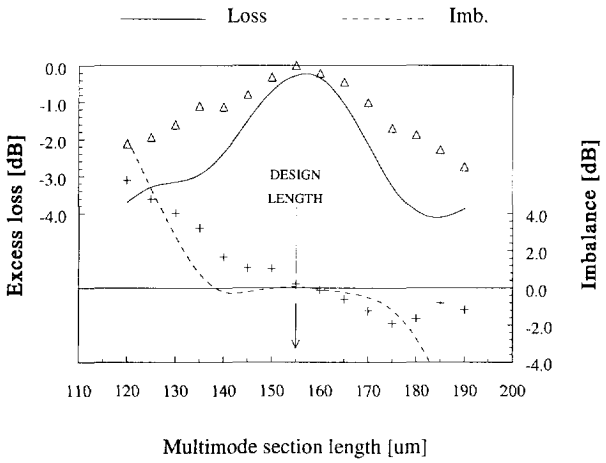

Figure 3.12 Excess loss and imbalance results for the 3-dB couplers. Solid line is simulated and triangles are measured excess losses. Dashed line is simulated and crosses are measured imbalances.

couplers with optimum multimode section length is below 0.2 dB and simultaneously the excess loss reaches a minimum (measured to be around 0.2 dB).

Figure 3.13 and Fig. 3.14 present the results for the cross-couplers. The measured insertion loss for the optimum multimode section length is 0.8 dB and the measured crosstalk is −18 dB, reaching 0.5-dB insertion loss and the same crosstalk figure for a slightly larger multimode section length.

The design of the couplers was optimized for TE-polarization. When tested for TM-polarization they showed an average of 0.2 dB extra excess/insertion loss, no appreciable deterioration in the imbalance and a slight improvement (~1 dB)in the crosstalk.

Measurements agree quite well with computer simulations in the region around the optimum multimode section length. The discrepancy in the adjacent regions can be attributed to a lower number of modes being guided in the multimode section, due to an obtained etch depth somewhat smaller than the one depicted in Fig. 3.1, and smooth, tilted waveguide sidewalls. Simulations with slightly wider access waveguides (dotted line in Fig. 3.13) seem to confirm the tendency towards a flatter and lower characteristic.

3.3.5 Conclusions

The self-imaging property of a homogeneous multimode step-index optical waveguide has been applied in the design of passive planar monomode optical couplers working by multimode interference. Based on these designs, 3-dB and cross-couplers were fabricated in Al_2O_3/SiO_2

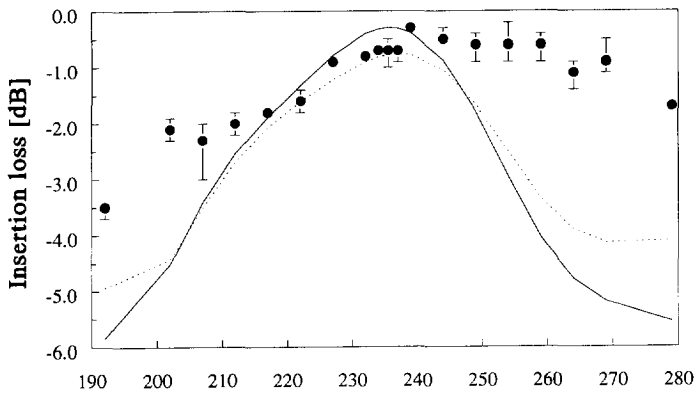

Figure 3.13 Insertion loss results for the cross-couplers. Solid line is simulated and dots are measured insertion losses. The dotted line shows the calculated insertion loss for a device supporting only 5 modes.

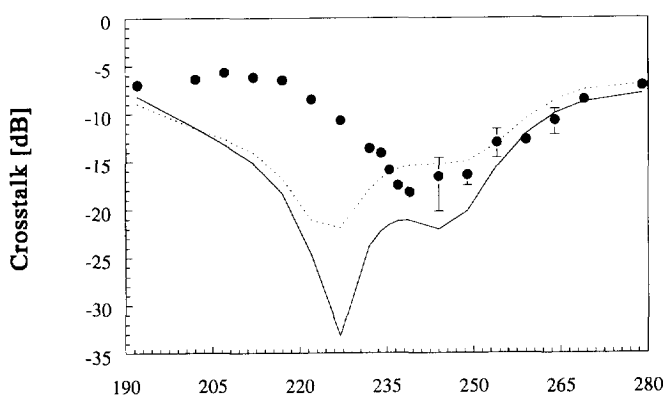

Figure 3.14 Crosstalk results for the cross couplers. Solid line is calculated and dots are measured insertion losses. The dotted line shows the calculated crosstalk for a device supporting only 5 modes.

channel waveguides on Si substrates. Theoretical predictions and experimental results at 1.52-μm wavelength were presented which demonstrate that MMI couplers offer high performance: on-chip excess loss better than 0.5 dB, imbalance within 0.2 dB for the 3-dB couplers, crosstalk below 15 dB for the cross-couplers, high reproducibility, low polarization dependence and small device size.

Experimental agreement with computer-simulated behaviour is good around the design values. All measured quantities show rather flat curves with respect to the multimode section length, providing an indication of the good tolerance to this process parameter. The most critical parameter in the fabrication of the couplers is the multimode section width which, according to the calculations so far, should be controlled to ± 0.40 μm from its design value in order to achieve acceptable excess loss and imbalance figures. This was experimentally verified and is presented later in this chapter.

Because of its good tolerance to process and operation parameters, this new coupler is suitable for integration with more complex OEICs such as phase diversity networks (see Chapter 4), Mach-Zehnder interferometers (see Chapter 5), integrated balanced receivers [129], and electro-optic waveguide switches [82, 130].

3.4 InP-based 2×2 MMI couplers

This section presents the modelling and experimental results obtained on two sets of InP-based 3-dB MMI couplers, with emphasis on the coupler's tolerance to fabrication and its behaviour under varying conditions of operation.

The study on the multimode section length and width was performed on 3-dB MMI couplers designed and fabricated for a Mach-Zehnder interferometer polarization splitter [64] (dealt with in Chapter 5).

The study on the multimode section width and optical bandwidth is a result of cooperation between the Institute for Quantum Electronics at the Swiss Federal Institute of Technology and our laboratory at Delft University of Technology [99]. These devices were designed in Delft and fabricated in Zurich as part of a low-voltage polarization-insensitive Mach-Zehnder interferometer switch in InGaAsP/InP [130].

For both sets, measurements were carried out at TE and TM polarizations, at the 1.55 μm-wavelength window.

3.4.1 Introduction

Tolerance to fabrication parameters is an important issue for any device, all the more when it is integrated along with other devices, and occupies a relatively large chip area. Recent papers demonstrated the integrateability of MMI couplers in a polarization-insensitive Mach-Zehnder interferometer electro-optic switch [83], and in a monolithic polarization diversity balanced receiver [131].

With the coming of the ~25 nm-bandwidth erbium-doped fibre amplifier into the WDM communication systems, integrated optical couplers and splitters are required to have bandwidths at least that large. In spite of its relevance, we found only a few articles [132, 133] addressing the subject of wavelength sensitivity of (cross) directional couplers. Here we present the calculated and the measured sensitivity to fabrication process parameters, state of polarization and operating wavelength in the range of 1440–1570 nm for InGaAsP/InP 3-dB MMI couplers.

3.4.2 Modelling

The InGaAsP/InP waveguide structures were analysed with the Effective Index Method (EIM). The couplers were modeled by two methods: Two-dimensional finite difference Beam Propagation Method (BPM) [134] and Mode Propagation Analysis (MPA). The MPA was carried out by computing the excitation coefficients of each guided mode in the multimode section with a one-dimensional overlap integral at $z = 0$, propagating them, reconstructing the total field and computing the excitation coefficients to both output waveguides with a one-dimensional overlap integral at $z = L_M$.

As BPM takes all modes into account (including radiative modes), it provides an accurate model for most optical devices but, being a purely numerical method, makes the understanding of the devices difficult. The MPA, however, takes into account only guided modes and therefore gives good results only for well-guiding structures in which most of the power is carried by the guided modes, but has the advantage of providing a modal description inside the multimode section and thus some insight into the device operation. We show that MPA is in good agreement with BPM and experimental results.

3.4.3 Electro-optic switch compatible structure

The cross-section of the strip-loaded waveguide structure (compatible with an electro-optic phase shifter which has been integrated in a Mach-Zehnder interferometer switch [130]) is shown in Fig. 3.15. A thick InP top layer and weakly doped layers adjacent to the InGaAsP guiding layer keep the absorption losses low. The layers were grown by Metal-Organic Vapour Phase Epitaxy (MOVPE) on an n^+-InP substrate. The waveguides were patterned by magnetron-enhanced CH_4/H_2 reactive ion etching.

3.4.4 Fabrication

The general layout of the couplers is depicted in Fig. 3.6. Lateral offsets were applied at curve-to-straight and curve-to-curve junctions in order to minimize transition losses.

The 3-dB MMI couplers for the passive polarization splitter were fabricated in the structure shown in Fig. 3.2. In order to prove experimentally the theoretical predictions on geometrical

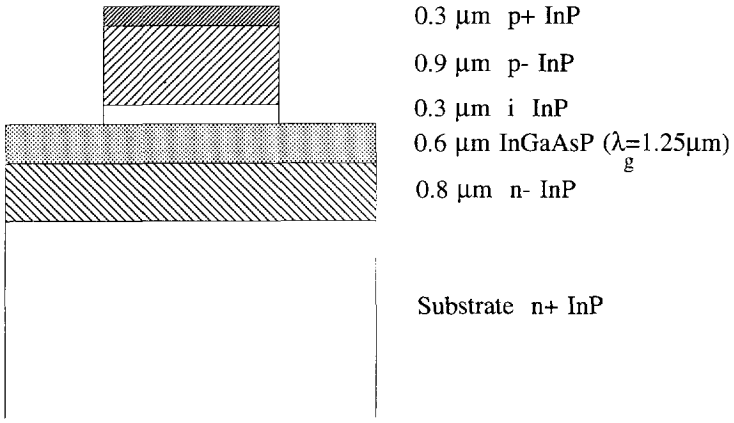

Figure 3.15 Cross-section view of the InGaAsP/InP strip-loaded waveguide structure grown by MOVPE, compatible with an electro-optic phase shifter.

tolerances obtained in Section 2.8, their lengths L_M and widths W_M span the ranges 415–435 μm and 15.6–16.4 μm in five steps each. Curved access waveguides are 2 μm-wide and have a radius of 1.3 mm.

The structure shown in Fig. 3.15 was used for the realization of the 3-dB MMI couplers for the electro-optic switch, with $L_M = 530$ μm and W_M ranging from 17.5 to 18.5 μm in steps of 0.25 μm. The curved access waveguides have a radius of 2 mm and are 3-μm wide.

3.4.5 Experimental results

The devices were measured by launching light alternatively into each input and recording the light from both outputs. End-fire coupling was accomplished with a pair of 40× IR anti-reflection coated microscope objectives and the output was imaged onto a Ge photodiode and a video camera.

We measured excess loss relative to the best (lowest attenuation) straight waveguide, and imbalance as a function of the multimode section length and width, and as a function of wavelength, for both polarizations.

Figure 3.16 and Fig. 3.17 show the excess losses and imbalances for TE and TM polarization measured at 1520 nm for 25 different couplers as a function of W_M, with L_M as a parameter. These couplers were realized in the structure given in Fig. 3.2 and showed a best excess loss of 0.3 dB and imbalances within 0.2 dB.

Figure 3.18 and Fig. 3.19 show simulation and measurement results for TE and TM polarization obtained at 1530 nm for the series of couplers with $L_M = 530$ μm and varying multimode section width, realized in the structure of Fig. 3.15. Figure 3.20 and Fig. 3.21

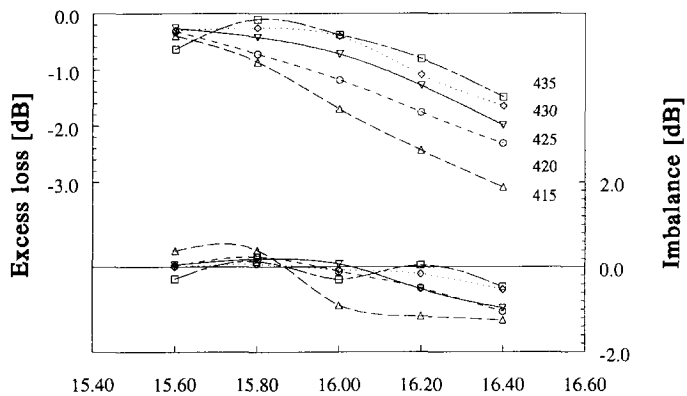

Figure 3.16 Excess loss and imbalance of InP-based 3-dB MMI couplers for TE polarization, as a function of W_M, with $L_M = 415 \ldots 435$ μm as a parameter. Markers are measured values and lines are spline fits.

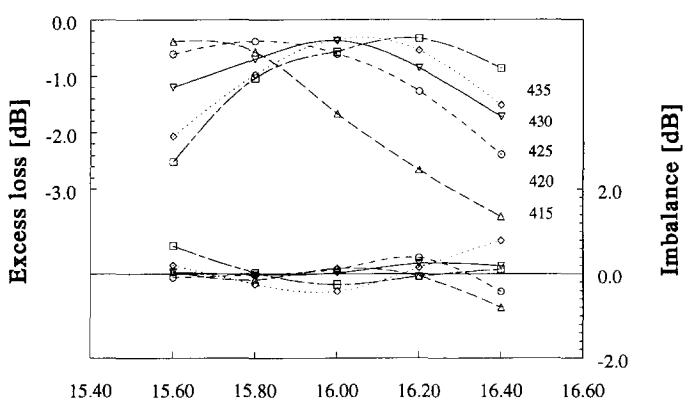

Figure 3.17 Excess loss and imbalance of InP-based 3-dB MMI couplers for TM polarization, as a function of W_M, with $L_M = 415 \ldots 435$ μm as a parameter. Markers are measured values and lines are spline fits.

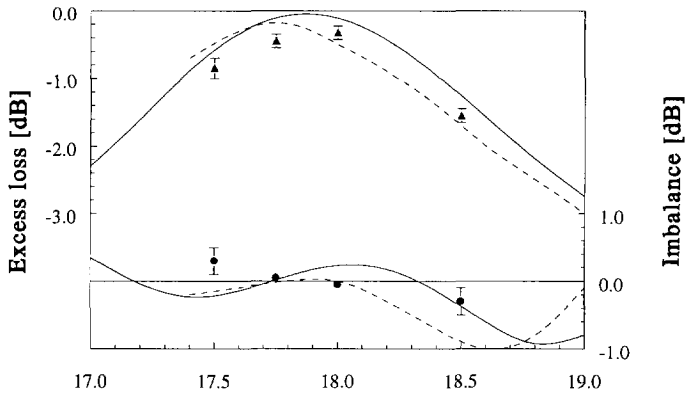

Figure 3.18 Tolerance to multimode section width at 1530 nm, TE polarization. Upper curves: calculated excess loss. Lower curves: calculated imbalance. Solid lines: MPA calculations. Dashed lines: BPM simulations. Markers: measured values. Bars: observed spread.

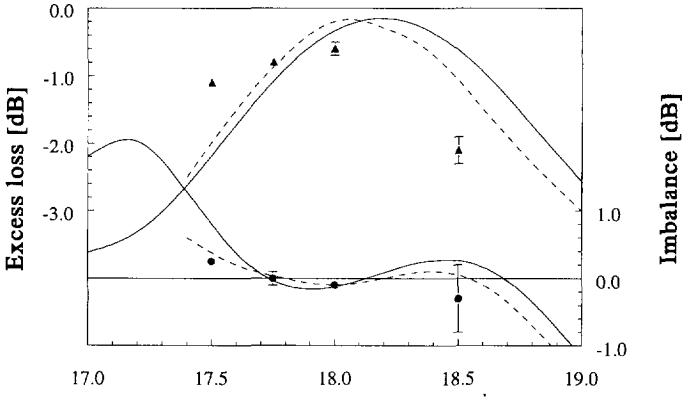

Figure 3.19 Tolerance to multimode section width at 1530 nm, TM polarization. Upper curves: calculated excess loss. Lower curves: calculated imbalance. Solid lines: MPA calculations. Dashed lines: BPM simulations. Markers: measured values. Bars: observed spread.

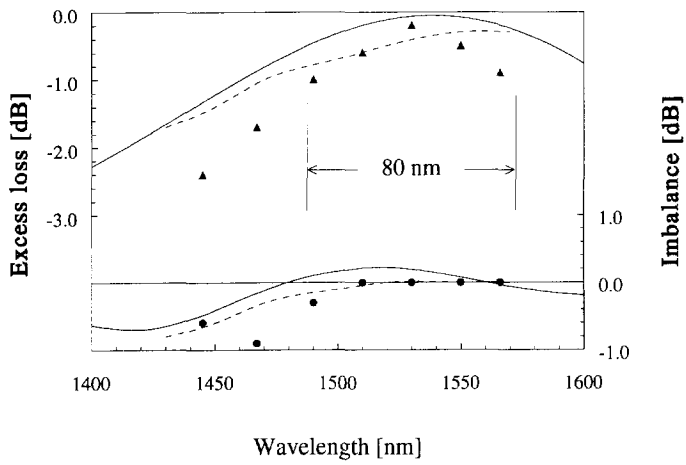

Figure 3.20 Excess loss and imbalance versus wavelength for $W_M = 18$ μm, TE polarization. Upper curves: calculated excess loss. Lower curves: calculated imbalance. Solid lines: MPA calculations. Dashed lines: BPM simulations. Markers: measured values.

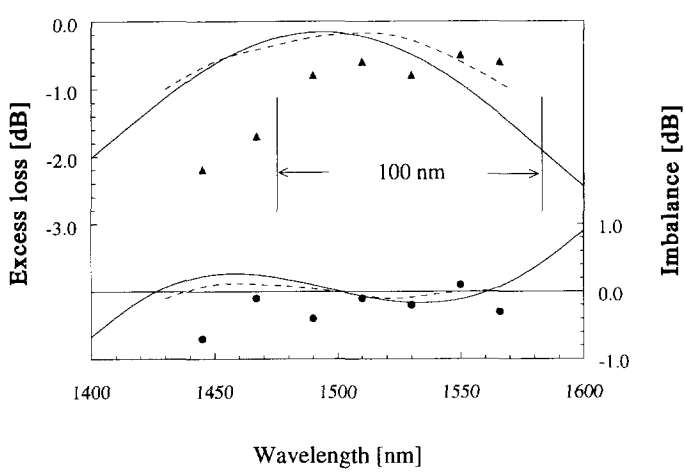

Figure 3.21 Excess loss and imbalance versus wavelength for $W_M = 18$ μm, TM polarization. Upper curves: calculated excess loss. Lower curves: calculated imbalance. Solid lines: MPA calculations. Dashed lines: BPM simulations. Markers: measured values.

show simulation and measurement results for TE and TM polarization obtained at different wavelengths, for the couplers with $W_M = 18$ μm.

3.4.6 Conclusions

We have investigated the performance sensitivity of InGaAsP/InP 3-dB MMI couplers to the multimode section length and width, the operating wavelength and the polarization. The experimentally determined large bandwidth, low polarization sensitivity and good fabrication tolerances are in rather good agreement with the simulations made with MPA and BPM.

From Figs. 3.16 and 3.17, it can be seen that the multimode section width (the most critical parameter in the fabrication of the MMI couplers) has to be controlled to within ± 0.25 μm in order to ensure a loss penalty below 1.0 dB. This result agrees very well with the the width tolerance predicted in Section 2.8. A lithography process as described in section 3.1.2 is capable of fulfilling this width tolerance.

By setting (arbitrarily) a 1.0 dB loss penalty, and a 0.2 dB imbalance, a bandwidth of 80 to 100 nm can be deduced from the data in Fig. 3.20 and Fig. 3.21, which is about twice the bandwidth reported for lithium niobate weak synchronous couplers [133]. This results agrees quite well with the wavelength tolerance predicted in Section 2.8.

From the measured values, a (full) loss penalty of about 0.3 dB can be expected for TM compared to TE polarization. As mentioned before, polarization independent operation can be achieved by designing at half-way between the optima for each polarization. In that case, both polarizations will share the same loss penalty (0.15 dB). No substantial degradation in the balance is measured for either polarization.

Because of their large bandwidth and polarization insensitivity, these devices have a great potential for application in WDM communication systems.

3.5 1×2 power splitter

A new type of planar integrated optical power splitter is presented here. The Multimode Power Splitter (MMPS) is based on the principle of symmetric modal interference in a multimode section. The device achieves equi-phase, balanced power partition from one single-moded input guide into two single-moded output guides. Simulations and experimental results show that low excess loss (around 1 dB) and very low imbalance (within 0.15 dB) can be attained with extremely short devices (20–30 μm for silica-based devices and 50–80 μm for InP-based devices).

3.5.1 Introduction

Equal optical power partition is of great importance to successfully achieve on-chip functions such as signal distribution, monitoring, mixing, etc. Two-way power splitting can be achieved by means of (very long) adiabatic Y-junction structures, or (lossy) diffraction-based structures.

For low-loss compact optical integrated circuits Two-Mode Interference (TMI) couplers [125] and, more recently, Multimode Interference (MMI) couplers [89, 135] based on the self-imaging principle have been reported. Although 2×2 TMI and MMI optical couplers can provide power splitting with good excess loss and imbalance figures, even better performance with respect to tolerance and device size can be obtained if only one (symmetrically positioned) input waveguide is applied, as described in subsection 2.4.2. Using this principle, simple and reliable equi-phase balanced optical power splitting can be realized with extremely small devices.

3.5.2 Operating principle

Figure 3.22 shows a structural view of the 1×2 Power Splitter. It consists of a straight input waveguide, a short multimode (MM) section and two single-moded curved output waveguides.

The principle of operation was described in general terms in section 2.4.2. The device presented here achieves the smallest possible size for a 1×2 MMI splitter by supporting the minimum of two symmetric modes. In this respect, it can be considered as a limiting case of the more general class of 1×N MMI splitters. Because of this, a simple understanding of the interference mechanism is possible by inspection of the modal evolution within the multimode section.

Figure 3.23 shows the evolution of the mode profiles within the multimode section. The input signal (In) excites the fundamental (HE00) and second-order mode (HE02). These modes propagate along the z-axis and, due to their different propagation constants, a phase difference accumulates. When this phase difference is equal to π, the total field profile (Out) is composed of the fundamental mode plus the second-order mode shifted by π. The resultant field profile presents two lobes and will couple with very high efficiency to the pair of single-moded output waveguides.

3.5.3 Design and modelling

The basic idea is to obtain mode interference between the fundamental and the second-order mode propagated in the multimode section. Hence, the width W_M must be chosen such that the multimode section supports more than two modes. In our design, for the purpose of achieving very small size, we have designed the multimode waveguide to support two symmetric modes. The single-moded input waveguide is centered with respect to the multimode section and will therefore excite only the even symmetric modes. In order to achieve the desired interference, the length of the multimode section must satisfy the following relation

$$L_M = \frac{\pi}{\beta_0 - \beta_2} = \frac{\lambda}{2(N_0 - N_2)} \tag{3.5}$$

where λ is the free-space wavelength, β_0 and β_2 are the propagation constants, and N_0 and N_2 are the effective indices of the fundamental and second-order mode in the multimode section.

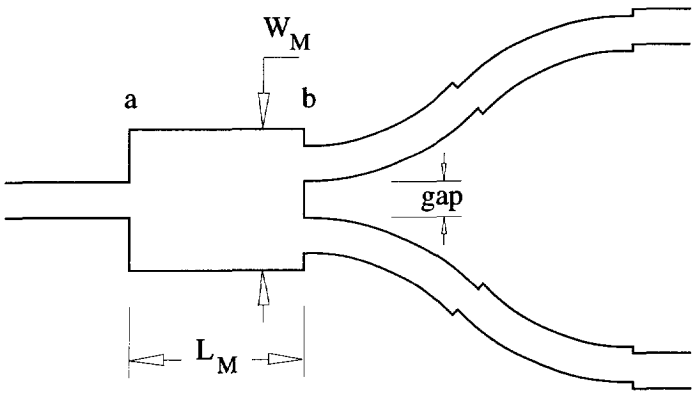

Figure 3.22 Schematic layout of the 1×2 power splitter. The input and output junctions are denoted by **a** and **b** respectively.

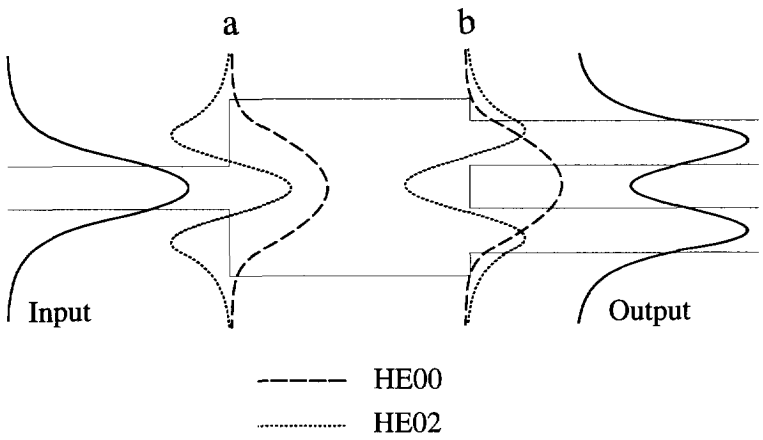

Figure 3.23 Mode amplitude evolution along the multimode section of the 1×2 power splitter. **a**: Input junction decomposition. **b**: Output junction reconstruction.

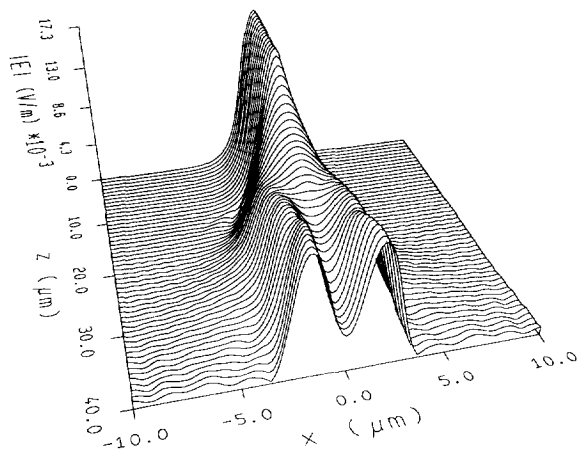

Figure 3.24 Beam Propagation Method (BPM) simulation of the intensity evolution in a 1×2 silica-based power splitter with $L_M = 20$ μm.

The propagation constants in all waveguides were calculated with the Effective Index Method (EIM). A one-dimensional overlap integral was applied for the computation of the excitation coefficients of the fundamental and second-order mode, at the beginning of the multimode section (input junction). The modal fields at the end of the multimode section (output junction) were calculated with the propagation constants of each mode, and the total field was obtained by adding these modal fields. The excitation coefficient of the total end field to the pair of output waveguides was computed with a one-dimensional overlap integral. The coupling between the output waveguides is not accounted for in this procedure.

Simulation results predict an optimum excess loss of 0.3 dB and perfect balance for a perfectly symmetric device. A 0.1–0.2 μm lateral misalignement at the input junction was predicted to cause a 0.01-0.05 dB extra excess loss and 0.04–0.16 dB imbalance, whereas a 0.2-μm misalignement at the output junction was predicted to increase the excess loss by 0.06 dB and produce a negligible imbalance of 0.01 dB.

A Beam Propagation Method (BPM) simulation of the device was performed, and the field evolution is shown in Fig. 3.24. It can be seen that the incoming power is divided into two equal-intensity lobes, which excite the fundamental modes of the output waveguides. The numerical results predicted an excess loss of ~0.75 dB. The discrepancy with the (lower) excess loss obtained by MPA is most probably due to a coupling between the output guides.

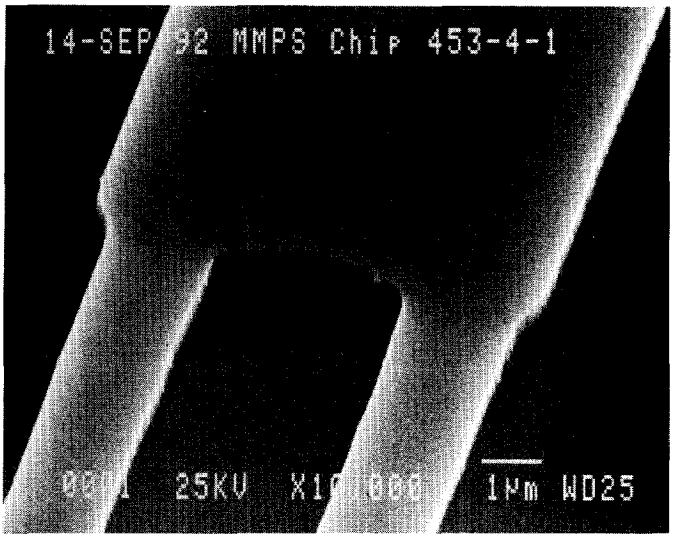

Figure 3.25 SEM photograph showing the output junction of the InP-based 1×2 power splitter. The multimode section length of these couplers is ~80 μm.

3.5.4 Experiments and discussion

The devices were designed and fabricated for operation at 1.52-μm wavelength, both for silica- and InP-based waveguides.

Two series of multimode power splitters were realized in silica-based aluminum oxide waveguides. The first series, with optimum design values of $W_M = 5.2$ μm, $L_M = 21$ μm and an output junction gap of 1.4 μm, was expected to show the lowest excess loss. The second series, with $W_M = 6.8$ μm, $L_M = 32$ μm and a gap of 2.4 μm, was expected to be slightly more tolerant to junction misalignments. The measurement data allowed to verify a somewhat lower excess loss for the smaller devices. As for tolerance to junctions misalignements, no difference was observed between the two series; most probably due to the fact that the non-intentional misalignments in the (optical) mask made imperceptible the effect of the intentional ones.

In order to test experimentally the sensitivity to the multimode section width, a number of devices were fabricated with W_M varying in a range of ± 0.3 μm, in steps of 0.1 μm. The impact of asymmetry on excess loss and imbalance was verified by purposely introducing a lateral misalignment of 0.1–0.2 μm in the input and output junctions of some devices.

Figure 3.26 shows the experimental results obtained for the first series (devices with $L_M =$

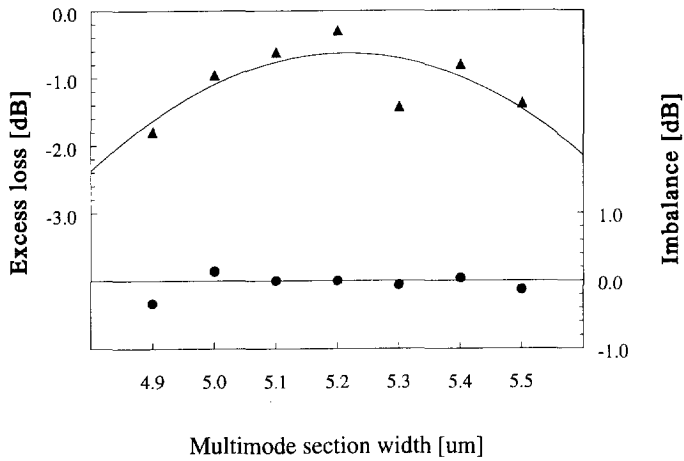

Figure 3.26 Experimental results obtained on a silica-based 1×2 power splitter with $L_M = 21$ μm. Triangles are measured excess losses (fitted by a parabola) and circles are measured imbalances.

21 μm and W_M ranging from 4.9 to 5.5 μm). An average excess loss of 1.0 dB and a 0.15-dB imbalance were measured for both series. Imbalances better than 0.1 dB were measured on 40% of all devices.

The measured average excess loss and imbalance in InP-based devices was 0.97 dB and 0.2 dB, respectively, with 30% of the devices showing imbalances better than 0.1 dB. Figure 3.25 shows a SEM picture of the output junction.

In conclusion, symmetric modal interference in a multimode section has been applied to achieve equi-phase balanced optical power splitting with very small and simple devices. Simulations and experiments performed on silica- and InP-based waveguide structures, indicate that well-balanced (within 0.1 dB) ultra-short (some tens of micrometres) 1×2 splitters can be achieved at the expense of some excess loss (~1.0 dB).

Chapter 4

Phase diversity network

This chapter describes the design and realization of an all-passive 4×4 integrated optical phase diversity network. The network makes use of the Multi-Mode Interference 3-dB couplers introduced in previous chapters, and a few other simple routing waveguide structures. The devices are fabricated in silica-based waveguides for operation at 1.55-μm wavelength. Measurement results suggest the feasibility of performing phase-diversity coherent detection by an all-passive photonic integrated circuit. This work was reported in a post-deadline paper at ECOC '91, Paris, September 1991, [62].

4.1 Introduction

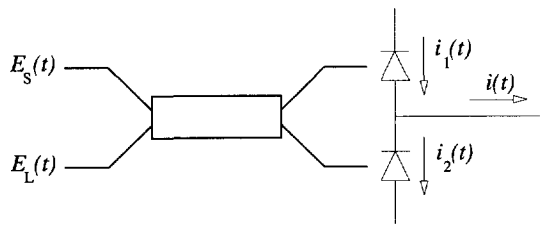

Figure 4.1 Diagram of an optical coherent receiver. The input and local oscillator signals are mixed in a 3-dB coupler. The balanced pair of photodiodes respond to (the average power of) the combined signals and deliver photocurrents $i_1(t)$ and $i_2(t)$. The current difference $i(t)$ is then amplified and fed to a demodulator circuit.

An (integrated) optical coherent balanced receiver (as shown in Figure 4.1) uses a 2×2 3-dB coupler to combine a (weak) input signal carrier field

$$E_S = \sqrt{P_S}\cos(\omega_S t + \varphi_S) \tag{4.1}$$

with a (much stronger) local oscillator field

$$E_L = \sqrt{P_L}\cos(\omega_L t + \varphi_L) \tag{4.2}$$

where P is the average optical power, ω is the optical frequency and φ is the phase. The balanced dual-detector configuration has the advantage of almost total relative intensity noise (RIN) suppression, and full use of the local oscillator power [136].

The received current $i(t)$ can be found [137] to be

$$i(t) = i_1(t) - i_2(t) = \frac{\eta e}{\hbar\omega}\sqrt{P_S P_L}\cos(\omega_{IF} + \varphi_{SL} - \frac{\pi}{2}) \tag{4.3}$$

where η is the quantum efficiency of the photodetectors (assumed identical), $\omega_{IF} = \omega_S - \omega_L$ is the intermediate frequency (IF), and $\varphi_{SL} = \varphi_S - \varphi_L$ is the relative phase between the signal carrier and the local oscillator.

Figure 4.2 depicts the received current $i(t)$ obtained from an optical carrier intensity-modulated (IM) by a binary data stream 010101...For a heterodyne system, in which $\omega_L \neq \omega_S$, the amplitude of the received data stream will fluctuate and fade away with a period $2\pi/\omega_{IF}$. A homodyne system ($\omega_L = \omega_S$) would in principle be free of this problem. However, unless the local oscillator is phase-locked to the signal, a fluctuation of the data stream will still be present due to the randomly varying relative phase φ_{SL}.

In practical heterodyne systems, the IF has to be 4 to 5 times higher than the signaling rate r in order to avoid negative effects of spectrum back-folding [138]. At high bit rates (over the Gbit/s level) this poses stringent speed requirements (up to approximately $6r$) to the receiver photodiodes and demodulation circuits. Homodyne systems, however, deliver a baseband signal to the photodiodes and demodulation circuits, demanding bandwidths of the order of r.* The price to be paid is the need to phase lock the local oscillator to the incoming signal carrier [139, 140, 141].

An elegant solution to the problem of phase noise in coherent systems is the phase diversity technique [142]. Phase diversity not only obviates the need for phase locking but also relaxes the laser linewidth requirements for frequency locking, at the cost of some system power penalty (0.25 dB for a 4×4 optical hybrid compared to an ideal heterodyne system) [143]. The basic idea is to obtain both the "in phase" $i_P(t)$ and the "in quadrature" $i_Q(t)$ current signals (shown in Figure 4.2) by suitable processing of the optical signal carrier and local oscillator. These currents show an antipodal behaviour, i.e. when one crosses zero, the other reaches a maximum. Thus, the baseband information stream can be recovered (demodulated) by adding the outputs of square detectors or simply (albeit some ripple) of envelope detectors [63].

*Note, though, that heterodyne systems require a faster *bandpass* demodulation circuit whereas homodyne systems require a slower *lowpass* demodulation circuit.

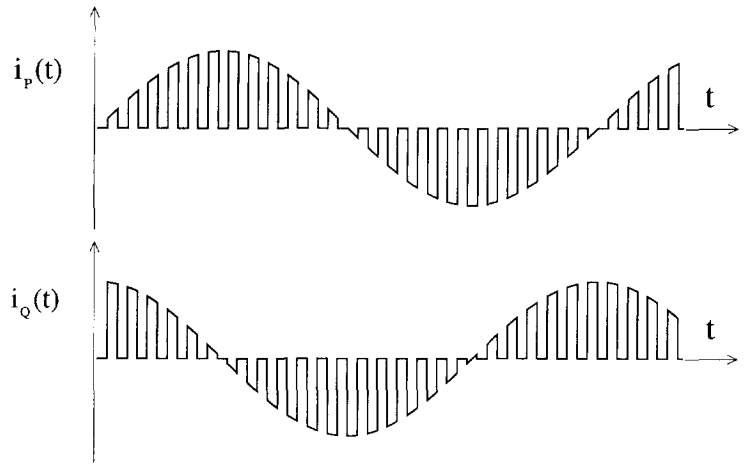

Figure 4.2 Received currents $i_P(t)$ and $i_Q(t)$ for the cases of "in phase" ($\varphi_{SL} = 0$) and "in quadrature" ($\varphi_{SL} = \pi/2$) input and local oscillator signals, respectively.

4.2 Design of the network

The combined output signals of one 3-dB coupler are 180° out of phase. A pair of 3-dB couplers could then deliver the quadrature combinations needed for phase diversity operation provided that their input signal phases are 0° and 90°. These inputs can be obtained by splitting the incoming signal and local oscillator, and delaying one path by 90°.

Figure 4.3 shows a schematic diagram of a 4×4 phase diversity network, using this principle. The network comprises four 2×2 3-dB couplers, a phase-shifter and an intersecting waveguide; and it is suitable for planar integration.

4.2.1 Intersecting waveguides

The intersecting waveguides should provide cross-over of the optical signals with as small as possible insertion loss and crosstalk. Theoretical and experimental studies of $LiNbO_3$ X-junctions with small intersecting angles (<10°) [144, 145] have predicted that crosstalk figures as low as −30 dB are achievable at angles of ~ 5° ± 0.25°, with insertion losses of about 1.5 dB. Waveguide crossings with such small intersecting angles will suffer from severe blunting unless fabricated by a (critical alignment) two-masking step process.

Insertion losses of 0.04–0.06 dB in silica- and GaAs-based waveguide crossings at right angles have been inferred by measurements in multi-cross spiral structures [146, 147].

A possible alternative could be the use of cross-couplers to realize the cross-over function. Following some experiments [66], this approach was discarded in order to reduce the number

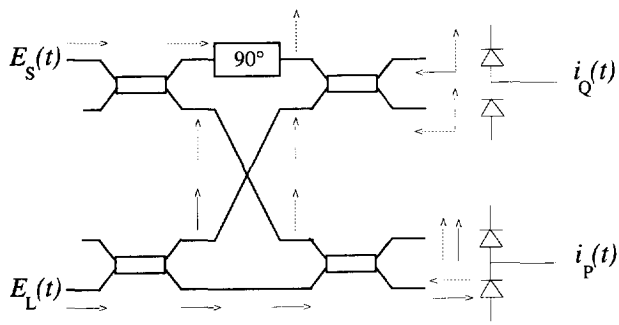

Figure 4.3 Schematic diagram of a phase diversity network. Arrows indicate the phases of the optical signals at various points.

of critical design parameters in the network.

In principle, it is desirable to have small-angle intersecting waveguides in order to keep the whole network as small as possible. The requirement is not severe though, as the lateral dimension of our network had to be chosen to accomodate two optical fibers (125-μm diameter) at its inputs, which allows for large-angle crossings to be used.

An extension of the analytical results —although not completely correct, because the original treatment [148] makes some approximations which hold true for small intersecting angles— could provide some indicative idea of the performance behaviour for large intersecting angles, say 30–90°. After experimenting on a number of silica-based X-junctions with varying angles, we found that intersecting angles larger than about 40° showed insertion losses of less than 0.3 dB and negligible crosstalk. For our design we applied large, conservative angles of 62°.

4.2.2 The phase-shifter

The phase-shifter is realized by decreasing $\lambda/4$ one optical path within the network. Figure 4.4 shows the basic geometry of the phase-shifter. The different optical length is achieved by a reduction of the radii of the bends and the addition of a straight segment to complete the path. The phase shifts through the upper and lower optical paths are, respectively

$$\phi_2 = \beta_2\, 2\theta \tag{4.4}$$

$$\phi_1 = 2\beta_1\theta + \beta_S L_S \tag{4.5}$$

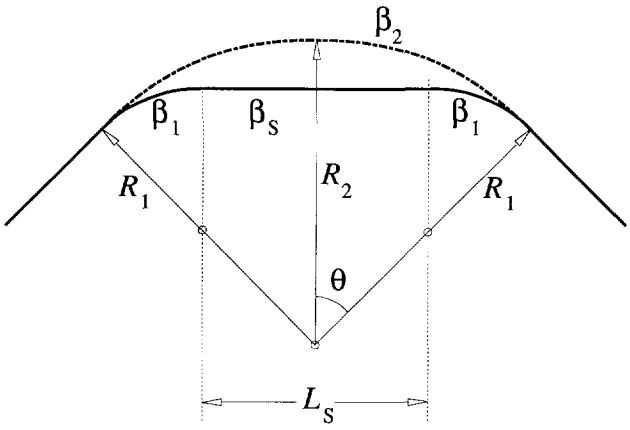

Figure 4.4 Basic geometry of the phase-shifter. The solid-line path (curves of radii R_1 and angle θ, and straight segment of length L_S) presents a shorter optical length than the dashed-line path (curve of radius R_2 and angle 2θ).

where the β_1 and β_2 are the propagation constants in the curved waveguides (in rad/rad), θ is the curve angle, β_S is the propagation constant in the straight waveguide (in rad/μm), and L_S is the length of the straight waveguide. The propagation constants β_1 and β_2 depend on the radii R_1 and R_2, and can be calculated by a (conformal) transformation to an equivalent straight guide [149]. As shown in Fig. 4.3, the optical phase difference of both paths must be

$$\phi_2 - \phi_1 = \frac{\pi}{2} \tag{4.6}$$

The design values can be calculated by trial and error. Given the waveguide characteristics, the curve angle θ and the radius R_2, the phase shift through the upper path follows from Eq. (4.4). A radius R_1 ($< R_2$) is chosen, and the length of the straight segment is calculated as

$$L_S = 2(R_2 - R_1)\sin\theta \tag{4.7}$$

The optical phase difference through the lower path can then be calculated with Eq. (4.5) and compared to the result of Eq. (4.4). The process is eventually repeated until Eq. (4.6) is fulfilled.

A slightly asymmetric version of the basic phase-shifter shown in Fig. 4.4 was used in our design, in order to comply with the requirements of access channel separation. The values obtained are $R_2 \approx 300$ μm, $R_1 \approx 290$ μm, $\theta \approx 25°$, and $L_S \approx 7$ μm.

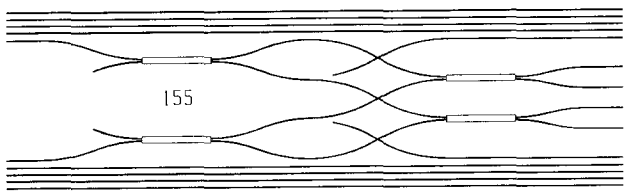

Figure 4.5 Layout (75×) of the phase diversity network. The two input channels can be seen on the left, and the four output channels on the right. Lateral straight waveguides running alongside the device provide reference for loss measurements. Two extra channels allow monitoring of the X-junctions. Total device dimensions are 270 μm × 1.2 mm

4.3 Realization of the network

Figure 4.5 shows the layout of the phase diversity network, which is based on the scheme given in Fig. 4.3. The first pair of MMI 3-dB couplers splits the input and local oscillator signals, which are routed and fed into the second pair of MMI 3-dB couplers. The optical phases are ensured equal throughout the four routing channels by using identical (except for the phase-shifter) curved paths and X-junctions. Additionally, this topology provides two extra output channels which allow in-situ monitoring of the X-junctions; low crosstalk will result in low optical power from the extra channels.

A series of networks was designed and fabricated in silica-based waveguides for operation at 1.55 μm wavelength. The networks comprise MMI 3-dB couplers (as described in Chapter 3 and [59]) with varying multimode section lengths. All access and routing waveguides were 2 μm-wide, and curves have radii in the order of 300 μm. Offsets were applied between straight and curved waveguides (0.1 μm centre-to-centre) and between bends of opposite curvature (0.2 μm), in order to minimize transition losses.

An input channel separation of 270 μm is sufficient to prevent input crosstalk and allow for the signals to be delivered from a pair of optical fibres. Each of the four output channels is spaced by about 50 μm in order to ease spatial signal separation during measurements. These requirements would be much less severe in the case of monolithic integration, opening the way to further miniaturization.

4.4 Experimental results

Figure 4.6 shows the measurement setup for the characterization of the phase diversity

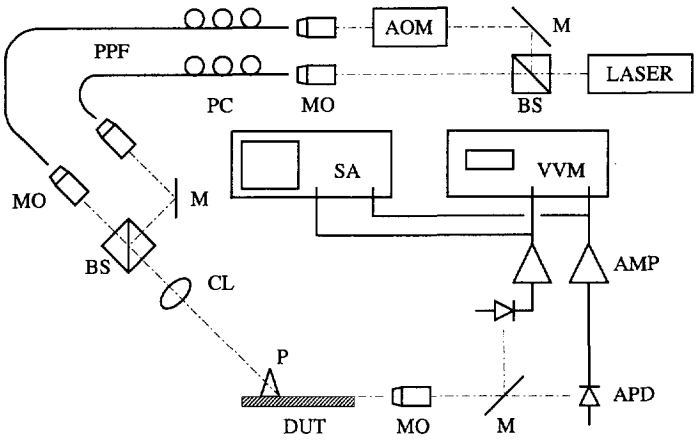

Figure 4.6 Measurement setup mounted at TU Eindhoven for the characterization of the phase diversity networks. M: mirror, BS: beam splitter, AOM: acousto-optic modulator, MO: microscope objective, PC: polarization controller, PPF: polarization-preserving fibre, CL: cilindrical lens, P: prism, DUT: device under test, APD: avalanche photodiode, AMP: amplifier, VVM: vector voltmeter, SA: spectrum analyzer.

networks. Both input channels are excited with signals derived from the same 1.55-μm wavelength laser source. One derivation goes directly into one output channel and the other one is first (frequency-shift) modulated by an acousto-optic modulator driven at 80 MHz. An optical isolator is included to suppress interfering back reflections to the laser. Two polarization controllers permit the setting of the polarization of the input fields. The signals from the four output channels are detected in pairs (in order to allow phase comparison) by two germanium APDs, amplified and fed to a spectrum analyzer and a vector-voltmeter.

The results of the measurements are shown in Fig. 4.7. The measured intensity and phase are represented by a vector on a pair of orthogonal axes. The best observed phase deviations were 5°/12°/12°/9°. Based on a previous paper on this subject [150], we calculated for these phase deviations a 3.3-dB sensitivity degradation with respect to an ideal 4×4 network. This figure can be reduced to 1.5 dB when the phase deviations are known *a priori*, so the system can be compensated accordingly. The measured excess loss was around 3 dB, and the maximum imbalance (power ratio between any two output channels) was within 0.5 dB. Devices with lower excess losses (around 1.5 dB) were also observed, although presenting somewhat larger output phase deviations.

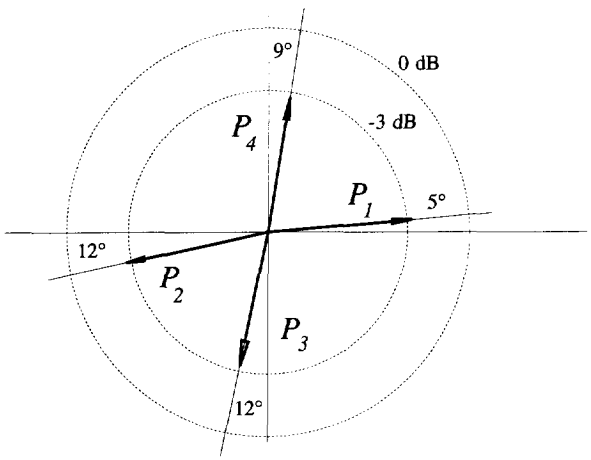

Figure 4.7 Measured optical output intensities and phases. The outer circle represents 0-dB losses and the inner circle represents −3-dB losses. Also shown are the phase deviations from ideal behaviour.

4.5 Conclusions

The experiments suggest that all-passive phase diversity operation is in principle feasible. From Fig. 4.7, it can be seen that each pair of signals delivered by the output MMI couplers (i.e. P_1-P_2 and P_3-P_4) are very nearly in antiphase. This pattern was observed in all measured devices, and indicates corrrect behaviour of the MMI 3-dB couplers. The fact that both pairs of output channels are not exactly in quadrature is due to non-ideal performance of the 90° phase-shifter. The good performance of the passive phase-shifter relies on the uniformity of the fabrication process. In those cases in which uniformity cannot be assured, an active phase control might then provide reliable, penalty-free oparation.

Very compact implementations of optical hybrids for phase diversity operation, based on one single 4×4 MMI coupler, have been demonstrated in Schott glass [85], in ion-exchanged waveguides [86, 151], and in InGaAsP/InP material [87].

Chapter 5

Polarization splitters

This chapter reports a passive TE/TM mode polarization splitter based on a Mach-Zehnder interferometer. The device was made by a two-mask process in InGaAsP/InP waveguides. Insertion loss of 1.5 dB and extinction ratios of −19 dB for TE and −15 dB for TM have been measured at 1510-nm wavelength. A large optical bandwidth is obtained by using a pair of MMI 3-dB couplers and a wavelength-tolerant birefringent phase shifter. The results of this work were reported in Phot. Tech. Letters, March 1994, [64].

5.1 Introduction

In order to obtain a maximum (and stable) combined signal in a coherent detector, the input field and the local oscillator field must have (and keep) the same state of polarization. Also, some waveguide devices require the light to be linearly polarized for efficient operation. However, the state of polarization of a signal travelling through an optical fibre suffers (random) fluctuations. This phenomenon is due to birefringence of the optical fibre and coupling effects between the two orthogonal states of polarization in which a generic field propagating in an optical fibre can be decomposed. Coupling is caused by physical imperfections of the material (inhomogeneity and anisotropy) and mechanical perturbations of the fibre (kinks, bending, squeezing, twist, strain, etc). These mechanisms depend on environmental conditions and produce random variations with (non-uniform) time periods ranging from seconds to minutes.

Several methods have been proposed to either control the state of polarization of the incoming signal, or obviate the problem of its fluctuation. Polarization maintaining fibres permit light to pass through whilst retaining its state of polarization. Its high losses (~2 dB/km) and cost, however, limit its use to a few special applications. Electro-mechanical (e.g. fibre squeezers) or electro-optic (e.g. Faraday rotators) polarization controllers working in feedback loops suffer from large size, complexity, slow response, and mechanical fatigue.

So far, the most practical solutions to polarization fluctuations are polarization diversity

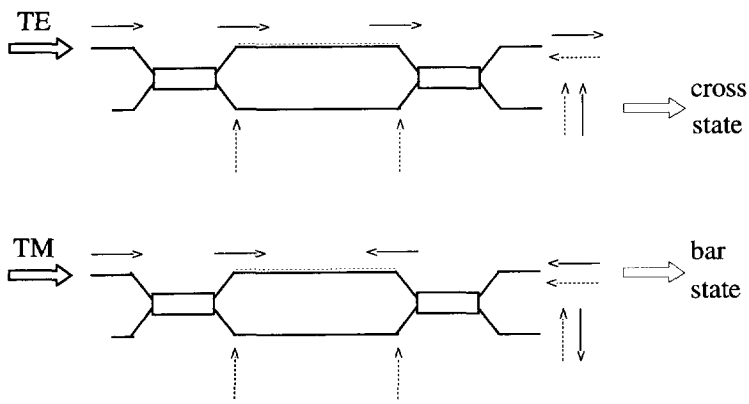

Figure 5.1 Evolution of the signal phases (shown by thin arrows at different points in the device) in a Mach-Zehnder interferometer TE-TM splitter. The TE components keep their relative phase through the differential arms, whilst the TM components build a phase shift of π at the end of the differential arms.

[152] and rather special formats of polarization modulation [153]. Spatial TE/TM mode splitting is crucial for polarization diversity receivers [154, 155, 156], as well as for polarization shift keying [157] and polarization-multiplexed systems [158]. Several polarization splitters have been studied which are based on different operating principles. Asymmetric Y-branches on $LiNbO_3$ were reported [159] in which the effective indices were electro-optically controlled. The polarization-dependent phase shift in a pair of length-compensated nitride-loaded silicon-based waveguides was exploited in an interferometer polarization splitter [160]. Polarization splitters based on metal-cladded directional couplers in InGaAsP/InP were demonstrated [161]. More recently, a mode evolution splitter has been reported [162] which exploits the large birefringence of first-order modes in ridge waveguides.

This chapter describes the design, fabrication and measurement results of a passive Mach-Zehnder Interferometer (MZI) polarization splitter in InGaAsP/InP. It is demonstrated that waveguides with equal TE propagation constants –while still having a convenient difference in TM– can be realized by suitably loading a ridge waveguide with a dielectric (SiO_2) layer and a metal layer on top. Based on this concept, two *equal-length* waveguides (which we call differential arms) can be fabricated which are capable of providing the desired TM phase shift of π within the MZI, without introducing any TE phase shift. This approach has the advantage of obviating the need for a critical compensating length in the differential arms, and/or the tuning of the waveguide widths.

5.2 Principle of operation

The principle of operation of the Mach-Zehnder interferometer polarization splitter is shown in Fig. 5.1. The device consists of two 3-dB couplers, and a pair of non-equally birefringent straight waveguides of equal length (differential arms). These arms are designed in such a way as to present no relative phase shift for TE-polarization, and a relative phase shift of π for TM-polarization, i.e.

$$\Delta\phi_{\mathrm{TE}} = k_0(N_{\mathrm{TE}}^{\mathrm{ms}} - N_{\mathrm{TE}}^{\mathrm{sl}})L_{\mathrm{D}} \doteq k_0\,\Delta N_{\mathrm{TE}}\,L_{\mathrm{D}} = 0 \tag{5.1}$$

$$\Delta\phi_{\mathrm{TM}} = k_0(N_{\mathrm{TM}}^{\mathrm{ms}} - N_{\mathrm{TM}}^{\mathrm{sl}})L_{\mathrm{D}} \doteq k_0\,\Delta N_{\mathrm{TM}}\,L_{\mathrm{D}} = \pi \tag{5.2}$$

where $k_0 = 2\pi/\lambda$ is the wavenumber, λ is the free-space wavelength, N is the effective refractive index, L_{D} is the length of the differential arms, and the superscripts *ms* and *sl* refer to the metal-SiO_2 cladded waveguide and the strip-loaded waveguide respectively, which will be explained shortly.

The first 3-dB coupler splits the (randomly polarized) input signal into two quadrature (+90° relative phase) components, which are fed into the differential arms. Because of the equal TE propagation constants, the TE components will keep their relative phase (+90°) all along the differential arms and, when combined in the second 3-dB coupler, will interfere destructively at the bar output and add up at the cross output port. The TM components, because of the phase shift of π introduced by one arm, will reach the input of the second 3-dB coupler with a relative phase of −90° and, when combined, will cancel out at the cross output and add up at the bar output port.

5.3 Design considerations

A metal layer applied directly on top of a ridge waveguide causes a very strong reduction in the TM effective index [161], with a small decrease in the TE effective index and a large attenuation for both polarizations. The inclusion of a (low-index) dielectric layer between the waveguide and the metal can compensate the TE index decrease and bring the propagation losses of both polarizations to acceptable levels [164], while still providing a useful difference in the TM effective index. This allows the design of a metal-SiO_2 cladded waveguide with equal TE effective index as the strip-loaded waveguide. A cross-section of the metal-SiO_2 cladded and strip-loaded waveguide structures is shown in Fig. 5.2.

The real and imaginary parts of the effective indices were calculated for both structures by using the Effective Index Method with complex refractive indices for the metal layers [163]. The Fiedler and Schlachetzki model [100] was used to calculate the refractive indices of InP and of lattice-matched quaternary $In_{0.72}Ga_{0.28}As_{0.61}P_{0.39}$ ($\lambda_g = 1.3\ \mu$m) at different wavelengths. Figure 5.3 shows the differences in the real part of the effective indices N_{TE} and N_{TM} –as defined in Eqs. (5.1) and (5.2)– between the metal-SiO_2 cladded and the strip-loaded

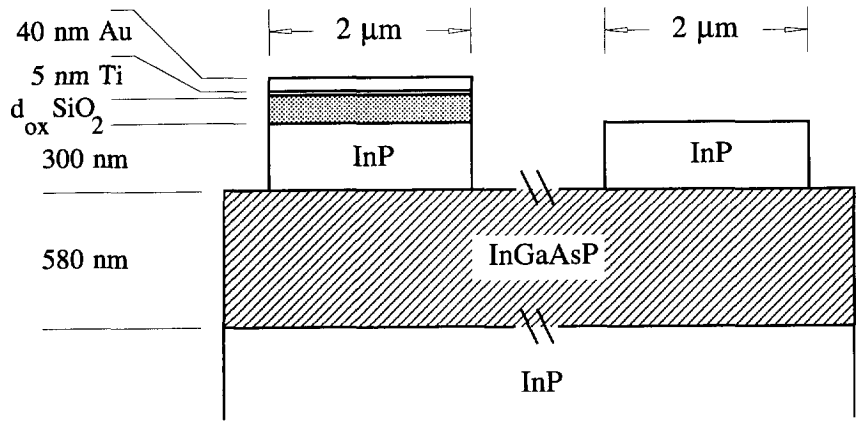

Figure 5.2 Cross-section of the metal-SiO_2 cladded waveguide (left) and the strip-loaded waveguide (right) structures. The refractive indices are: n(Au)=0.18−j10.2, n(Ti)=3.70−j4.50 [163], n(InP)=3.17, n(InGaAsP)=3.39 [100], and $n(SiO_2)$=1.444 [66] at 1550-nm wavelength.

waveguide, calculated as a function of the SiO_2 layer thickness d_{ox}. Metal layers thicker than 30 nm do not further modify the effective refractive index differences. At $d_{ox} \approx 120$ nm, it is found $\Delta N_{TE} = 0$, which fulfils Eq. (5.1) for any value of L_D. For this value of d_{ox}, $\Delta N_{TM} = 4.3 \times 10^{-4}$ and Eq. (5.2) is thus fulfilled with L_D=1.76 mm.

The attenuation penalty due to the presence of metal in the metal-SiO_2 cladded waveguide decreases exponentially with the SiO_2 thickness (Fig. 5.4), and for $d_{ox} = 120$ nm it is found to be ~1.8 dB/cm for TE and ~0.8 dB/cm for TM.

A schematic layout of the Mach-Zehnder polarization splitter is shown in Fig. 5.5. MMI couplers were used because of their good fabrication tolerances, polarization independence and large optical bandwidth [99]. All access waveguides were 2 μm-wide. In order to minimize losses [65], lateral offsets were applied at the straight-to-curve transitions (0.15 μm) and at the curve-to-curve transitions (0.30 μm). The total device is 3.3-mm long, which includes 1.0-mm radius curved access waveguides with a 50-μm separation.

5.4 Fabrication of the devices

Figure 5.6 shows the fabrication sequence of the Mach-Zehnder polarization splitter. The devices were realized on a non-intentionally doped InP/InGaAsP/InP wafer grown by low-pressure MOVPE [105]. After sputtering a 120-nm SiO_2 film onto the whole wafer, a thin (~5 nm) Ti layer (to improve the adherence of Au) and a 40-nm Au layer were deposited

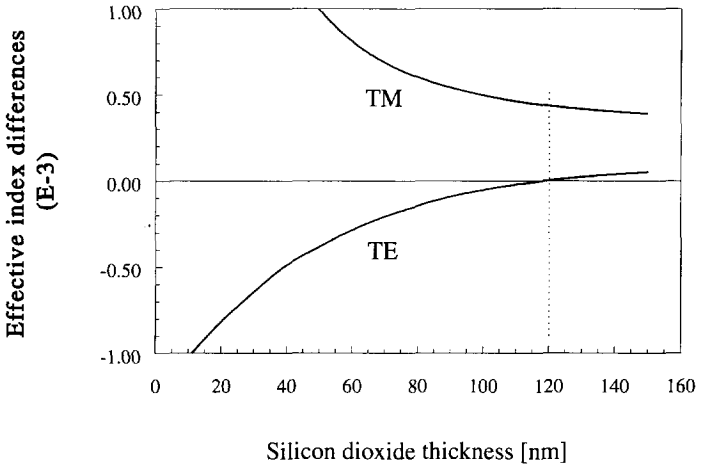

Figure 5.3 Calculated refractive index differences ΔN_{TE} and ΔN_{TM} (from Eqs. (5.1) and (5.2)) between the metal-SiO_2 cladded waveguide and the strip-loaded waveguide, as a function of SiO_2 layer thickness d_{ox}. The dotted line indicates the design value of d_{ox} for which ΔN_{TE}=0.

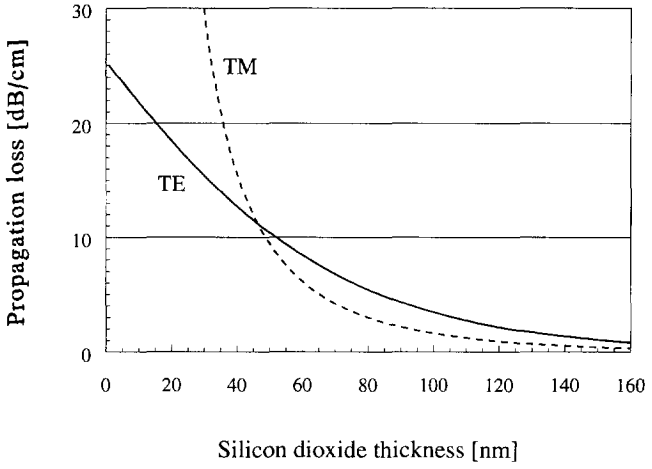

Figure 5.4 Calculated loss in a 2 μm-wide metal-SiO_2 cladded waveguide with 40-nm Au and 5-nm Ti, as a function of SiO_2 layer thickness.

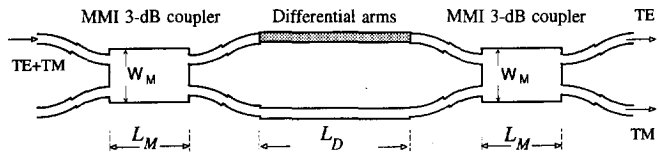

Figure 5.5 Schematic layout of the Mach-Zehnder interferometer polarization splitter. It consists of two MMI 3-dB couplers with length L_M and width W_M, and a pair of differential arms of length L_D. The shaded area indicates the metal-SiO_2 cladding on top of the strip-loaded waveguide.

by e-beam evaporation. The first photolithography step (which defines the entire layout) was optimized in terms of photoresist thickness, exposure time and reversal bake in order to minimize the effects of a standing wave intensity due to the reflecting (Au) surface [107], at the exposure wavelengths of 405 nm (h-line) and 436 nm (g-line). The waveguides were patterned with two reactive-ion etching (RIE) steps: Metals and SiO_2 layers were etched in a CHF_3 plasma RIE. The 300-nm InP top layer was etched by a self-aligned CH_4:He RIE [111]. A second (non-critical alignment) standard photolithography covers one differential arm of the device, allowing the removal of the unwanted metals and SiO_2 by wet chemical etching. The samples were anti-reflection coated by depositing a $\lambda/4$ layer of SiO_x on the cleaved facets.

5.5 Experimental results

We fabricated a series of MZI polarization splitters with L_D varying from 1.5 to 2.0 mm in steps of 20 μm and MMI 3-dB couplers with L_M=425 μm and W_M=15.8, 16.0 and 16.2 μm. In order to test the individual performances of the MMI 3-dB couplers, we integrated a series of them with lengths L_M ranging from 415 to 435 μm in steps of 5 μm, and widths W_M ranging from 15.6 to 16.4 μm in steps of 0.2 μm. These 3-dB couplers showed excess loss below 1.0 dB and imbalance within 0.2 dB, for a length tolerance of $\pm$5 μm and a width tolerance of $\pm$0.2 μm, as reported in Chapter 3. Attenuation on 2 μm-wide strip-loaded straight (reference) waveguides was determined to be 1.2 dB/cm for TE and 2.8 dB/cm for TM, from transmission measurements, a two-dimensional overlap calculation of the mode mismatch, and an analytical approximation of the facet reflectivity [165]. These results agree to within $\pm$0.3 dB/cm with loss measurements performed on similar waveguide structures by the Fabry-Perot resonance method [166]. The metal-SiO_2 cladded waveguides showed 3.3 dB/cm for TE and 3.7 dB/cm

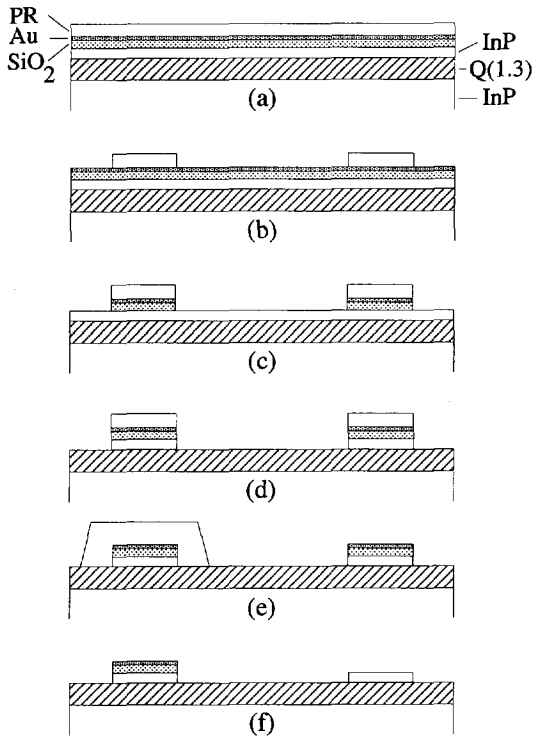

Figure 5.6 Fabrication process sequence of the Mach-Zehnder polarization splitter. (a) Initial layer stack (top to bottom): photoresist (PR), gold (Au), SiO_2, InP, InGaAsP (Q(1.3)), InP. (b) First photolithography. (c) CHF_3 plasma RIE. (d) CH_4:He RIE. (e) Photoresist removal and second photolithography. (f) Wet chemical etching of metals and SiO_2.

for TM.

The MZI polarization splitters were characterized by launching alternatively TE- and TM-polarized light into one input, recording the light from both outputs and repeating the process for the other input. Light was end-fire coupled by focusing a pair of 40× (0.65 NA) infra-red anti-reflection coated microscope objectives at the cleaved facets. The outputs were imaged onto a Ge photodiode and read by a lock-in amplifier.

Figure 5.7 shows the insertion loss and extinction ratio measured with a 1507-nm Fabry-Perot laser on a number of devices with varying L_D. Typical insertion loss of 1.5 dB (with respect to straight reference waveguides) was observed for both polarizations in the vicinity of L_D=1.76 mm. As expected, TE extinction ratio remains quite constant for all devices. Its slight droop is most probably due to the fact that ΔN_{TE} (though very low) is not exactly zero. The

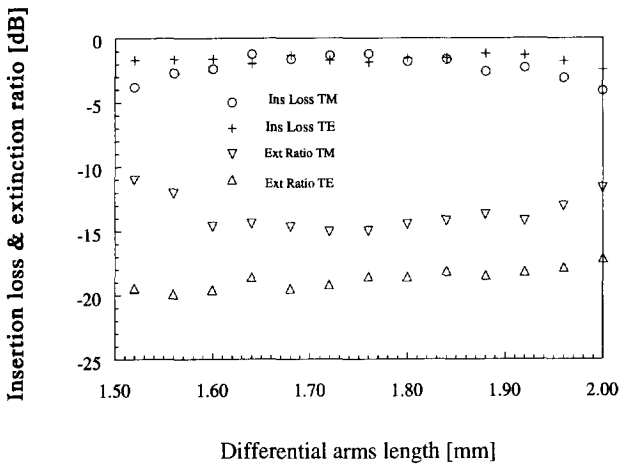

Figure 5.7 Measured insertion loss and extinction ratio as a function of differential arms length L_D, obtained with a 1507-nm centre wavelength FP laser.

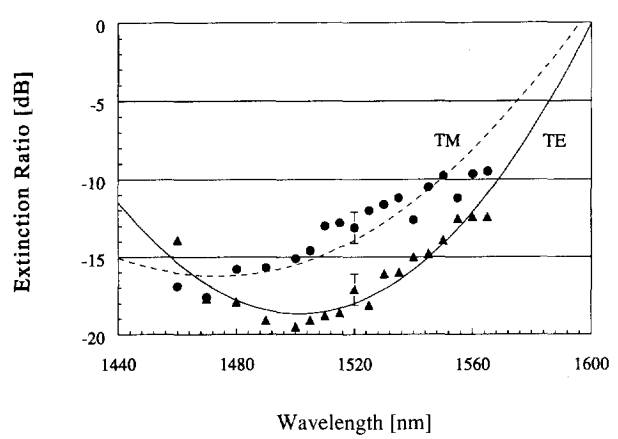

Figure 5.8 Measured extinction ratio versus wavelength for a device with L_D=1.76 mm obtained with an external cavity tunable laser. Each marker is the average of two measurements (one for each input), with the typical observed spreads shown as vertical bars. Solid and dashed lines are parabolic fits.

extinction ratio for TM shows a soft maximum around L_D=1.76 mm. The difference between TE and TM extinction ratios is partly due to a somewhat larger TM imbalance in the MMI 3-dB couplers.

Figure 5.8 shows the extinction ratio as a function of the wavelength, measured on a device with design value dimensions (L_D=1.76 mm, L_M=425 μm and W_M=16.0 μm). Each marker represents the average of two measurements (one for each excited input port). The best TE extinction ratio was -19 dB at 1500 nm, in good agreement with the design wavelength of 1510 nm. TM reaches a best extinction ratio of -17 dB at 1470 nm. We attribute this discrepancy to the uncertainty in the value of the metals' refractive indices. Over a 60-nm wavelength range the TE (TM) extinction ratio remains below -16 dB (-13 dB).

5.6 Conclusions and proposals

A polarization splitter based on a Mach-Zehnder interferometer has been reported. The desired TE and TM phase shifts were realized with a metal-SiO_2 cladding on a rib-loaded waveguide. The devices were fabricated in InGaAsP/InP waveguides with a rather simple two- mask process. The design requires, however, a good control of the SiO_2 layer thicknesses and its refractive index, in order to accurately compensate the influence of the metal layer for TE polarization. For example, a $\pm 10\%$ deviation from the optimum SiO_2 layer thickness would result in a 5-dB penalty in the extinction ratio. At 1510-nm, we measured extinction ratios of -19 dB for TE and -15 dB for TM, insertion losses of about 1.5 dB for both polarizations, and large bandwidth.

Based on the property of metal layers to depress the TM effective index in optical waveguides (while the TE index remains almost unchanged), we propose a polarization splitter based on an MMI coupler with a partially metal-cladded multimode waveguide section. A top view of the device can be seen in Fig. 5.9, along with plots of the TE and TM effective indices across the multimode waveguide. A (good conductor, e.g. Au) metal layer is deposited over the length of the multimode section, covering the central area defined by the gap between the access waveguides. The length of the multimode section should be equal to $3L_\pi$, in such a way that for TE-polarized light (which will practically not "feel" the presence of the metal layer) the coupler is in the cross state. TM-polarized light, however, "sees" a system of parallel waveguides and (if the index depression is large enough and/or the coupler is short enough) will go through to the bar output. The optimization of these parameters, together with the realization of polarization splitters based on this principle, is presently being pursued by our research group.

Figure 5.10 shows preliminary results of BPM calculations on a polarization splitter based on this concept, which suggest its viability. In addition, MPA simulations predict a TE (TM) insertion loss of $\sim$2 dB ($\sim$0.6 dB) and extinction ratio of approximately -21 dB (-10 dB).

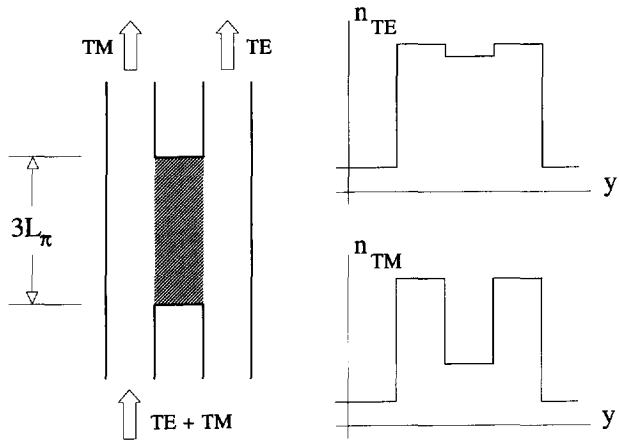

Figure 5.9 Top view of the proposed depressed-index profile (DIP) polarization splitter, based on a metal-cladded multimode waveguide (the shaded area indicates the metal layer), and lateral refractive index profiles for both polarizations within the multimode waveguide.

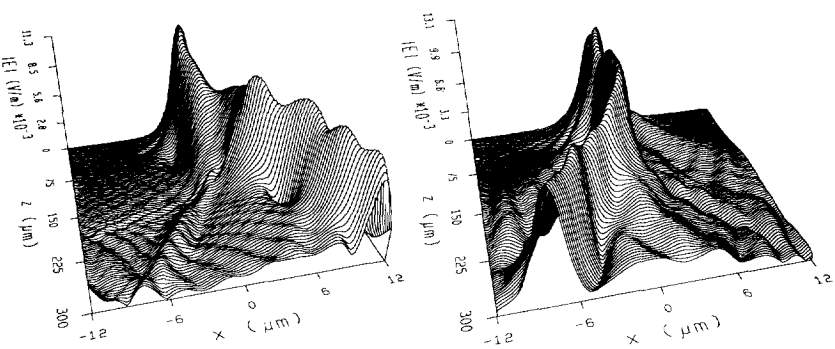

Figure 5.10 BPM-calculated field profile evolution in the proposed DIP polarization splitter for TE-polarization (left) and for TM-polarization (right). The simulated device was based on an InGaAsP/InP strip-loaded structure, $\sim$ 150-μm long, with a gap of $\sim$2 μm, a 6° output Y-shaped flare, and 2 μm-wide access waveguides.

Chapter 6

Conclusions

MMI devices have emerged as a new class of components which can provide coupling and splitting from/into a number of channels, with low loss and good balancing. As such, they might be compared to more conventional devices performing similar functions, such as directional couplers, adiabatic elements (X- or Y-junctions), diffractive structures (tree- or star-couplers), and two-mode interference (TMI) couplers. Table 6.1 summarizes important characteristics of coupling and routing devices. The table provides an overview of experimental performances, and is intended for a general comparison between classical components and MMI devices. However, it should be used with care; the reported works encompass a number of different materials and wavelengths.

In addition to the figures presented in Table 6.1, some other (non-quantifiable) advantages of MMI devices are worth mentioning. Firstly, the design procedure can be performed quite easily; all that is needed is to calculate first the beat length L_π with Eq. (2.7) and then to obtain the imaging length with Table 2.1 for the chosen structure. Secondly, cascadeability is not an issue; it is possible to obtain well-balanced 1-to-N splitting with just one single MMI device, albeit with an optical bandwidth penalty. Thirdly, MMI structures are compatible with both weakly guiding waveguides as well as with deeply etched waveguides, and are almost completely independent of the transverse structure.

Novel geometries and applications are currently being investigated, with promising results. Symmetric-interference 1×1 may be useful for filtering out the unwanted lowest order anti-symmetric mode of an input guide, while linearly tapered 1×1 or 1×2 MMI power splitters can act as field transformers in transitions between waveguides of different width [173]. Very recently, restricted-interference mechanisms were found which perform certain non-uniform (e.g. 28/72 or 15/85) splitting functions in 2×2 couplers. Based on this, MMI couplers with up-down tapered multimode sections were demonstrated which allow the free choice of the splitting ratios within a few percents [174], thus opening the way for these devices to perform "tap" functions in communication networks, and allowing more freedom in the design of ring

Device type and material		*Ref.*	*Inputs* × *outputs*	*Excess loss* [dB]	*Imbalance* [dB]	*Bandwidth* [nm]	*Polarization penalty* [dB]	*Size*
Y-junction	(G)	[167]	1×2	2.0–6.0	0.1–0.5	large	low	< 6°
X-junction	(L)	[144]	2×2	<1.0	>20	large	low	> 6°
Parallel coupler	(S)	[168]	2×2	0.1–0.2	0.6	200	0.3	4 mm
TMI coupler	(I)	[127]	2×2	1.0–3.0	0.1	15		400 μm
MMI coupler	(I)	[80]	2×2	0.1–0.3	<0.05	(100)	0.2	240 μm
MMI coupler	(I)	[99]	2×2	0.3–0.6	<0.1	80–100	0.3	530 μm
Tree-coupler	(I)	[169]	1×16	2.0–3.0	2.6–4.0		<1.0	~1 mm
MMI splitter	(G)	[91]	1×2 ...20	~0	0.35			N×120 μm
MMI splitter	(I)	[93]	1×4	0.1	0.1	(60)		300 μm
MMI splitter	(I)	[170]	1×16	2.2	1.5		0.4	140 μm
Star-coupler	(S)	[171]	19×19	1.5	2.0			7.5 mm
Star-coupler	(S)	[172]	8×8	1.4–1.7	1.3–1.5	200	0.3	1.5 mm
MMI coupler	(I)	[87]	4×4	1.0	0.3–0.9		0.2	945 μm
MMI coupler	(G)	[88]	10×10	≤3.0	0.1–0.2			3270 μm

Table 6.1 Representative characteristics and experimentally measured performances of integrated optical routers and couplers. The material is denoted by (I): InGaAsP/InP, (G): GaAs/AlGaAs, (L): $LiNbO_3$, and (S): SiO_2. Parenthesized numbers are results of numerical simulations by MPA or BPM.

lasers.

Considering the records of MMI devices so far, both as single couplers capable of enhancing the performance of larger photonic circuits or as new components allowing new functionalities, we foresee an increasing exploitation of the self-imaging principle in integrated optics.

References

[1] T. H. Maiman, "Stimulated optical radiation in ruby," *Nature*, vol. 187, pp. 493–494, 1960.

[2] K. C. Kao and G. H. Hockham, "Dielectric fiber surface waveguides for optical frequencies," *Proceedings IEE*, vol. 113, no. 7, pp. 1151–1158, 1966.

[3] A. Werts, "Propagation de la lumière cohérente dans les fibres optiques," *L'Onde Electrique*, vol. 46, no. 474, pp. 967–980, 1966.

[4] J. Strong, *Concepts of Classic Optics*. San Francisco: Freeman, 1958. Appendix N.

[5] F. P. Kapron, D. B. Keck, and R. D. Maurer, "Radiation losses in glass optical waveguides," *Applied Physics Letters*, vol. 17, pp. 423–425, 1970.

[6] T. Okoshi, *Optical Fibers*. New York: Academic, 1982.

[7] M. Garbuny, *Optical Physics*, ch. 5. New York: Academic, 1965.

[8] D. B. Keck, K. D. Maurer, and P. C. Schultz, "On the ultimate lower limit of attenuation in glass optical waveguides," *Applied Physics Letters*, vol. 22, no. 7, pp. 307–309, 1973.

[9] J. R. Stauffer, "FT3C—a lightwave system for metropolitan and intercity applications," *Journal Selected Areas Communication*, vol. SAC-1, pp. 413–419, 1983.

[10] N. Imoto, A. Kawana, S. Machida, and H. Tsuchiya, "Characteristics of dispersion free single mode fiber in the 1.5-μm wavelength region," *Journal Quantum Electronics*, vol. 16, pp. 1052–1058, 1980.

[11] S. M. Abbot, R. E. Wagner, and P. R. Trischitta, "SL undersea lightwave system experiments," in *Rec. IEEE Int. Conf. Commun.*, (Boston, USA), June 1983. Paper C3.5.

[12] E. Iwahashi and H. Fukutomi, "F-400M system overview," *Rev. Electron. Commun. Lab.*, vol. 31, pp. 237–243, 1983.

[13] T. D. Croft, J. E. Ritter, and V. A. Bhagavatula, "Low-loss dispersion-shifted single-mode fiber manufactured by the OVD process," in *Proc. Conf. Optical Fiber Communication (OFC)*, (San Diego, USA), 1985. Paper WD2.

[14] L. C. Blank, L. Bickers, and S. D. Walker, "220 km and 233 km transmission experiments over low-loss dispersion-shifted fibre at 140 Mb/s and 34 Mb/s," in *Proc. Conf. Optical Fiber Communication (OFC)*, (San Diego, USA), February 1985. Paper PD-7.

[15] V. J. Mazurcyk, N. S. Bergano, R. E. Wagner, K. L. Walker, N. A. Olsson, L. G. Cohen, and J. C. Campbell, "420 Mb/s transmission through 203 km using silica-core fiber and DFB laser," in *Proc. European Conf. Optical Commun. (ECOC)*, (Stuttgart, Germany), September 1984. Paper PD-7.

[16] F. E. Goodwin, "A 3.39-μm infrared optical heterodyne communication system," *Journal Quantum Electronics*, vol. 3, no. 11, pp. 524–531, 1967.

[17] O. E. DeLange, "Wide-band optical communication systems: part II – frequency division multiplexing," *Proc. IEEE*, vol. 58, no. 10, pp. 1683–1690, 1970.

[18] K. Nosu, H. Toba, and K. Iwashita, "Optical FDM transmission technique," *Journal Lightwave Technology*, vol. 5, no. 9, pp. 1301–1308, 1987.

[19] B. S. Glance, J. Stone, K. J. Pollock, P. J. Fitzgerald, C. A. Burrus, B. L. Kasper, and L. W. Stulz, "Densely spaced FDM coherent star network with optical signals confined to equally spaced frequencies," *Journal Lightwave Technology*, vol. 6, no. 11, pp. 1770–1781, 1988.

[20] S. Yamazaki, M. Shibutani, N. Shimosaka, S. Murata, T. Ono, M. Kitamura, K. Emura, and M. Shikada, "A coherent optical FDM CATV distribution system," *Journal Lightwave Technology*, vol. 8, no. 3, pp. 396–405, 1990.

[21] C. D. Chen, J. M. P. Delevaux, B. W. Hakki, O. Mizuhara, T. V. Nguyen, R. J. Nuyts, K. Ogawa, Y. K. Park, C. S. Scolnick, R. E. Tench, J. Thomas, L. D. Tzeng, and P. D. Yeates, "A field demonstration of 10 Gb/s - 360 km transmission through embedded standard (non-DSF) fiber cables," in *Proc. Conf. Optical Fiber Communication (OFC)*, (San José, USA), pp. 124–127, February 1994. Post-deadline paper PD27.

[22] D. R. Zimmerman, T. S. Afferton, J. J. Thomas, and C. J. Scolnick, "Domestic deployment of an optically amplified 1.7 Gbit/s terrestrial lightwave system," in *Proc. Conf. Optical Fiber Communication (OFC)*, (San José, USA), pp. 258–260, February 1994. Paper ThR5.

[23] I. Garret and G. Jacobsen, "The effect of laser linewidth on coherent optical receivers with nonsynchronous demodulation," *Journal Lightwave Technology*, vol. 5, no. 4, pp. 551–560, 1987.

[24] I. Garret, D. J. Bond, J. B. Waite, D. S. L. Lettis, and G. Jacobsen, "Impact of phase noise in weakly coherent systems: A new and accurate approach," *Journal Lightwave Technology*, vol. 8, no. 3, pp. 329–337, 1990.

[25] T. Okoshi, "Polarization-state control scheme for heterodyne or homodyne optical fibre communications," *Journal Lightwave Technology*, vol. 3, no. 6, pp. 1232–1237, 1985.

[26] D. Zaccarin, D. Angers, and T. H. Huynh, "Performance analysis of optical heterodyne PSK receivers in the presence of phase-noise and adjacent channel interference," *Journal Lightwave Technology*, vol. 8, no. 3, pp. 353–366, 1990.

[27] S. Betti, G. de Marchis, E. Iannone, and M. Todaro, "Crosstalk in a DPSK FDM system affected by laser phase-noise," *Microwave and Optical Technology Letters*, vol. 3, no. 5, pp. 141–144, 1990.

[28] T. Okoshi and Y. H. Cheng, "Four-port homodyne receiver for optical fibre communications comprising phase and polarisation diversities," *Electronics Letters*, vol. 23, no. 8, pp. 377–378, 1987.

[29] T. E. Darcie, "Subcarrier multiplexing for multiple-access lightwave networks," *Journal Lightwave Technology*, vol. 5, pp. 1103–1110, 1987.

[30] R. Olshansky, V. A. Lanzisera, and P. M. Hill, "Subcarrier multiplexed lightwave systems for broadband distribution," *Journal Lightwave Technology*, vol. 7, pp. 1329–1342, 1989.

[31] G. E. Bodeep and T. E. Darcie, "Semiconductor lasers versus external modulators: A comparison of nonlinear distortion for lightwave subcarrier CATV applications," *Photonics Technology Letters*, vol. 1, pp. 401–403, 1989.

[32] S. Watanabe, T. Terahara, I. Yokota, T. Naito, T. Chikama, and H. Kuwahara, "Optical coherent broad-band transmission for long-haul and distribution systems using subcarrier multiplexing," *Journal Lightwave Technology*, vol. 11, no. 1, pp. 116–127, 1993.

[33] H. M. Rein, J. Hauenschild, M. Möller, W. McFarland, D. Pettengill, and J. Doernberg, "30 Gbit/s multiplexer and demultiplexer ICs in silicon bipolar technology," *Electronics Letters*, vol. 28, no. 1, pp. 97–99, 1992.

[34] T. Suzaki, M. Soda, H. Tezuka, T. Morikawa, C. Ogawa, H. Takemura, T. Tashiro, S. Fujita, and K. Emura, "Ten-Gbit/s optical receiver with Si bipolar IC," in *Proc. European Conf. Optical Commun. (ECOC)*, (Berlin, Germany), pp. 597–600, September 1992.

[35] N. A. Olsson, R. A. Logan, L. F. Johnson, K. L. Walker, and L. G. Cohen, "Transmission with 1.37-Tbit.km/sec capacity using ten wavelength division multiplexed lasers at 1.5 μm," in *Proc. Conf. Optical Fiber Communication (OFC)*, p. 88, 1985. Paper WB6.

[36] C. Lin, H. Kobrinski, A. Frenkel, and C. A. Brackett, "Wavelength-tunable 16 optical channel transmission experiment at 2 Gbit/s and 600 Mbit/s for broadband suscriber distribution," *Electronics Letters*, vol. 24, no. 19, pp. 1215–1216, 1988.

[37] H. Toba, K. Oda, K. Nakanishi, N. Shibata, K. Nosu, N. Takato, and M. Fukuda, "100-Channel optical FDM transmission/distribution at 622 Mb/s over 50 km," in *Proc. Conf. Optical Fiber Communication (OFC)*, 1990. Paper PD1-1.

[38] R. J. Mears, L. Reekie, L. Jauncey, and D. N. Payne, "High-gain, rare-earth-doped fibre amplifier at 1.54 μm," in *Proc. Conf. Optical Fiber Communication (OFC)*, (Reno, USA), 1987. Paper WI2.

[39] D. Lee, D. J. DiGiovanni, J. R. Simpson, A. M. Vengsarkar, and K. L. Walker, "Backward amplified spontaneous emission from erbium-doped fibers as a measure of amplifier efficiency," in *Proc. Conf. Optical Fiber Communication (OFC)*, (San José, USA), pp. 179–180, 1993. Paper ThF2.

[40] J. P. Gordon and L. F. Mollenauer, "Effects of fiber nonlinearities and amplifier spacing on ultra-long distance transmission," *Journal Lightwave Technology*, vol. 9, no. 2, pp. 170–173, 1991.

[41] P. P. Smyth, R. Wyatt, A. Fidler, P. Eardley, A. Sayles, K. Blyth, and S. Craig-Ryan, "152 photons per bit detection at 2.5 Gbit/s using an erbium fibre preamplifier," in *Proc. European Conf. Optical Commun. (ECOC)*, (Amsterdam, the Netherlands), pp. 91–94, 1990.

[42] P. K. Runge, "Impact of fiber optics on undersea communication," in *Proc. Conf. Optical Fiber Communication (OFC)*, (San José, USA), 1992. Invited paper ThH2.

[43] G. Balland, R. M. Paski, and R. A. Baker, "TAT-12/13 integration development tests – interim results," in *Proc. International Conf. Optical Fiber Submarine Telecom.*, (Versailles, France), March 1993. Paper 3.6.

[44] L. A. Wang, Y. H. Lo, M. Z. Iqbal, A. S. Gozdz, P. S. D. Lin, R. Bhat, and H. Shirokmann, "Tunable four-wavelength DFB laser array with 10-Gbit/s speed and 5-nm continuous tuning range," in *Proc. Conf. Optical Fiber Communication (OFC)*, (San José, USA), pp. 277–278, 1992. Paper FB7.

[45] T. P. Lee and C. E. Zah, "Multi-wavelength strained layer quantum well laser arrays for WDM systems and optical network applications," in *Proc. European Conf. Optical Commun. (ECOC)*, (Berlin, Germany), September 1992. Invited paper Tu B4.1.

[46] A. Hasegawa and F. Tappert, "Transmission of stationary nonlinear optical pulses in dispersive dielectric fibers. I. Anomalous dispersion," *Applied Physics Letters*, vol. 23, pp. 142–144, 1973.

[47] M. Nakazawa, K. Suzuki, E. Yamada, H. Kubota, M. Takaya, and Y.Kimura, "20 Gbit/s-1850 km and 40 Gbit/s-750 km soliton data transmissions using erbium-doped fiber amplifiers," in *Proc. Conf. Optical Fiber Communication (OFC)*, (San José, USA), pp. 41–44, Fabruary 1993. Post-deadline paper PD9-1.

[48] L. F. Mollenauer, E. Lichtman, M. J. Neubelt, and G. T. Harvey, "Demonstration using sliding-frequency guiding filters, of error-free soliton transmission over more than 20 Mm at 10 Gbit/s single channel, and over more than 13 Mm at 20 Gbit/s in a two-channel WDM," *Electronics Letters*, vol. 29, no. 10, pp. 910–911, 1993.

[49] M. Nakazawa, K. Suzuki, E. Yamada, H. Kubota, Y. Kimura, and M. Takaya, "Experimental demonstration of soliton data transmission over unlimited distances with soliton control in time and frequency domains," *Electronics Letters*, vol. 29, no. 9, pp. 729–730, 1993.

[50] B. Christensen, G. Jacobsen, E. Bødtker, J. Mark, and I. Mito, "Soliton communication on standard non dispersion-shifted fiber," in *Proc. European Conf. Optical Commun. (ECOC)*, (Montreux, Switzerland), pp. 27–33, September 1993. Invited paper MoC2.1.

[51] B. Christensen, G. Jacobsen, E. Bødtker, J. Mark, and I. Mito, "4-Gb/s soliton communication on standard non dispersion-shifted fiber," *Photonics Technology Letters*, vol. 6, no. 1, pp. 101–103, 1994.

[52] B. Wedding and B. Franz, "Unregenerated optical transmission at 10 Gbit/s via 204 km of standard singlemode fibre using a directly modulated laser diode," *Electronics Letters*, vol. 29, no. 4, pp. 402–404, 1993.

[53] P. D. Drummond, R. M. Shelby, S. Friberg, and Y. Yamamoto, "Quantum solitons in optical fibres," *Nature*, vol. 365, pp. 307–313, December 1993.

[54] S. Friberg, "Demonstration of colliding-soliton all-optical switching," *Applied Physics Letters*, vol. 63, no. 4, pp. 429–431, 1993.

[55] H. Kogelnik, "Current trends in integrated optics," in *Proc. European Conf. Optical Commun. (ECOC)*, (Copenhagen, Denmark), September 8–11 1981. Invited paper 9.1.

[56] R. H. Walden, W. E. Stanchina, R. A. Metzger, R. Y. Loo, J. Schaffner, M. W. Pierce, Y. K. Brown, F. Williams, V. Jones, J. Pikulski, M. Rodwell, K. Giboney, and R. A. Mullen, "Broadband optoelectronic integrated receiver front-ends comprising InP-based heterojunction bipolar transistors and base-collector photodiodes," in *Proc. Conf. Optical Fiber Communication (OFC)*, (San José, USA), p. 33, February 1994. Paper TuH4.

[57] L. B. Soldano, F. B. Veerman, M. K. Smit, B. H. Verbeek, and E. C. M. Pennings, "Multimode interference couplers," in *Proc. Integrated Photonics Research Topical Meeting (IPRC)*, (Monterey, USA), p. 13, April 1991. Poster TuD1.

[58] E. C. M. Pennings, R. J. Deri, A. Scherer, R. Bhat, T. R. Hayes, N. C. Andreadakis, M. K. Smit, and R. J. Hawkins, "Ultra-compact, low-loss directional coupler structures on InP for monolithic integration," in *Proc. Integrated Photonics Research Topical Meeting (IPRC)*, (Monterey, USA), April 1991. Post-deadline paper PD2.

[59] L. B. Soldano, F. B. Veerman, M. K. Smit, B. H. Verbeek, A. H. Dubost, and E. C. M. Pennings, "Planar monomode optical couplers based on multi-mode interference," *Journal Lightwave Technology*, vol. 10, no. 12, pp. 1843–1850, 1992.

[60] L. B. Soldano, M. Bouda, M. K. Smit, and B. H. Verbeek, "New small-size single-mode optical power splitter based on multi-mode interference," in *Proc. European Conf. Optical Commun. (ECOC)*, (Berlin, Germany), pp. 465–468, September 1992. Paper We B10.5.

[61] L. B. Soldano and E. C. M. Pennings, "Optical multi-mode interference devices based on self-imaging: Principles and applications," *Journal Lightwave Technology*, 1994. Invited paper, accepted for publication.

[62] L. B. Soldano, M. K. Smit, A. H. de Vreede, J. W. M. van Uffelen, B. H. Verbeek, P. van Bennekom, W. H. C. de Krom, and W. van Etten, "New all-passive 4×4 planar optical phase diversity network," in *Proc. European Conf. Optical Commun. (ECOC)*, (Paris, France), pp. 96–99, September 1991.

[63] W. H. C. de Krom, *Optical coherent phase diversity systems.* PhD thesis, Eindhoven University of Technology, Eindhoven, the Netherlands, 1992. ISBN 90-90048997-9.

[64] L. B. Soldano, A. H. de Vreede, M. K. Smit, B. H. Verbeek, E. G. Metaal, and F. H. Groen, "Mach-Zehnder interferometer polarization splitter in InGaAsP/InP," *Photonics Technology Letters*, vol. 6, no. 3, pp. 402–405, 1994.

[65] E. C. M. Pennings, *Bends in optical ridge waveguides, modeling and applications.* PhD thesis, Delft University of Technology, Delft, the Netherlands, 1990. ISBN 90-9003413-7.

[66] M. K. Smit, *Integrated optics in silicon-based aluminum oxide.* PhD thesis, Delft University of Technology, Delft, the Netherlands, 1991. ISBN 90-9004261-X.

[67] M. R. Amersfoort, *Phased-array wavelength demultiplexers and their integration with photodetectors.* PhD thesis, Delft University of Technology, Delft, the Netherlands, 1994. ISBN 90-407-1041-4.

[68] H. F. Talbot, "Facts relating to optical science No. IV," *The London and Edinburgh Philosophical Magazine and Journal of Science*, vol. 9, pp. 401–407, December 1836. Third Series.

[69] D. Marcuse, *Light Transmission Optics.* New York: Van Nostrand Reinhold, 1972.

[70] O. Bryngdahl, "Image formation using self-imaging techniques," *J. Opt. Soc. Am.*, vol. 63, no. 4, pp. 416–419, 1973.

[71] R. Ulrich, "Image formation by phase coincidences in optical waveguides," *Optics Communications*, vol. 13, no. 3, pp. 259–264, 1975.

[72] R. Ulrich, "Light-propagation and imaging in planar optical waveguides," *Nouv. Rev. Optique*, vol. 6, no. 5, pp. 253–262, 1975.

[73] R. Ulrich and G. Ankele, "Self-imaging in homogeneous planar optical waveguides," *Appl. Phys. Lett.*, vol. 27, no. 6, pp. 337–339, 1975.

[74] D. C. Chang and E. F. Kuester, "A hybrid method for paraxial beam propagation in multimode optical waveguides," *Trans. Microwave Theory Techniques*, vol. MTT-29, no. 9, pp. 923–933, 1981.

[75] A. Simon and R. Ulrich, "Fiber-optical interferometer," *Appl. Phys. Lett.*, vol. 31, no. 2, pp. 77–79, 1977.

[76] C. M. Weinert and N. Agrawal, "Three-dimensional simulation of multimode interference devices," in *Proc. Integrated Photonics Research Topical Meeting (IPRC)*, (San Francisco, USA), February 1994. Paper FH2.

[77] R. M. Knox and P. P. Toulios, "Integrated circuits for the millimeter through optical frequency range," in *Proc. MRI Symp. on Submillimiter Waves* (J. Fox, ed.), (New York, USA), pp. 497–516, Polytechnic Press, 1970.

[78] P. N. Robson and P. C. Kendall, eds., *Rib waveguide theory by the spectral index method.* Optoelectronic Series, John Wiley & Sons Inc., 1990. ISBN 0-86380-110-2.

[79] N. S. Kapany and J. J. Burke, *Optical Waveguides.* New York: Academic Press, 1972.

[80] E. C. M. Pennings, R. J. Deri, R. Bhat, T. R. Hayes, N. C. Andreadakis, M. K. Smit, L. B. Soldano, and R. J. Hawkins, "Ultracompact, low-loss directional couplers on InP based on self-imaging by multimode interference," *Appl. Phys. Lett.*, vol. 59, no. 16, pp. 1926–1928, 1991.

[81] F. B. Veerman, P. J. Schalkwijk, E. C. M. Pennings, M. K. Smit, and B. H. Verbeek, "An optical passive 3-dB TMI coupler with reduced fabrication tolerance sensitivity," *J. Lightwave Technol.*, vol. 10, no. 3, pp. 306–311, 1992.

[82] J. E. Zucker, K. L. Jones, T. H. Chiu, B. Tell, and K. Brown-Goebeler, "Polarization-independent electro-optic waveguide switch using strained InGaAs/InP quantum wells," in *Proc. Integrated Photonics Research Topical Meeting (IPRC)*, (New Orleans, USA), pp. 21–24, April 1992. Paper Pd7.

[83] J. E. Zucker, K. L. Jones, T. H. Chiu, and K. Brown-Goebeler, "Strained quantum wells for polarization-independent electroopic waveguide switches," *Journal Lightwave Technology*, vol. 10, no. 12, pp. 1926–1930, 1992.

[84] M. Bachmann, P. A. Besse, and H. Melchior, "General self-imaging properties in N×N multi-mode interference couplers including phase relations," *Applied Optics*, 1994. Accepted for publication.

[85] T. Niemeier and R. Ulrich, "Quadrature outputs from fiber interferometer with 4×4 coupler," *Optics Letters*, vol. 11, no. 10, pp. 677–679, 1986.

[86] P. Roth, "Passive integrated optic mixer providing quadrature outputs," in *Proc. 5th European Conf. on Integrated Optics*, (Paris, France), pp. 169–173, 1989.

[87] E. C. M. Pennings, R. J. Deri, R. Bhat, T. R. Hayes, and N. C. Andreadakis, "Ultra-compact integrated all-passive optical 90° hybrid using self-imaging," in *Proc. 18th European Conf. Optical Communication ECOC'92*, (Berlin, Germany), pp. 461–464, October 1992. Paper We B10.4.

[88] R. M. Jenkins, J. M. Heaton, D. R. Wight, J. T. Parker, J. C. H. Birbeck, G. W. Smith, and K. P. Hilton, "Novel 1×N and N×N integrated optical switches using self-imaging multimode GaAs/AlGaAs waveguides," *Applied Physics Letters*, vol. 64, no. 6, pp. 684–686, 1994.

[89] L. B. Soldano, F. B. Veerman, M. K. Smit, B. H. Verbeek, A. H. Dubost, and E. C. M. Pennings, "High-performance monomode planar couplers using a short multi-mode interference section," in *Proc. European Conf. Optical Commun. (ECOC)*, (Paris, France), pp. 225–228, September 1991. Paper TuB5-2.

[90] R. M. Jenkins, R. W. J. Deveraux, and J. M. Heaton, "Waveguide beam splitters and recombiners based on multimode propagation phenomena," *Optics Letters*, vol. 17, no. 14, pp. 991–993, 1992.

[91] J. M. Heaton, R. M. Jenkins, D. R. Wight, J. T. Parker, J. C. H. Birbeck, and K. P. Hilton, "Novel 1-to-N way integrated optical beam splitters using symmetric mode mixing in GaAs/AlGaAs multimode waveguides," *Appl. Phys. Lett.*, vol. 61, no. 15, pp. 1754–1756, 1992.

[92] P. A. Besse, M. Bachmann, and H. Melchior, "Phase relations in multi-mode interference couplers and their applications to generalized integrated Mach-Zehnder optical switches," in *Proc. European Conf. Integrated Optics (ECIO)*, (Neuchâtel, Switzerland), pp. 2.22–2.23, April 1993.

[93] A. Ferreras, F. Rodríguez, E. Gómez-Salas, J. L. de Miguel, and F. Hernández-Gil, "Design and fabrication of a InP/InGaAsP multimode power splitter," in *Proc. Integrated Photonics Research Topical Meeting (IPRC)*, (Palm Springs, USA), pp. 151–154, March 22–24 1993. Paper IME4.

[94] A. Ferreras, F. Rodríguez, E. Gómez-Salas, J. L. de Miguel, and F. Hernández-Gil, "Useful formulas for multimode interference power splitter/combiner design," *Photonics Technology Letters*, vol. 5, no. 10, pp. 1224–1227, 1993.

[95] T. P. Young, S. N. Radcliffe, A. J. Davies, and P. Smith, "Beamer — a design tool for integrated optics," *GEC Journal of Research*, vol. 6, no. 3, pp. 152–161, 1988.

[96] C. Rolland, D. M. Adams, D. Yevick, and B. Hermansson, "Optimization of strongly guiding semiconductor rib waveguide Y-junctions," *Photonics Technology Letters*, vol. 2, no. 6, pp. 404–406, 1990.

[97] R. Ulrich and T. Kamiya, "Resolution of self-images in planar optical waveguides," *J. Opt. Soc. Am.*, vol. 68, no. 5, pp. 583–592, 1978.

[98] P. A. Besse, M. Bachmann, H. Melchior, L. B. Soldano, and M. K. Smit, "Optical bandwidth and fabrication tolerances of multimode interference couplers," *Journal Lightwave Technology*, vol. 12, no. 6, pp. 1004–1009, 1994.

[99] L. B. Soldano, M. Bachmann, P. A. Besse, M. K. Smit, and H. Melchior, "Large optical bandwidth of InGaAsP/InP multi-mode interference 3-dB couplers," in *Proc. European Conf. Integrated Optics (ECIO)*, (Neuchâtel, Switzerland), pp. 14.10–14.11, April 1993.

[100] F. Fiedler and A. Schlachetzki, "Optical parameters of InP-based waveguides," *Solid-State Electronics*, vol. 30, no. 1, pp. 73–83, 1987.

[101] B. Chapman, *Glow discharge process, sputtering and plasma etching*. New York: Wiley, 1980.

[102] M. K. Smit, C. J. van der Laan, and G. A. Acket, "Aluminum oxide films for integrated optics," *Thin Solid Films*, vol. 138, pp. 171–181, 1986.

[103] W. A. Pasmooij, P. A. Mandersloot, and M. K. Smit, "Prism-coupling of light into narrow planar optical waveguides," *Journal Lightwave Technology*, vol. 7, no. 1, pp. 175–180, 1989.

[104] V. Ramaswamy, "Strip-loaded film waveguide," *The Bell System Technical Journal*, vol. 53, no. 4, pp. 697–704, 1973.

[105] I. Moerman, G. Coudenys, P. Demeester, B. Turner, and J. Cawley, "Influence of gas mixing on the lateral uniformity in horizontal MOVPE reactors," *J. Cryst. Growth*, vol. 107, pp. 175–180, 1991.

[106] R. J. Deri and E. Kapon, "Low-loss III-V semiconductor optical waveguides," *Journal Quantum Electronics*, vol. 27, no. 3, pp. 626–640, 1991.

[107] J. D. Cuthbert, "Optical projection printing," *Solid State Technology*, pp. 59–69, August 1977.

[108] W. G. Oldham, W. Arden, H. Binder, and C. Ting, "Contrast studies in high-performance projection optics," *Trans. Electron Devices*, vol. 30, no. 11, pp. 1474–1479, 1983.

[109] M. Spak, D. Mammato, S. Jain, and D. Durham, "Mechanism and lithographic evaluation of image reversal in AZ-5214 photoresist," tech. rep., American Hoechst Corp., Somerville, USA, 1985.

[110] M. Bolsen, "AZ-5200 resists for positive and negative patterning," tech. rep., Hoechst Japan Ltd., Minato-ku, Japan, 1986.

[111] L. H. Spiekman, F. P. van Ham, M. Kroonwijk, Y. S. Oei, J. J. G. M. van der Tol, F. H. Groen, and G. Coudenys, "A new fabrication process for very low-loss narrow-width InGaAsP/InP waveguides," in *Proc. European Conf. Integrated Optics (ECIO)*, (Neuchâtel, Switzerland), April 1993. Paper 2-30.

[112] Y. S. Oei, C. van Dam, F. P. van Ham, L. H. Spiekman, B. H. Verbeek, F. H. Groen, E. G. Metaal, and J. W. Pedersen, "Improved RIE-technique for controlled roughness and anisotropy in InP-based devices," in *Proc. State of the Art Program on Compound Semiconductors (SOTAPOCS XVIII)*, (Pennington, USA), pp. 134–141, The Electrochemical Society, Inc., 1993. Proceedings Volume 93-27.

[113] R. J. Deri, "Monolithic integration of optical waveguide circuitry with III-V photodetectors for advanced lightwave receivers," *Journal Lightwave Technology*, vol. 11, no. 8, pp. 1296–1313, 1993.

[114] A. Bandyopadhyay and P. K. Basu, "A comparative study of phase modulation in InGaAsP/InP and GaAs/AlGaAs based P-p-n-N structures," *Journal Lightwave Technology*, vol. 10, no. 10, pp. 1438–1442, 1992.

[115] T. Tamir, ed., *Integrated Optics*, vol. 7 of *Topics in Applied Physics*. Springer-Verlag, 2nd ed., 1979.

[116] M. Dagenais, R. F. Leheny, H. Temkin, and P. Bhattacharya, "Applications and challenges of OEIC technology: A report on the 1989 Hilton Head workhsop," *Journal Lightwave Technology*, vol. 8, no. 6, pp. 846–862, 1990.

[117] T. P. Pearsall, ed., *GaInAsP Alloy Semiconductor*. John Wiley & Sons, 1982.

[118] W. K. Marshall and J. Katz, "Waveguide p-i-n junction electrooptic modulators: Theoretical analysis and design criteria," *Applied Optics*, vol. 24, pp. 1996–2000, 1985.

[119] B. R. Bennett, R. A. Soref, and J. del Alamo, "Carrier-induced change in refractive index of InP, GaAs, and InGaAsP," *Journal Quantum Electronics*, vol. 26, no. 1, pp. 113–122, 1990.

[120] J. F. Vinchant, J. A. Cavaillès, M. Erman, P. Jerry, and M. Renaud, "InP/GaInAsP guided-wave phase modulators based on carrier-induced effects: Theory and experiment," *Journal Lightwave Technology*, vol. 10, no. 1, pp. 63–70, 1992.

[121] J. G. Mendoza-Alvarez, L. A. Coldren, A. Alping, R. H. Yan, T. Hausken, K. Lee, and K. Pedrotti, "Analysis of depletion edge translation lightwave modulators," *Journal Lightwave Technology*, vol. 6, no. 6, pp. 793–808, 1988.

[122] J. Buus, "The effective index method and its application to semiconductor lasers," *Journal Quantum Electronics*, vol. 18, no. 7, pp. 1083–1089, 1982.

[123] K. S. Chiang, "Performance of the effective-index method for the analysis of dielectric waveguides," *Optics Letters*, vol. 16, no. 10, pp. 714–716, 1991.

[124] K. Utaka, K. I. Kobayashi, and Y. Suematsu, "Lasing characteristics of 1.5–1.6 μm GaInAsP/InP integrated twin-guide lasers with first order distributed Bragg reflectors," *Journal Quantum Electronics*, vol. 17, no. 5, pp. 651–658, 1981.

[125] M. Papuchon, A. Roy, and D. B. Ostrowsky, "Electrically active optical bifurcation: BOA," *Applied Physics Letters*, vol. 31, no. 4, pp. 266–267, 1977.

[126] F. Rottmann, A. Neyer, W. Mevenkamp, and E. Voges, "Integrated-optic wavelength multiplexers on lithium niobate based on two-mode interference," *Journal Lightwave Technology*, vol. 6, pp. 946–952, 1988.

[127] C. Caldera, C. D. Bernardi, G. Destefanis, M. Meliga, S. Morasca, C. Rigo, and A. Stano, "3-dB couplers integrated in InGaAlAs/InP for coherent applications," in *Proc. European Conf. Optical Commun. (ECOC)*, (Amsterdam), pp. 357–360, September 1990.

[128] S. Gevorgyan and A. Hovsepyan, "Coupling among waveguides of small spacing," *Electronics Letters*, vol. 24, no. 1, pp. 814–815, 1988.

[129] R. J. Deri, E. C. M. Pennings, A. Scherer, A. S. Gozdz, C. Caneau, N. C. Andreadakis, V. Shah, L. Curtis, R. J. Hawkins, J. B. D. Soole, and J. I. Song, "Ultracompact monolithic integration of balanced, polarization diversity photodetectors for coherent lightwave receivers," *Photonics Technology Letters*, vol. 4, no. 11, pp. 1238–1240, 1992.

[130] M. Bachmann, M. K. Smit, L. B. Soldano, P. A. Besse, E. Gini, and H. Melchior, "Polarization-insensitive low-voltage optical waveguide switch using InGaAsP/InP four-port Mach-Zehnder inteferometer," in *Proc. Conf. on Optical Fiber Communication OFC/IOOC'93*, (San José, USA), pp. 32–33, 1993. Paper TuH3.

[131] R. J. Deri, R. Welter, E. C. M. Pennings, C. Caneau, J. L. Jackel, R. J. Hawkins, J. J. Johnson, H. Gilchrist, and C. Gibbons, "High-speed heterodyne operation of monolithically integrated balanced polarisation diversity photodetectors," *Electronics Letters*, vol. 28, no. 25, pp. 2332–2334, 1992.

[132] J. E. Watson and A. Milbrodt, "Calculated wavelength sensitivity of lithium niobate switches," *Journal Lightwave Technology*, vol. 7, no. 12, pp. 1973–1981, 1989.

[133] I. Januar, R. J. Feuerstein, A. R. Mickelson, and J. R. Sauer, "Wavelength sensitivity in directional couplers," *Journal Lightwave Technology*, vol. 10, no. 9, pp. 1202–1209, 1992.

[134] Y. C. Chung and N. Dagli, "An assessment of finite difference beam propagation method," *Journal Quantum Electronics*, vol. 26, no. 8, pp. 1335–1339, 1990.

[135] E. C. M. Pennings, R. J. Deri, A. Scherer, R. Bhat, T. R. Hayes, N. C. Andreadakis, M. K. Smit, and R. J. Hawkins, "Ultra-compact, low-loss directional coupler structures on InP for monolithic integration," in *Proc. European Conf. Optical Commun. (ECOC)*, (Paris, France), pp. 405–408, September 1991. Paper WeA7-3.

[136] G. L. Abbas, V. W. S. Chan, and T. K. Yee, "A dual-detector optical heterodyne receiver for local oscillator noise suppression," *Journal Lightwave Technology*, vol. 3, no. 5, pp. 1110–1122, 1985.

[137] S. B. Alexander, "Design of wide-band optical heterodyne balanced mixer receivers," *Journal Lightwave Technology*, vol. 5, no. 4, pp. 523–537, 1987.

[138] L. G. Kazovsky, "Optical heterodyning versus optical homodyning: A comparison," *Journal Optical Communications*, vol. 6, no. 1, pp. 18–24, 1985.

[139] T. G. Hodgkinson, "Phased locked loop analysis for pilot carrier coherent optical receivers," *Electronics Letters*, vol. 21, pp. 1202–1203, 1985.

[140] L. G. Kazovsky, "Decision driven phased locked loop for optical homodyne receivers: Performance analysis and laser linewidth requirements," *Journal Lightwave Technology*, vol. 3, no. 6, pp. 1238–1247, 1985.

[141] L. G. Kazovsky, "Balanced phased locked loops for optical homodyne receivers: Performance analysis design considerations, and laser linewidth requirements," *Journal Lightwave Technology*, vol. 4, no. 2, pp. 182–195, 1986.

[142] A. W. Davis, M. J. Pettit, J. P. King, and S. Wright, "Phase diversity techniques for coherent optical components," *Journal Lightwave Technology*, vol. 5, no. 4, pp. 561–572, 1987.

[143] J. Siuzdak and W. van Etten, "BER evaluation for phase and polarization diversity optical homodyne receivers using noncoherent ASK and DPSK demodulation," *Journal Lightwave Technology*, vol. 7, no. 4, pp. 584–599, 1989.

[144] L. McCaughan and N. Agrawal, "Novel physical effects in intersecting waveguides," *Applied Physics Letters*, vol. 51, no. 18, pp. 1389–1391, 1987.

[145] N. Agrawal and L. McCaughan, "Low-loss Ti:$LiNbO_3$ intersecting waveguides," *Applied Physics Letters*, vol. 54, no. 17, pp. 1669–1671, 1989.

[146] F. McKenzie, C. J. Beaumont, M. Nield, and S. A. Cassidy, "Measurement of excess loss in planar silica X-junctions," *Electronics Letters*, vol. 28, no. 20, pp. 1919–1920, 1992.

[147] R. R. Hayes and D. Yap, "GaAs spiral optical waveguides for delay-line applications," *Journal Lightwave Technology*, vol. 11, no. 3, pp. 523–528, 1993.

[148] N. Agrawal, L. McCaughan, and R. Shesadri, "A multiple scattering interaction analysis of intersecting waveguides," *Journal Applied Physics*, vol. 62, no. 6, pp. 2187–2193, 1987.

[149] M. Heiblum and J. H. Harris, "Analysis of curved optical waveguides by conformal transformation," *Journal Quantum Electronics*, vol. 11, no. 2, pp. 75–83, 1975. See also erratum in *op. cit.*, vol. 12 (1976), p. 313.

[150] W. H. C. de Krom, "Sensitivity degradation of an optical 2×2 and a 3×3 phase diversity ASK receiver due to gain imbalance and nonideal phase relations of the optical hybrid," *Journal Lightwave Technology*, vol. 9, no. 11, pp. 1593–1601, 1991.

[151] P. Roth and O. Parriaux, "Integrated optic interferometer with phase diversity," in *Proc. Conf. on Integrated Optics and Optical Communications*, (Kobe, Japan), pp. 120–121, 1989.

[152] L. G. Kazovsky, "Phase- and polarization-diversity coherent optical techniques," *Journal Lightwave Technology*, vol. 7, pp. 279–292, 1989.

[153] S. Betti, F. Curtis, and G. D. Marchis E. Iannone, "Phase noise and polarization state insensitive optical coherent systems," *Journal Lightwave Technology*, vol. 8, no. 5, pp. 756–767, 1990.

[154] Y. Hayashi, N. Ohkawa, H. Fushumi, and D. Yanai, "A fully-engineered coherent optical trunk transmission system," in *Proc. European Conf. Optical Commun. (ECOC)*, (Paris, France), pp. 393–396, September 1991. Paper WeA6-4.

[155] H. Tsushima, S. Sasaki, K. Kuboki, S. Kitajima, R. Takeyari, and M. Okai, "1.244-Gbit/s 32-channel 121-km transmission experiment using shelf-mounted CPFSK optical heterodyne system," in *Proc. European Conf. Optical Commun. (ECOC)*, (Paris, France), pp. 397–400, September 1991. Paper WeA6-5.

[156] E. Bødtker, B. Christensen, G. Jacobsen, N. G. Jensen, and H. J. Olsen, "Field test of fully implemented, highly sensitive 636 Mb/s polarization diversity SF-FSK system," in *Proc. European Conf. Optical Commun. (ECOC)*, (Paris, France), pp. 401–404, September 1991. Paper WeA6-6.

[157] K. Fukuchi, S. Yamazaki, T. Ono, and M. Rangaraj, "Polarization shift keying – direct detection scheme for fiber nonlinear effect insensitive communication system," in *Proc. European Conf. Optical Commun. (ECOC)*, (Berlin Germany), pp. 169–172, Sept-Oct 1992.

[158] F. Heismann, P. B. Hansen, S. K. Korotky, G. Raybon, J. J. Veselka, and M. S. Whalen, "Automatic polarization demultiplexer for polarization-multiplexed transmission systems," in *Proc. European Conf. Optical Commun. (ECOC)*, (Montreux, Switzerland), pp. 401–404, September 1993.

[159] M. Masuda and G. L. Yip, "An optical TE-TM mode splitter using a $LiNbO_3$ branching waveguide," *Applied Physics Letters*, vol. 37, pp. 20–22, 1980.

[160] Y. Shani, C. H. Henry, R. C. Kistler, and K. J. Orlowsky, "Four-port integrated optic polarization splitter," *Applied Optics*, vol. 29, no. 3, pp. 337–339, 1990.

[161] P. Albrecht, M. Hamacher, H. Heidrich, D. Hoffmann, H. P. Nolting, and C. M. Weinert, "TE/TM mode splitters on InGaAsP/InP," *Photonics Technology Letters*, vol. 2, no. 2, pp. 114–115, 1990.

[162] J. W. Pedersen, J. J. G. M. van der Tol, E. G. Metaal, Y. S. Oei, F. H. Groen, and I. Moerman, "Realization of a mode evolution polarization splitter on InGaAsP/InP," in *Proc. European Conf. Optical Commun. (ECOC)*, (Montreux, Switzerland), September 1993. Post-deadline paper ThC12.3.

[163] M. A. Ordal, L. L. Long, R. J. Bell, S. E. Bell, R. R. Bell, R. W. Alexander, and C. A. Ward, "Optical properties of the metals Al, Co, Cu, Au, Fe, Pb, Ni, Pd, Pt, Ag, Ti, and W in the infrared and near infrared," *Applied Optics*, vol. 22, no. 7, pp. 1099–1119, 1983.

[164] S. Rashleigh, "Four-layer metal-clad thin film optical waveguides," *Optical and Quantum Electronics*, vol. 8, pp. 49–60, 1976.

[165] J. Buus, "Analytical approximation for the reflectivity of DH lasers," *Journal Quantum Electronics*, vol. 17, no. 12, pp. 2256–2257, 1981.

[166] R. Regener and W. Sohler, "Loss in low-finesse Ti:$LiNbO_3$ optical waveguide resonators," *Applied Physics B*, vol. 36, pp. 143–147, 1985.

[167] K. Al-hemyari, G. F. Doughty, C. D. W. Wilkinson, A. H. Kean, and C. R. Stanley, "Optical loss measurements on GaAs/GaAlAs single-mode waveguide Y-junctions and waveguide bends," *Journal Lightwave Technology*, vol. 11, no. 2, pp. 272–276, 1993.

[168] R. Adar, C. H. Henry, R. F. Kazarinov, R. C. Kistler, and G. R. Weber, "Adiabatic 3-dB couplers, filters and multiplexers made with silica waveguides on silicon," *Journal Lightwave Technology*, vol. 10, no. 1, pp. 46–50, 1992.

[169] M. Zirngibl, C. Dragone, C. H. Joyner, M. Kouznetsov, and U. Koren, "Efficient 1×16 optical power splitter based on InP," *Electronics Letters*, vol. 28, no. 13, pp. 1212–1213, 1992.

[170] L. H. Spiekman, Y. S. Oei, E. G. Metaal, F. H. Groen, I. Moerman, M. K. Smit, and B. H. Verbeek, "Extremely small, fabrication-tolerant InP-based power-splitting and combining structures by deep etching," in *Proc. European Conf. Optical Commun. (ECOC)*, (Firenze, Italy), September 25–29 1994. Paper We.C.2.3.

[171] C. Dragone, C. H. Henry, I. P. Kaminow, and R. C. Kistler, "Efficient multichannel integrated optics star coupler on silicon," *Photonics Technology Letters*, vol. 1, no. 8, pp. 241–243, 1989.

[172] K. Okamoto, H. Takahashi, M. Yasu, and Y. Hibino, "Fabrication of wavelength-insensitive 8×8 star coupler," *Photonics Technology Letters*, vol. 4, no. 1, pp. 61–63, 1992.

[173] J. M. Heaton. Private communication, 1994.

[174] P. A.Besse, E. Gini, M. Bachmann, and H. Melchior, "New 1×2 multi-mode interference couplers with free selection of power splitting ratios," in *Proc. European Conf. Optical Commun. (ECOC)*, (Firenze, Italy), September 25–29 1994. Paper We.C.2.4.

Samenvatting

Dit proefschrift beschrijft de analyse, fabricage, metingen en een aantal toepassingen van geintegreerde optische componenten gebaseerd op multimodale interferentie (MMI).

De werking van MMI componenten is gebaseerd op het principe van zelfafbeelding, waarbij enkel- of meervoudige replica's van een ingangsveld op regelmatige intervallen in de richting van propagatie worden gereproduceerd. Het zelfafbeeldend principe wordt bestudeerd door middel van een propagatie analyse van geleide modi. Afhankelijk van de modale excitatie worden verschillende interferentie mechanismen gevonden, die het ontwerp van een scala van N×N en N×M optische koppelaars mogelijk maken.

Een eenvoudige uitdrukking wordt afgeleid voor de berekening van de afbeeldingsresolutie van een multimodale golfgeleider op basis van zijn numerieke apertuur. Fabricagetoleranties, optische bandbreedte en polarisatie- afhankelijkheid worden berekend. De breedte van de multimode sectie blijkt de meest kritische grootheid te zijn.

Een aantal 3-dB en kruisingskoppelaars is ontworpen, gefabriceerd en getest bij een golflengte van 1.55 μm. Onbalans waarden minder dan 0.2 dB, overspraak ter grotte van -18 dB en verlies minder dan 0.5 dB t.o.v. een rechte referentie golfgeider zijn gemeten voor koppelaars gefabriceerd in zowel Si als InP gebaseerde golfgeleiders. Voor 3-dB koppelaars in InP/InGaAsP is de invloed van fabricage- en werkingenparameters variaties experimenteel bepaald. Voor een maximum extra verlies van 1 dB en een onbalans beter dan 0.2 dB, dient de breedte van de multimode sectie minder ± 0.25 μm van de ontwerp- waarde af te wijken. Onder dezelfde voorwaarden is een optische bandbreedte van ruim 100 nm gemeten. Een polarisatie-afhankelijkheid van ongeveer 0.3 dB wordt berekend en gemeten, indien het ontwerp voor een van beide polarisaties is geoptimaliseerd. Door het ontwerp in het midden van de optima voor de twee polarisaties te kiezen, kan deze afhankelijkheid nog met een factor twee gereduceerd worden.

Een zeer korte ($\sim$25 μm voor Si gebaseerde en $\sim$60 μm voor InP gebaseerde golfgeleiders) 1×2 vermogenssplitser is gefabriceerd. Gemiddelde componentverliezen van 1 dB, tezamen met een onbalans van slechts 0.1 dB zijn gemeten voor 30 tot 40% van alle componenten.

Een geheel passief 4×4 phase-diversity netwerk is gerealiseerd bestaande uit vier MMI 3-dB koppelaars, een fase draaier en golfgeleider structuren om deze componenten onderling te verbinden. Het beste verkregen resultaat was een verlies van $\sim$3 dB voor het gehele netwerk, met een onbalans binnen 0.5 dB en fase afwijkingen van 5°/12°/12°/9°.

Een passieve polarisatiesplitser, gebaseerd op een Mach-Zehnder structuur, is gerealiseerd in InP/InGaAsP. Een diëlectrische laag en een metaallaag gepositioneerd bovenop een dijk golfgeleider zorgen voor een verschuiving van de effectieve brekingsindex voor TM polarisatie, terwijl de effectieve index voor TE polarisatie niet verandert, en de verliezen blijven acceptabel. Over een 60-nm golflengte bereik is een TE (TM) onderdrukkingscoëefficient beter dan -16 dB ($-$ 13dB), met een inzetverlies van slechts 1.5 dB, gemeten.

Aan het slot van dit proefschrift wordt een kort overzicht gegeven van de eigenschappen van MMI componenten in vergeleking met andere koppelende en routerende componenten. MMI componenten blijken zeer veelzijdig te zijn. Een aanzienlijk aantal kopppelings-, combinatie- en splitsingsfuncties is mogelijk met prestaties vergelijkbaar of beter dan conventionele componenten.

Acknowledgements

The list of those people who have helped and cooperated with me during my research work is very long. I would like to mention here a few of them.

Prof Dr B.H. Verbeek led me into the field of integrated optics and offered me the opportunity to work and write this thesis at the Laboratory of Telecommunication and Remote Sensing Technology.

Dr M.K. Smit has been a continuous inspiration and a reliable beacon in every matter concerning research. I am much indebted to him.

Dr E.C.M. Pennings taught me more than one important fact about integrated optics. I am thankful to him for writing the modal propagation analysis software and for his valuable contribution when preparing the invited paper for the *Journal of Lightwave Technology*, parts of which have been used in this thesis.

Dr Y.S. Oei, A.H. de Vreede, C.R. de Boer, F.P.G.M. van Ham and J.W.M. van Uffelen have provided all the technical support. I am grateful to them not only for their devotion to quality technology but also for their remarkable skill in understanding my specifications.

My colleagues C. van Dam, X.J.M. Leijtens, L.H. Spiekman, C.A.M. Steenbergen and C.G.M. Vreeburg have participated in discussions and provided useful advice. I am particularly grateful to M.R. Amersfoort for his constant good humour, which has enlivered many working hours spent together.

Some students have contributed with their undergraduate laboratory tasks. F. Veerman developed the first "quasi-MMI" couplers and was of much help during my initial round of measurements. A.H. Dubost designed and tested the first silica-based MMI couplers. I had a great pleasure –and luck– in coaching him during his specialization stage at the Delft University. M. Bouda carried out the experiments on the 1×2 power splitters and provided illustrative material.

A number of people outside the laboratory have also collaborated on this work. P. van Bennekom of the Eindhoven University devoted plenty of time, equipment and expertise to the measurement of the phase diverity network. G. Krijnen of the University of Twente provided the BPM software. A. Kuntze of the department of Applied Physics deposited the anti-reflection coatings. E.G. Metaal of the PTT Research Leidschendam performed the reactive ion etching on some samples. M. Bachmann and P.A. Besse of the Swiss Federal Instutute of Technology, and J.M. Heaton of the British Defence Research Agency provided with many useful suggestions and experimental data for some publications. Philips Research Laboratories polished the silica-based chips and supplied with chromium masks. Mrs J.B. Zaat-Jones skilfully corrected the manuscript, the remaining language mistakes were slipped in by me during later amendments.

I should like to acknowledge here the hospitality of the Dutch people. I would also like to thank all of my friends, here and overseas, who have been of much inspiration in my quest of

happiness beyond the boundaries of science.

Finally, it is a pleasure to have a chance to recognize the help of my family. They have always encouraged, supported and cheered me up throughout my work.

Biography

Lucas B. Soldano was born in Buenos Aires, Argentina, on June 1, 1960. He studied at Buenos Aires University, where he received his Electronics Engineer degree in 1988. During his studies he was active in the field of gas- and solid-state lasers. In 1991 he obtained a Design Engineer degree in Microelectronics, from Delft University of Technology, Delft, the Netherlands, where he is currently working toward his Ph.D. degree. His present research work deals with integrated optical components for telecommunications.